Structure - Property Evaluation of Gd & Ca Added Mg-Al & Mg-Zn Alloys

Thesis Submitted to AcSIR for the Award of the Degree of
DOCTOR OF PHILOSOPHY
in
Engineering Sciences

By

ATHUL K.R.

Registration No: 20EE13A39016

Under the guidance of

Dr. A. SRINIVASAN
&
Dr. U.T.S. PILLAI

CSIR - NATIONAL INSTITUTE FOR INTERDISCIPLINARY SCIENCE & TECHNOLOGY (CSIR - NIIST)
THIRUVANANTHAPURAM, KERALA, INDIA

2018

To You.

DECLARATION

I hereby declare that the matter embodied in the thesis entitled: "***Structure - Property Evaluation of Gd & Ca Added Mg-Al & Mg-Zn Alloys***" is the result of the investigations carried out by me at the Materials Science and Technology Division, CSIR - National Institute for Interdisciplinary Science and Technology (CSIR - NIIST), Trivandrum, under the supervision of Dr. A. Srinivasan and Dr. U.T.S. Pillai and the same has not been submitted elsewhere for any other degree.

In keeping with the general practice of reporting scientific observations, due acknowledgement has been made wherever the work described is based on the findings of other investigators.

Athul K.R.

National Institute for Interdisciplinary Science & Technology
Council of Scientific & Industrial Research
Government of India
Thiruvananthapuram - 695 019, Kerala, India

CERTIFICATE

This is to certify that the work incorporated in this Ph.D. thesis entitled "***Structure - Property evaluation of Gd & Ca added Mg-Al & Mg-Zn alloys***" submitted by **Mr. Athul K.R.** to Academy of Scientific and Innovative Research (AcSIR), in partial fulfilment of the requirements for the award of the **Degree of Doctor of Philosophy in Engineering Sciences**, embodies original research work under our combined supervision and guidance at the Materials Science and Technology Division of the CSIR - National Institute for Interdisciplinary Science and Technology (CSIR - NIIST), Trivandrum. We further certify that this work has not been submitted to any other University or Institution in part or full for the award of any degree or diploma.

Dr. U.T.S. Pillai
(Thesis Supervisor)

Dr. A. Srinivasan
(Thesis Supervisor)

Acknowledgements

"Thought is the wind, knowledge is an ocean and mankind the vessel." This thesis is the end of my long journey which has been kept on track and seen through to completion with the support and encouragement of numerous people including my well wishers, friends, colleagues and various institutions. As we all know, the sea is not forever calm and there had been rough times. It is my pleasant task to express my thanks to all those who steered this journey to success and made it an unforgettable experience for me.

It is with great respect and profound gratefulness that I record my indebtedness and deep felt devotion to my Guide, **Dr. A. Srinivasan**, Senior Scientist, CSIR-NIIST, for his precious and encouraging supervision, valuable discussions, never failing kindness and channelling me in the right direction throughout the course of this research work. My Co-Guide, **Dr. U.T.S. Pillai**, Chief Scientist, CSIR-NIIST, was always there with me with his sincere efforts and constructive criticisms. A mere 'Thank you' doesn't seem sufficient but it is said with appreciation for his support, encouragement, care, understanding and precious friendship. I am much indebted to him for his valuable advice in my work, spending his precious time to read, and correct my thesis and journal papers. I owe a great debt of gratitude to my well wisher, **Dr. B.C. Pai**, Emeritus Scientist, CSIR-NIIST, for his persistent encouragement and advice during the course of this work. I thank **Dr. Prabhakar Rao**, Head of Department, Material Science & Technology Division, CSIR-NIIST, for the academic support and the facilities provided to carry out the research work at the Institute. I wish to express my warm and sincere thanks to **Dr. Ajayaghosh**, Director, CSIR-NIIST, and **Dr. Suresh Das**, former Director, CSIR-NIIST, for the approving my research journey. I

am very much obliged to **Council of Scientific and Industrial Research (CSIR),** New Delhi for granting Senior Research Fellowship and the financial support for carrying out this research work.

I heartily acknowledge my Ph.D. doctoral committee members: **Dr. S. Savithri**, **Dr. T.P.D. Rajan** and **Dr. S. Ananthakumar** for their timely advices, constructive criticism and positive appreciation. I extend my word of thanks to **Dr. Manilal** and **Dr. Krishna Kumar** for their scientific inputs, personal helps and friendly nature which has always made me feel at ease while working on the AcSIR 800 Project. My earnest thanks to **Dr. Luxmi Varma** and **Dr. Mangalam S Nair,** the present and former AcSIR Co-ordinators for the help rendered and timely conduction of my assessments and other AcSIR formalities. I am very much thankful to **Mr. M.C. Shaji**, and **Dr. M. Ravi** from CSIR-NIIST for their valuable advices and encouragement. I can't imagine any better collaboration than what I had with them. Special thanks are due to **Mr. Pruthviraj** for the XRD analyses, **Mr. M.R. Chandran**, **Mr. Harish, Ms. Haritha** and **Ms. Soumya** from CSIR-NIIST for SEM and EDS facilities. I owe thanks to **Dr. K.R. Ravi** and **Mr. Jayakrishnan**, PSG tech, Coimbatore, for their help, valuable advices and great friendship. My heartfelt thanks to **Mr. V. Antony** and **Mr. T. Soman** for the help received during my experiments in melting and casting. I acknowledge with thanks the help received from **Mr. J. Arun Sankar**, **Mr. M. Giri Sankar** and **Mr. Sarangadharan** for the machining, fabrication and other works. I am particularly thankful to the **Technical** and **Non-Technical staff**, CSIR-NIIST, for their silent but strong contributions throughout my stay at NIIST.

Even though only my name appears on the cover of this dissertation, the real motivators who have been with me through my thick and thin, the ones who need a loud applause are my friends. **Mr. Abhilash Viswanath** and **Dr. K.M. Sree Manu**, our

association goes a long way since days of post graduation and have been with me ever since as friends, labmates and room mates. Thank you for being with me in the ups and downs of life during the past 8 years. Special thanks are due to my seniors **Dr. K.K. Ajithkumar**, **Dr. Arun Boby**, **Dr. E. Jayakumar** and **Mr. Manikandan** for all the love that they have showered upon me. Special shout-out to the inmates of "Kanyakanz": **Mr. Hari Sanil**, **Mr. Mithun Krishnan**, **Mr. Arjun Panicker** and **Mr. B.K. Arjun**; cheers to the bestest of time spent together which will be forever cherished. I greatly value the close personal rapport that have forged over the years with **Mr. Jithu Jayaraj**, **Mr. Rajesh Kumar**, **Ms. Jerin Pancrecious**, **Ms. A.G. Arsha**, **Ms. Ramya Rajan**, **Mr. M.G. Akhil, Mr. Gowtham Kumar, Mr. Nikhil Koshy**, **Mr. S. Arun Kumar**, **Mr. Lavish Kumar**, **Mr. Manu Madhav**, **Mr. K.R. Rajesh**, **Mr. Ajmal Khader**, **Mr. Riyas Mohammed**, **Mr. Vijay**, **Mr. Rahul**, **Mr. Ananthu**, **Mr. Vasudevan**, **Mr. G.K. Arun**, **Mr. Rafi Mohammed**, **Mr. G.K. Arun, Mr. Anil Chacko**, **Mr. N. Anand**, **Mr. Dipin**, **Mr. Vishnu**, **Mr. Adharsh, Mr. Sanjeev**, **Mr. Prince Joseph**, **Mr. Arun Kumar and Mr. Chilambarasan.** It's said that people will walk in and out of your life, but only true friends will leave footprints in your heart. **Mr. Sambhu Mohan, Dr. Arun Sreekumar**, **Mr. Harish Kailas**, **Mr. Nidhin Gopinath**, **Mr. Shinoop**, **Mr. Rahul Mohan**, **Mr. O.M. Prince**, **Mr. Sunil Varghese**, **Mr. Ashok Chitarenjan**, **Mr. Rajesh Rajagopal, Mr. Manoj Manu**, **Mrs. Nimisha Nair**, **Mrs. Jinu Elizabeth**, **Mrs. Meenu Ajayan**, **Mrs. Jamuna**, **Ms. Sharda Sunil Kumar**, **Mrs. Preethi Varghese**, **Ms. Vijitha**… the list is endless. I owe you guys big time! To my colleagues and dear students at Marian Engineering College, your love, support and encouragement is worth more than I can express on paper. I am also very grateful to all my colleagues who helped me in some way or the other during

my NIIST days. I risk doing them a disservice by not mentioning all of them here, but plead paucity of space.

Words and sentences are not enough to thank the biggest source of my strength, my family. My parents, **Mr. N. Ratnakaran** and **Dr. K. Chitra**, always had faith in me and gave me the freedom to pursue whatever I desired in life. I salute you for the selfless love, care, pain and sacrifice you did to shape my life. Although you hardly understood what I researched on, you were willing to support any decision I made. I would never be able to pay back the immense love and affection showered upon me by you. Thanks to my sister, Ms. **K.R. Anju,** for her selfless love, care, occasional annoying and dedicated efforts at all times. From the bottom of my heart I thank **Mr. S. Selvest** (uncle), **Dr. K. Betty** (Aunt), **L. Lalitha Bai** (Grandma), **Dr. S. Neethu**, **Dr. S. Geethu** and **Mr. Kannan** (Cousins) for the unwavering love and support provided in every possible way to see the completion of this work.

I thank **God**, the almighty, for providing me this opportunity and granting me the strength and patience to complete the research successfully.

Athul K.R.

Chapter 7 Summary & Conclusions

List of Tables

List of Figures

Synopsis

Due to low density, magnesium is a potential '***metal for the future'***. Besides its use as alloying element in aluminum alloys, titanium, and steel production; magnesium alloys are also considered as replacements for aluminum alloys to make the components lighter and stronger. Good solid solubility of Gd in Mg makes it an ideal alloying element to achieve solution strengthening and precipitation strengthening thereby enhancing the room and high temperature properties. The Gd phases also favor the formation of protective films to improve the corrosion resistance of the alloy. The so-called ''scavenger effect'' of RE on corrosion resistance of magnesium alloys taps the impurity elements such as Fe and Cu to form intermetallic compounds, thereby reducing their content in the alloy. The microstructures of Mg-Al alloys are composed of α-Mg solid solution, and the eutectic mixture (α-Mg + β-$Mg_{17}Al_{12}$). The presence of low melting point $Mg_{17}Al_{12}$ phase in Mg-Al alloys limits its strength and creep properties at elevated temperatures and make them unsuitable for power train applications in automobile industry. This opens the door for the development of new Mg-Al alloys with thermally stable intermetallic phases. Gadolinium (Gd) is one of the rare earth elements that can reduce the formation of β-$Mg_{17}Al_{12}$ phase by consuming Al to form thermally stable Al_2Gd phase and also it has an electrochemical potential almost near to that Mg.

The presence of I-phase in Mg-Zn-RE alloys results in excellent mechanical performance at room and elevated temperatures. Mg-Zn-Y alloys have been extensively studied and the microstructure consists of different phases, such as I, W and X phases, depending on the Zn/Y atomic ratio, thus resulting in different mechanical behaviors. However, the Mg-Zn-Gd system is relatively new, and has not been investigated in

detail. Hence, to tailor make new Mg-Zn-Gd alloys with high strength and corrosion resistance, a thorough investigation on the structure-property correlation of these alloys is essential with varying Zn/Gd ratios. Development of quaternary RE alloys with enhanced RT and HT properties are still underway.

Ca is known as a potential grain refiner and can improve the strength and creep resistance by the formation of thermally stable phases. Further, by the addition of Ca, melt oxidation is reduced during casting and also oxidation during heat treatment process. Hence, in the present research work, Ca content in different wt.% are added to the optimal Mg-Al-Gd and Mg-Zn-Gd to study the property enhancement.

In a nutshell, ternary Mg-Al-Gd and Mg-Zn-Gd alloys are comparatively new, and has not been investigated in detail. Hence for the development of new ternary and quaternary alloys (Ca addition) with high strength (at room and elevated temperature) and corrosion resistance, a thorough knowledge on the structure-property correlation of these alloys is essential.

Chapter 1 Introduction

1.1 General Background

Magnesium (Mg), with a density of 1.7 g/cc, which is two third of aluminum (2.7 g/cc) and less than one fourth of steel (7.8 g/cc), is the lightest available structural material and can be used as a promising candidate in this scenario. Besides, Mg alloys have added advantages such as excellent specific strength and stiffness, good dimensional stability, high damping capacity and high recyclability. The past half century has witnessed a worldwide growth in the application of magnesium and its alloys as novel light materials for the overall weight-reduction in the aeronautical and automotive industry. The prime challenges faced by automotive industries are energy crisis and global warming, hence the design and development of 'safer and cleaner' vehicles is the subject of research globally. It is surveyed that 65-75% of the fuel consumption in automobiles is related to the weight and a 10% reduction in vehicle weight can lead to approximately 7% reduction in fuel consumption and thereby reduction in greenhouse gas emission.

The most commercially used Mg alloys like the AZ91, AM50, AM60, AS21 etc offer a combination of excellent castability, corrosion resistance, good room temperature properties and high ductility [1,2]. However the use of these alloys in the automobile and electronic industries are restricted to low-temperature applications. The presence of low melting point $Mg_{17}Al_{12}$ phase in these alloys limits their strength and creep properties at elevated temperatures and make them unsuitable for power train applications in automobile industry [3-5]. Hence, research attempts are underway for the development of Al less or Al free Mg alloys suitable for high temperature applications. This situation opens the door for the development of new Mg alloys which

can suppress the formation of $Mg_{17}Al_{12}$ phase by the formation of thermally stable phases. Addition of rare earth (RE) elements are found to be a promising method to enhance the mechanical strength and creep resistance at elevated temperature. The solid solution hardening and precipitation hardening caused by RE addition contributes to the improvement of the strength. Yttrium, cerium, lanthanum, gadolinium and neodymium are mainly used as rare earth elements for alloying. Microstructure of Mg-Al alloys consist of α-Mg and $Mg_{17}Al_{12}$. With the addition of almost all rare earths, microstructure is refined, amount of $Mg_{17}Al_{12}$ is decreased and new Al_2RE or $Al_{11}RE_3$/Al_4RE phases are formed. Gadolinium (Gd) is one of the active rare earth elements that have high affinity to aluminium and thus can reduce the formation of β-$Mg_{17}Al_{12}$ phase by consuming aluminium to form thermally stable intermetallic Al_2Gd phase and also it has an electro chemical potential almost near to that Mg [6-8]. Expanding the potential application of Mg-Al is the primary purpose of the study. Hence, studies on increasing the application of Mg-Al magnesium alloy for powertrain application with supportive corrosion resistance and wear with individual and combined effect of Gd with Ca is highly essential.

Next to Mg-Al alloys, Mg-Zn alloys show a good combination of mechanical properties and corrosion behavior [9,10]. Zn is known to increase age hardening response as it produces intermetallic compounds and refines the grain size. A small amount of Zn contributes to overall strength due to solid solution and precipitation strengthening [10,11]. Microstructure observation reveals that the addition of Zn element significantly refined the grain size of as-cast Mg-Zn alloys and increased the volume percent intermetallic in the microstructure [12]. The deleterious effects of metallic impurities like Fe and Ni can also be reduced by the addition of Zn [13]. With RE additions, Mg-Zn-RE alloys have been developed and has been heavily studied due

to the presence of peculiar secondary phases, e.g. icosahedral quasicrystalline phase (I-phase) and long period stacking ordered (LPSO) phase, which result in excellent mechanical performance at room and elevated temperatures [14,15]. The relation between composition, microstructure and properties of Mg-Zn-Y based system in both as cast and heat treated conditions is well documented in the literature. However, the Mg-Gd-Zn system is relatively new, and has not been investigated in detail. Hence, to develop new Mg-Gd-Zn alloys with high strength, high creep and corrosion resistance, a thorough knowledge on the structure-property correlation of these alloys is essential with different Zn/Gd ratios. Mg-Zn-Gd is one of the very important systems as its microstructure consists of many different phases, such as I, W, X and laves phases, depending on the ratio of Zn to Gd contents, thus resulting in different mechanical behaviors. In the present investigation, Mg-Zn alloys containing individual and combined effect of Gd with Ca were prepared, and their microstructure, mechanical corrosion and wear properties were evaluated in the as-cast condition.

Thus the present study, ***"Structure - Property Evaluation of Gd & Ca Added Mg-Al & Mg-Zn Alloys",*** aims to investigate the effect of varying Gd addition on the mechanical, corrosion and wear properties of Mg-Al and Mg-Zn alloys. Further, the modification of the optimal tested Mg-Al-Gd and Mg-Zn-Gd alloys with varying Ca addition has been carried out. The modification mechanisms, formations of different intermetallics compounds and their strengthening mechanismsare studied in detail.

1.2 Objectives of the Investigation

The primary objectives of the present work are:

- Study the effect of Gd on microstructure, mechanical, corrosion & wear properties of Mg-9Al alloys and Mg-5Zn alloys.
- Correlation of microstructures of the developed alloys with mechanical, corrosion

and wear properties.

- Modification of the optimal Mg-Al-Gd and Mg-Zn-Gd alloys with different percentage of Ca (0.5, 1 and 2 wt.%) and study their microstructural, mechanical and corrosion properties.

1.3 Lay out of the Thesis

The thesis is divided into seven chapters and the contents are discussed in brief as follows:

Chapter 1 deals with the general background as well as the challenges and motivation to pursue the present work. An overview of the objectives and scope of the work is also presented.

Chapter 2 presents the relevant information in the field of Mg and its alloys. The proposed research is originated based on previous research work. Further the detailed reviews of processing, mechanical, corrosion and tribological properties of RE added and Ca modified Mg-Al and Mg-Zn alloys are outlined. The literature review aims to produce a rationale and justification for the present work.

Chapter 3 deals with the selection of raw materials, description of experimental apparatus, processing conditions and modification treatment. The synthesis of the Mg-Al and Mg-Zn alloys prepared by liquid state processing is also described in detail. Besides, the specimen preparation and characterization for XRD, metallography (optical microstructure and SEM-EDX), mechanical (hardness, tensile and creep), corrosion (immersion and electrochemical) and tribological properties are explained.

Chapter 4 presents the detailed microstructural analyses of the Mg-Al-Gd and Mg-Zn-Gd alloys using optical microscope and SEM. Phase analysis (XRD and SEM-EDS)

and chemical composition of the alloys studied are discussed. The different intermetallic compounds formed during the Ca modification have also been identified and analyzed.

Chapter 5 deals with the evaluation of mechanical properties such as hardness, room as well as high temperature tensile properties and creep properties of Mg-Al and Mg-Zn alloys with varying amount of Gd and Ca. These properties are correlated with the microstructures.

Chapter 6 comprises the corrosion study (immersion and electrochemical test) of the developed alloys are performed in 3.5 wt.% NaCl. Dry sliding wear behavior of the Mg-Al-Gd alloys with different loads are examined and discussed with respect to the wear scar width (WSW). Attempts are also made to correlate the wear properties of the alloys with the microstructures.

Chapter 7 summarizes the outcome of the overall work, emphasizingon the major conclusions drawn from different chapters.

A critical analysis of the results provides ideas and directions for further investigation, which are discussed in the **'Scope of Future Work'** section.

The references cited in each chapter are given at the end. In addition, figures and tables are numbered independently in each chapter.

Chapter 2 Literature Review

2.1 Introduction

One of the major concerns since the beginning of automobiles is the energy efficiency and it is observed that a 10% reduction in vehicle weight can lead to approximately 7% increase in fuel economy and an appreciable reduction in greenhouse gases. Magnesium is the best suitable candidate considering the above needs. Magnesium is alloyed with other metals to tailor make a wide variety of properties, both to increase the manufacturability and the product properties [16-18]. A review of literature existing in the area of processing, properties and different modification techniques of RE containing Mg alloys are discussed. Influence of RE and Ca addition on the physical and mechanical characteristics of various Mg-Al and Mg-Zn alloys are reviewed in detail. Besides, the modification concepts, methods, mechanisms and the influence on mechanical properties are reviewed thoroughly.

2.2 Magnesium

2.2.1 History of Mg

In 1755, a Scottish scientist, Joseph Black recognized that magnesia contains magnesium but he was unable to produce pure Mg metal but in 1808 an English chemist, Sir Humphry Davy isolated Mg metal for the first time. The name 'magnesium' comes from the Greek word for a district in Thessaly called Magnesia. Magnesium is the 8th most abundant element in the earth's crust. Typical ores of magnesium are dolomite ($MgCO_3.CaCO_3$), magnesite ($MgCO_3$), serpentine ($Mg_3Si_2O_5(OH)_4$), carnallite ($KCl.MgCl_2 \cdot 6(H_2O)$) and as well as from sea water. Therefore, it can be said that magnesium is an almost inexhaustible resource. Method of producing magnesium

is mainly divided into two; electrolysis of fused anhydrous magnesium chloride ($MgCl_2$) and thermal reduction of magnesium oxide (MgO) by FeSi and the ores used in the production of magnesium are dolomite and magnesite. The electrolytic process involves the reduction of the Mg ion that is recovered from magnesite or seawater. Magnesium oxide or sulphate is converted into magnesium chloride ($MgCl_2$) brine and then into clean and dry $MgCl_2$ powder which on electrolysis gives chlorine gas and Mg metal close to 700 °C. The thermal reduction process, which is also called the Pidgeon process, is based on the reduction of metallic Mg from dolomite. In this process dolomite is reduced by supplying ferrosilicon and thermal energy. It is heated at high temperature in a retort furnace under a vacuum. Magnesium oxide (MgO) and dolomite react with ferrosilicon and release Mg in vapor form which condenses at the end of the retort furnace wall, subsequently melted, and cast as pure Mg ingots. While the pidgeon process is carried out as a continuous process, the electrolytic process is a batch process. After extraction, crude magnesium metal is shifted to cast shops for impurity removal, alloying element addition and transformation into billets, ingots, and slabs. During melting, molten magnesium and alloys are protected from oxidation and burning by gas such as sulfur hexafluoride or sulfur dioxide. For shipping and handling under severe climatic conditions, suitable paper wrappings or ventilated plastic are essential to prevent corrosion.

2.2.2 Properties

Mg is a highly attractive metal due to its low density compared to other common structural metals. It is almost two-third that of Al (2.7 g/cm^3) and a quarter that of steel (7.84 g/cm^3). The melting point of magnesium is 650 ^oC and its boiling point is 1107 ^oC. Mg has better heat dissipation and transfer owing to its high thermal conductivity of 156 W/mK. It also has a higher specific heat value of 1025 J/kgK.

Therefore, its machinability, turning, milling, and drilling processes are better than those of other metals. The modulus of elasticity of Mg alloys is relatively low at ~45 GPa, compared to ~70 GPa and ~210 GPa for Al alloys and steel, respectively. Furthermore, the tensile and yield strengths of Mg are relatively low. However, its specific strength (strength/density) is high compared to other metals. Table 2.1 presents the most essential physical and mechanical properties of pure Mg in comparison to Al and Fe [19-22].

Table 2.1 *Properties of pure Mg in comparison with Al and Fe.*

Property	Unit	Mg	Al	Fe
Atomic number		12	13	26
Atomic radius	pm	160	143	126
Atomic weight	$gmol^{-1}$	24.3	26.98	55.85
Density	gcm^{-3}	1.74	2.7	7.87
Melting point	^{o}C	650	660	1536
Boiling point	^{o}C	1090	25.19	2861
Thermal conductivity	$Wm^{-1}K^{-1}$	156	238	80
Specific heat	J/kgK	1025	900	460
Volume heat capacity	$J\ m^{3}\ x10^{-3}$	1783	24.3	3630
Electrical resistivity	ohm-m $x\ 10^{-8}$	4.45	2.65	9.7
Elastic modulus	GPa	45	70	210
Strength	MPa	90	98	275
Specific strength	$m\ x\ 10^{6}$	52	36	34

2.2.3 Structure

At room temperature, the Mg lattice parameters (a = 3.2092 Å and c =5.2105 Å with c/a ratio of 1.6236) are close to the hexagonal packed structure. The atomic positions, principal planes and directions are illustrated in Fig. 2.1 [23].

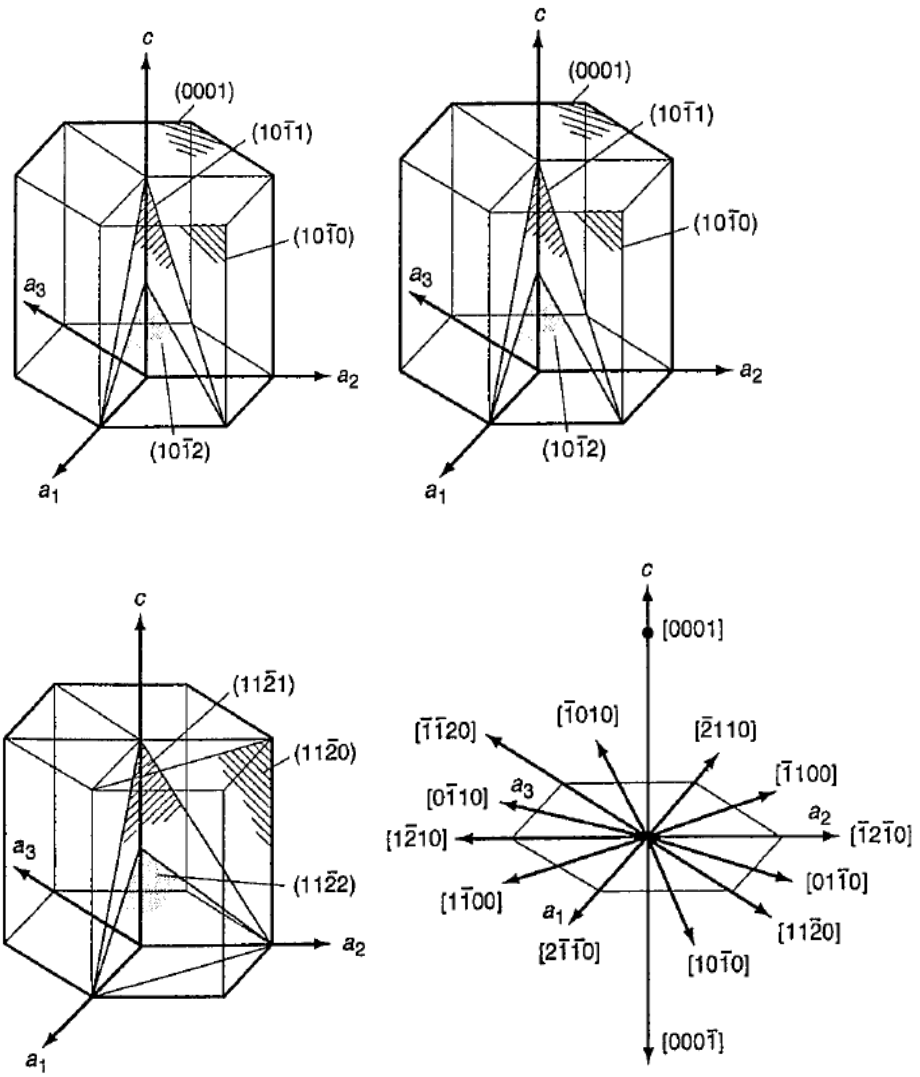

Fig.2.1 *The atomic positions, principal planes and directions of Mg.*

Table 2.2 *The slip parameters of Mg.*

Slip system	Burgers Vector type	Slip direction	Slip plane	No of slip system	
				Total	Independent
1	a	<11$\bar{2}$0>	basal plane {0001}	3	2
2	a	<11$\bar{2}$0>	1st order prism plane {10$\bar{1}$0}	3	2
3	a	<11$\bar{2}$0>	1st order pyramidal plane {10$\bar{1}$1}	6	4

4	c + a	<11$\bar{2}$3>	2nd order pyramidal plane {11$\bar{2}$2}	3	2
5	c	<0001>	1st order prism plane {10$\bar{1}$0}	3	2
6	c	<0001>	2nd order prism plane {11$\bar{2}$0}	3	2

Table 2.2 shows the slip parameters of Mg. At room and elevated temperatures, primary and secondary slip and twinning occur because the primary slip takes place on the (0001) basal plane and in the <1120 > most closely packed direction of the plane at RT and the secondary slip occurs in the <1120 > direction on the {1010} vertical face planes. Primary twinning happens across the {1012} planes and the secondary twinning occurs {3034}. At elevated temperatures, slip also occurs in the <1120> direction on the {1010} pyramidal planes and the twinning occurs across the {1013} planes [23].

2.3 Advantages of Mg

Magnesium is called ***"metal of the future"*** for a reason. The main advantage of magnesium alloy over another material is its low density. Besides being a component in titanium, aluminum alloys, and steel production, magnesium can also be cast into various mechanical parts and can replace aluminum alloys for anything that needs to be made lighter and stronger. Nowadays, magnesium is making more headlines because the automobile industry is starting to use more magnesium in auto parts due to the looming EU emissions and CAFE standards. The US EPA CAFE (Corporate Average Fuel Economy) standards require automobile manufacturers to enhance average fleet miles per gallon by 15% to 34.1% by 2017 from the current 27.3 average mpg. In addition, the Obama administration's new CAFE standards require vehicles to average 54.5 mpg by 2025, which is about 100% improvement from where we are today! With

these tough laws in place, automakers are looking up to magnesium to reduce the vehicle weight to meet the stringent mpg guidelines. Luckily for automakers, almost all of their auto parts, from engine blocks, wheels, panels, or the entire roof top can be fabricated from magnesium alloys. The other advantages are the high specific strength, specific stiffness, superior damping capacity, electromagnetic shielding capacity, excellent machinability and good castability [23]. Due to its excellent fluidity, magnesium alloy can be casted easily with relatively low tooling cost and energy consumption. Casting of thin wall parts (2 mm) is possible by using Mg alloys mainly because of its excellent fluidity. Magnesium castings experience high cooling rate due to its low volumetric specific heat. Thus, magnesium castings allow faster cycle times compared with aluminum and zinc. Due to its low density, high gate pressure can be achieved at moderate ram pressure. The steel dies used for Mg alloy casting last two or three times longer than with Al alloys because of the low solubility of iron in liquid magnesium and less heat per volume of magnesium die-casting alloys. Magnesium and its alloys offer excellent damping capacity, so it helps to decrease vibration and noise in many purposes like vibration testing fixtures and mounting brackets for electronic equipment. Magnesium alloys have lower resistance to cutting than other structural metallic materials. So, higher speed with good feed rates and greater depths of cut are thus possible. Also, less power is required to remove a given amount of Mg in comparison to other commonly machined metals [24].

2.4 Limitations of Mg

In spite of all these advantages, there are some limitations responsible for the lack of magnesium applications in different fields. They are:

(1) Low elevated temperature properties

(2) Highly corrosive and chemically reactive

(3) Limited cold workability and stiffness

(4) High cost of recycling

2.5 Mg Alloys

Magnesium alloy, being a mixture of Mg metal with metals or metalloids, leads to alteration in properties such as strength, ductility, workability, corrosion resistance and castability. Mg is chemically active and alloying magnesium leads to the formation of intermetallic compounds which influence the microstructure, thereby affecting the various properties of Mg alloys.

2.5.1 Alloying Elements

Pure Mg being too soft to use in industrial applications, has to be alloyed to enhance its properties such as creep resistance, strength, ductility, etc. Aluminum (Al), rare-earths (RE), zinc (Zn), calcium (Ca), manganese (Mn), silicon (Si), strontium (Sr), etc. are the commonly used alloying elements in Mg alloys. Their applications is however dependent on the desired performance. Mg alloys can be described not only by the chemical composition but also by the phases present in the alloy. This can be illustrated for binary and ternary systems in the form of phase diagrams, which show only the equilibrium condition. They do not provide information regarding the physical shape or dispersion of the phases that might emerge in non-equilibrium processing. In this section, the most significant alloying elements and their alloying effects are discussed.

2.5.2 Effects of elements addition on Mg

Aluminum (Al). Al is one of the most common alloying element in Mg, as it has the most favorable influence on Mg. Addition of Al enhances the castability, fluidity, strength and corrosion properties of Mg-Al alloys. The alloys containing more than 6

wt.% of Al can be heat treated. Al gives solid solution strengthening, and beyond 2 wt.% addition, the precipitation of the β-$Mg_{17}Al_{12}$ phase occurs which enhances hardening. However, addition of Al increases the tendency for shrinkage with micro porosity up to 9% and then reduces it [25].

Zinc (Zn). Zn is generally used as alloying element for magnesium alloy to enhance room temperature strength. It often increases solid solution strengthening effect and fluidity. The solid solubility of zinc in magnesium at room temperature is around 2% and 6.2% at 345 ^{o}C. However, beyond a certain limit it is susceptible to hot cracking in Mg-Al alloys. Small amount of Zn can be dissolved in Mg, as solution strengthening element, while excess Zn will react with Mg to form (Mg, Zn) containing phases. It is usually used in addition to Al to enhance strength without reducing ductility. Moreover, Zn addition to Mg alloy with Ni and Fe impurities can assist in improving the corrosion resistance [26].

Beryllium (Be). Be is added in smaller quantities to reduce the surface melt oxidation significantly during the melting, casting and welding processes. Be can also lead to grain coarsening [27].

Calcium (Ca). Calcium helps in grain refinement, enhanced creep and corrosion resistance, thermal and mechanical properties. Melt oxidation is reduced during casting and also oxidation during heat treatment process. Its presence also results in better rollability of Mg sheet. With amount exceeding 0.3 wt.%, the sheet will be prone to cracking during welding [28,29].

Cerium (Ce). Minor addition of cerium (0.2%) significantly increases elongation. The presence of Ce in Mg altered the texture of extruded rods during recrystallization thereby enhancing plastic deformation capability. In the Mg-Ce material, both twinning and slip occur while in Mg only twinning dominates. The addition of Ce reduces the

yield strength and increases the work hardening rate that delays the onset of instability [27].

Copper (Cu). Copper has limited solid solubility in Mg. Cu reacts with Mg to form Mg_2Cu intermetallics. Studies have indicated that addition of Cu assists in increasing the room temperature and high temperature strength; however, the ductility is compromised. It may also be noted that Cu addition can unfavorably influence the corrosion resistance [30,31].

Iron (Fe). Even in small quantities, Iron is detrimental to the corrosion resistance. 0.005% Fe content is the upper limit allowed for the best protection against corrosion [27,32].

Lithium (Li). Li addition decreases the density of alloys below that of unalloyed Mg, due to its low relative density of 0.54. Its addition leads to decrease in strength and increase in ductility

Manganese (Mn). Mn addition enhances the salt water corrosion resistance of Mg-Al and Mg-Al-Zn alloys. The low solubility of Mn in Mg limits the amount of Mn addition and is usually incorporated with other alloying elements like Al [32].

Molybdenum (Mo). Increasing the weight percent of Mo (0.7, 2.0, and 3.6wt.%) in Mg resulted in an improvement in hardness, elastic modulus and ductility with marginal decrease in strength. [31].

Nickel (Ni). The incorporation of Ni in Mg leads to the formation of Mg_2Ni intermetallics and an increase in room temperature strength with a simultaneous decrease in ductility was observed. Nickel additions (even in minute quantities) have an adverse effect on the corrosion resistance.

Neodymium (Nd). RE elements are added to increase the high temperature strength, creep resistance and corrosion resistance. However, as rare earths are costly, they are

primarily used in high-tech alloys. Their presence also assists in reducing the freezing range of the alloys, which leads to reduction in casting porosity and weld cracking. Addition of Nd enhances the strength of Mg. This is attributed to the solubility limits of Nd and the formation of stable precipitates within the grain structure and at grain boundaries.

Yttrium (Y). Yttrium has a relatively high solid solubility in Mg (12.6 wt.%, 3.75 at.%) It is incorporated in other rare earth metals to enhance the high temperature strength and creep performance [34].

Silicon (Si). Silicon can increase the fluidity of molten alloys. However, if it is used together with iron, the corrosion resistance will be compromised

Silver (Ag). When combined with rare earths, gives improved high temperature strength and creep resistance [22].

Strontium (Sr). Strontium is normally added combined with the other major alloying elements resulting in enhanced creep performance but YS and UTS remains almost unchanged [20].

Thorium (Th). The addition of thorium shows an improvement in creep strength up to 370 °C. In Zn containing alloys, the addition enhances the weldability. However, the radioactive nature of thorium, hinders its applications.

Tin (Sn). Tin combined with Al in Mg enhances ductility. During forging, it also assists in reducing cracking [32].

Titanium (Ti). There is very low mutual solubility of Ti and Mg in each other. Hassan et al.[21] reported that respective additions of 2.2 and 4.0 vol% of Ti in Mg led to an increase in 0.2% yield strength and ductility. No intermetallic compound was seen to be formed.

Zirconium (Zr). Zr is an excellent grain refiner when incorporated into the alloys

containing Zn, Th, REs, or a combination of these. However, due to the formation of stable compounds with Al or Mn, it cannot be used with these elements. Zr also forms stable compounds with Fe, C, O and H that are present in the melt [32].

2.5.3 Designation

The American Society for Testing and Materials (ASTM B 275) categorized magnesium alloys according to their alloying elements and the naming method denotes the appropriate chemical composition by weight. In this method, the alloys are designated by an alpha numerical code as explained below:

First Part: Indicating the two principal alloying elements/metals. Two code letters representing the two main alloying elements are arranged in order of decreasing percentage (or alphabetically if the percentages are equal). ***A*** *- Aluminium****, B*** *- Bismuth****, C*** *- Copper,* ***D*** *- cadmium,* ***E*** *- Rare earth,* ***F*** *- Iron,* ***G*** *- Magnesium,* ***H*** *- Thorium,* ***K*** *- Zirconium* ***L*** *- Lithium,* ***M*** *- Manganese,* ***N*** *- Nickel* ***P*** *- Lead,* ***Q*** *- Silver,* ***R*** *- Chromium,* ***S*** *- Silicon,* ***T*** *- Tin,* ***W*** *- Yttrium* ***Y*** *- Antimony,* ***Z*** *- Zinc.*

Second Part: Indicating the amount of the two principal alloying elements/metals consisting of two numbers corresponding to rounded-off percentages of the two main alloying elements and arranged in the same order as alloy designations in part of whole numbers.

Third Part: Differenciate between different alloys with the same percentage of two principal alloying elements. It consists of a letter of the alphabet assigned in the order as compositions become standard letters of alphabet except I and O.

Fourth Part: Indicating condition (temper). Consisting of a letter followed by a number (separated from the third part of the designation by a hyphen). ***F*** *- as fabricated* ***O*** *- as annealed* ***H10*** *and* ***H11*** *- slightly strain hardened* ***H23, H24*** *and* ***H26*** *- strain hardened and partially annealed* ***T4*** *- solution heat treated* ***T5*** *- artificially aged only*

T6 *- solution heat treated and artificially aged* ***T8*** *- solution heat treated, cold worked and artificially.*

For example, consider the magnesium alloy AZ81A-T4. The first part of the designation, AZ, indicates that aluminium and zinc are the two major principal alloying elements. The second part, 81, indicates the highest weight percentages of aluminium and zinc (8 and 1 respectively). The third part, A, indicates that it is the fifth alloy standardized with 8% Al and 1% Zn as the principal alloying additions. The fourth part, T4, indicates that the alloy is solution heat-treated. The Mg alloys can be classified into three categories depending on the increasing demand for specific properties like specific strength, ductility and creep resistance in the automotive industry, as shown in Fig. 2.2 [17]. Some examples of common magnesium alloys are given in Table 2.3.

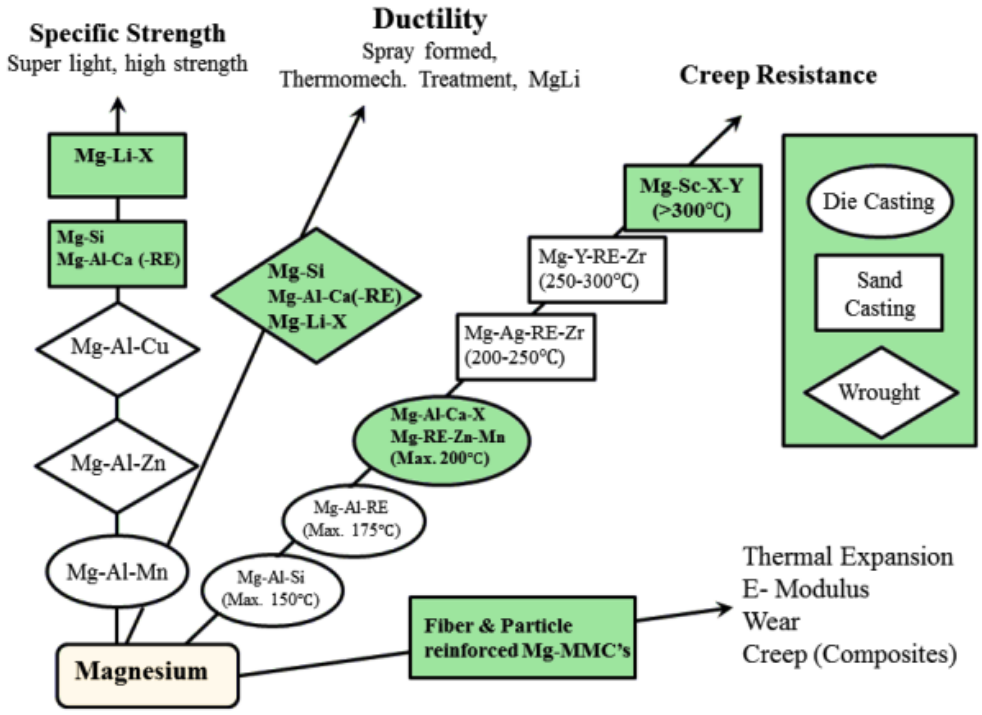

Fig. 2.2 *Classification of Mg alloys based on specific properties [17].*

Table 2.3 *Common magnesium alloys and their applications.*

Alloy Designation	Alloying Additives	Uses	Reasons for usage
AZ91	9.0% Al 0.7% Zn 0.13% Mn	General casting alloy	Good castability, good mechanical properties at T<150ºC.
AZ31	3.0% Al 1.0% Zn 0.2% Mn	Wrought products	Good extrusion alloy.
AM60	6.0% Al 0.15% Mn	High pressure die casting alloy	Greater toughness and ductility than AZ91, slightly lower strength. Often preferred for automotive structural applications.
ZE41	4.2% Zn 1.2% RE 0.7% Zr	Specialist casting alloy	Rare earth addition improves creep strength at elevated temperatures. Pressure tight.
AS41	4.2% Al 1.0% Si	General casting alloy	Better creep resistance than AZ91 at elevated temperatures but lower strength.

2.6 Applications of Mg alloys

The wide spectrum of magnesium alloy applications is discussed below. The principal applications are found in the automotive and aerospace industries because of environmental and performance gains.

2.6.1 Automotive sector

The pioneer use of magnesium in the automotive sector was first explored by Volkswagen (Beetle) with about 25 kg of magnesium castings in the transmission housing of air-cooled engine. With the development of more efficient water-cooled automobile engines, the 50 years of magnesium usage came to an end. In 1996, VW/Audi started with the B80 gearbox housing. Daimler Chrysler (Mercedes Benz), BMW, Ford and Jaguar used magnesium as a structural lightweight material. At

present, about 14 kgs of magnesium components are used in the VW Passat, Audi A4 & A6, especially for transmission casings, offering a 25% weight savings over aluminium. The Corvette Z06 uses magnesium roof components and magnesium engine cradle to minimize mass. Thanks to magnesium parts, the Corvette Z06 is one of the lightest high-performance vehicles on the market. Ford Explorer, the 2011 North American Truck of the Year, uses magnesium seat frames for its third-row passenger seats. The Chrysler Group employs magnesium in the interiors of its Grand Cherokee, Wrangler and Patriot models. Its instrument panels and front consol are made out of a single-piece magnesium die cast. Other applications of Mg include instrument panels, intake manifolds, cylinder head covers, inner boot lid sections and steering components which utilize more ductile AM50A and AM60B alloys. AS41 is used to make automatic transmission clutch pistons and stators [24,34]. The GM full-sized Savana and Express Vans use up to 26 kg of magnesium alloy [35]. Fig. 2.3 depicts the components made of Mg alloy and obtained weight reduction and Table 2.4 shows the list of the cars using magnesium alloys and components made of Mg alloys.

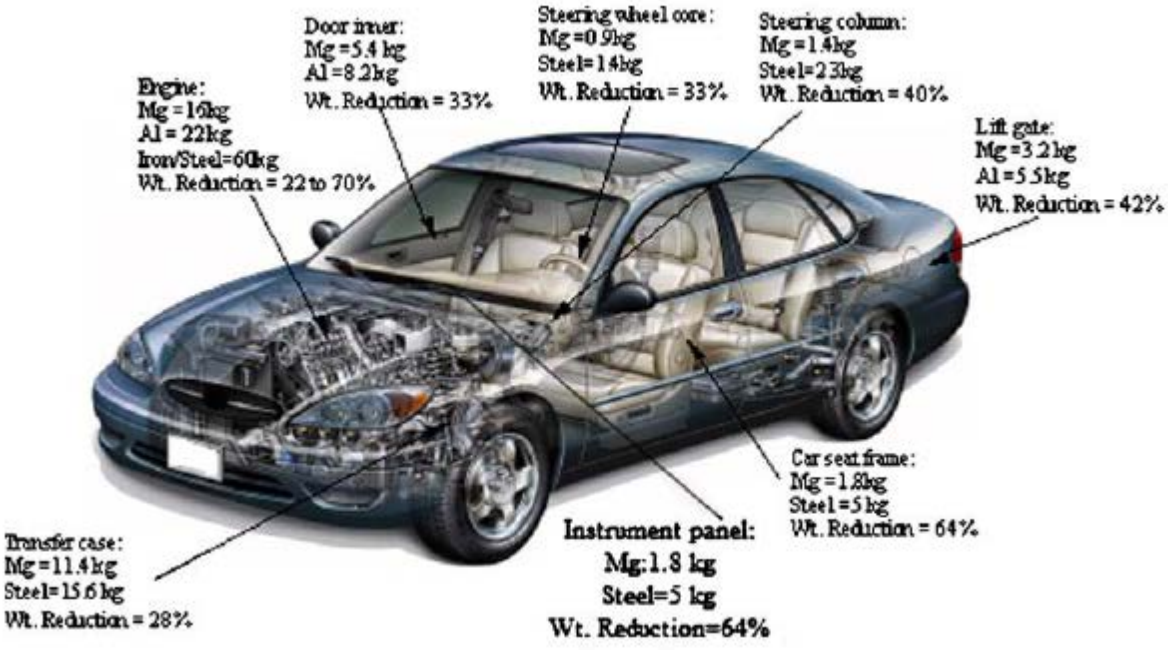

Fig. 2.3 *Some automotive components made of Mg alloy.*

Table 2.4 *Cars using Mg alloys components.*

Component	Producers and car models
Engine block	BMW
Steering wheel frame	Ford (Ford Thunderbird, Cougar, Taurus, Sable), Chrysler Toyota, BMW Lexus LS430
Seat frame	Mercedes-Benz Roadster 300/400/500 SL, Lexus LS430
Instrument panel	GM, Chrysler jeep, Ford, Audi A8, Toyota Century
Wheel rims	Toyota 2000GT, Toyota Supra, Alfa Romeo GTV, Porsche AG 911 Series
Cylinder head	Dodge Raw, Honda City Turbo, Alfa Romeo GTV, AutoZAZ-Daewoo
Clutch case	AutoZAZ-Daewoo Tavria, Slavuta, Daewoo-Sens, Volvo Motors LCP,Alfa Romeo GTV
Transmission case	AutoZAZ-Daewoo Tavria, Slavuta, Daewoo-Sens, Volvo Motors LCP, Porsche AG 911 Series, Volkswagen Volkswagen Passat, Audi A4,A6, Mercedes-Benz
Lower crankcase	Chrysler jeep, Alfa Romeo GTV, GM (Oldsmobile), McLaren Motors F1-V12
Cylinder block	GM Pontiac Gran AM, Corvette
Intake manifold	GM V8, Chrysler
Steering link bracing	GM LH Midsize
Camshaft drive chain case	Porsche AG 911 Series
Air intake system	BMW V8 motor
Oil pump body	McLaren Motors F1-V12
Gear controls housing	AutoZAZ-Daewoo Tavria, Slavuta, Daewoo-Sens

2.6.2 Aerospace sector

Since 1930's, magnesium has been extensively used in a variety of aerospace applications. Magnesium Elektron alloys combine weight saving high mechanical strength to provide a versatile material for use in aircraft interior applications leading to improved customer experience, better fuel efficiency and increased range. Elektron 43

alloy developed by Magnesium Elektron, passed rigorous tests conducted by the U.S. Federal Aviation Administration (FAA) Fire Test Working Groups, which subsequently lifted long-standing restrictions on the use of magnesium alloys in commercial aircraft interiors. By following the guidelines Elektron 43 alloy is setting the standard for the reintroduction of magnesium into aircraft interiors. The aircrafts using magnesium alloys components are Lockheed F-80C with complete magnesium construction, Northrop XP-56 Black Bullet with magnesium airframe and welded skin, Boeing B47 with 5500 kg of magnesium or Russian TU 95, Convair B-36 bomber containing 8600 kg, and TU 134 with 1550 kg and 780 kg of magnesium, respectively [36]. Magnesium is used in the thrust reversers for the Boeing 737, 747, 757, and 767 as well as in aircraft and helicopter transmission casings and engines. Missiles and spacecraft also contain magnesium and its alloys. Lift-off weight reduction is of prime importance in the design and a material is that can withstand the extreme conditions during operation is essential. Magnesium is capable of withstanding extreme elevated temperatures, impact of high energy particles and exposure to ozone. It is also used in large quantity in intercontinental ballistic missiles such as Titan, Atlas and Agena. Table 2.5 shows the list of the aircrafts using magnesium alloys and components made of Mg alloys.

Table 2.5 *Aircrafts using magnesium alloys components.*

Aircraft	Component	Material
Boeing 737, 747, 757, 767	Thrust reverse cascade casting	AZ92A
Roll Royce	RB211 gear box	EZ33A
General Dynamic F16, General Electric F110 Engine	Accessory drive gearbox	QE22
Sikorsky CH53D Sea Stallion	Transmission casing	AZ91E
Sikorsky UH53D Blackhawk	Transmission casing	ZE41
Sikorsky S92	Main transmission casing	WE43

2.6.3 Nuclear and defense industries

Due to the convenient properties such as low neutron absorption, good thermal conductivity, excellent compatibility with uranium and non diffusivity into uranium, magnesium is used as canning material in graphite moderated gas-cooled power reactors such as Calder Hall and the French EL2, 62 and G3 reactors. Magnesium alloys also have good applications in military and defense instruments such as armored vehicles, portable group equipment, stingray torpedoes, and radar equipment. Anti-tank ammunition rounds have been a primary use of magnesium extruded bar. Military industry extensively uses fine and atomized powers in the range of flare and ordinance applications, particularly decoy flares and illumination flares. Ground illumination flares are designed to dive by parachute and illuminate ground terrain and targets. Mg alloys such as EZ33 (Mg-2.7Zn-0.7Zr-3.2MM) are used in the “Skylark” research rockets. ZK51 (Mg-4.5Zn-0.7Zr) and ZE41 castings have been used extensively for structural parts in missiles because of their high specific strength and rigidity coupled with ease of fabrication [34].

2.6.4 Electronic industry

The use of Mg alloys is of great interest in electronic industry, mainly they are light weight, non-magnetic, and they can block electro-magnetic waves and minimize the influence of noise. But being metallic, they can radiate and conduct heat better than plastic and maintain a metallic texture. Some examples are computer housing, mobile telephone cases, etc. Thinner and lighter laptops, cell phones, and cameras that are durable to withstand the daily wear and tear are the pick of the day. Mg can make a big difference in the manufacture of these fragile products. The new HP Elite Book uses a magnesium base and aluminum-clad magnesium display enclosure and case that protects the laptop from the usual shock, drop, heat, humidity, vibration, pressure, and

protects the display from expensive repairs. Canon's new EOS D50 SLR digital camera is protected by a Mg casing that allows the camera to resist moisture better than its competitors and it weighs only 25.7 ounces. In addition to the excellent strength to weight ratio of Mg, it is also 100 times better than plastic for heat dissipation.

2.6.5 Medical field

As a lightweight metal with mechanical properties similar to natural bone, Magnesium is considered as a convenient metal for the construction of temporary biodegradable medical implants like screws, open-porous scaffolds or stents, which are successfully implanted to fix or repair the fractured bones or to repair damaged blood vessels. Advantages such as in-vivo degradation via corrosion in the electrolytic environment of the body, Mg-based implants have the potential to serve as biocompatible, osteoconductive, degradable implants for load-bearing applications is that it slowly degrades in the human body and is progressively replaced by the growing hard tissue thereby no second surgery is needed. Thus, it significantly reduces inconvenience to the patient, morbidity and health cost. On comparing the mechanical properties, magnesium is well compatible with natural bone. The density and Young´s modulus of magnesium are closer to those of natural bone (1.8-2.1 g/cm^3 and ~30 GPa). As compared to biodegradable polymers (polylactic acid) and ceramics (hydroxyapatite), magnesium has higher tensile strength and plasticity that is important for load-bearing applications like screws [22]. From the physiological point of view, magnesium is a crucial element for the human body with consumption lying in the range of 250-500 mg/day. Magnesium supports many enzymatic reactions, stabilizes DNA and RNA, and helps neurological functions and energy metabolism. Magnesium also influences cell proliferation, bone growth and strength. The adult human body contains approximately 30 gm of magnesium, concentrating mainly in muscles and

bones. The commonly used magnesium alloys in medical applications are AZ31, AJ62, WE43, etc. However, its low corrosion resistance and accumulation of large amount of hydrogen around the implant during the in vivo corrosion process, confine the widespread use of Mg-based materials as biomaterials. To overcome this issue, much research efforts focus on exploring the use of different alloying elements in Mg and surface treatments such as protective coatings on Mg-based materials [38,39].

2.6.6 Sports industry

A lot of buzz is being generated in the sports sector by Mg as it has taken the performance to a whole new level. Magnesium being stronger, light-weight, and durable, 16 times more shock absorbant than aluminum, makes it the ideal metal that gives competitive sports an extra edge. Many mountain bike and motorcycle companies have incorporated Mg in their designs for years while additional attention is being generated in the new innovations used in sports sectors. Snowboarders, skiers and ice skaters prefer their equipment made of magnesium due to the better stability at higher speeds [40].

2.7 Strengthening Mechanisms

Metals in their natural form are not suitable for any engineering applications. Due to the nature of metallic bonding and lattice defects, strengthening of metals are necessary because they are weak and the optimum properties can’t be obtained. Strengthening mechanisms are directed towards hindering the dislocation motion or strengthening the lattice against the easy movement of lattice defects. The ability of a metal to deform primarily depends on the ability of dislocations to move. Strengthening of metals include grain size reduction, solid solution strengthening, strain hardening, precipitation hardening, dispersion hardening, etc [41].

2.7.1 Grain refinement

The grain refinement strengthening mechanism is based on the fact that crystallographic orientation abruptly changes when passing from one grain to the next across the grain boundary. Therefore, if the orientation is very misaligned, it is difficult for a dislocation moving on a common slip plane in one crystal to pass over to a similar slip plane in another grain. Actually, the crystals are separated by a thin non-crystalline region, which is the characteristic structure of a large angle grain boundary. Atomic disorder at the boundary causes discontinuity in slip planes. Hence, dislocations are stopped by a grain boundary and pile up against it. The smaller the grain size, the more frequent is the pile up of dislocations [42]. A twin boundary can also act as an obstacle to dislocation motion. A grain boundary can act as a barrier for dislocation motion in two ways: (a) by forcing the dislocation to change its direction of motion and (b) discontinuity of slip plane because of disorder. The finer the grain of a metal larger is the area of grain boundaries that impedes dislocation motion. Grain size reduction also improves toughness. Methods of grain refinements used in casting process are mainly classified into three: (1) thermal method, (2) chemical method and (3) mechanical method [43,44].

2.7.2 Solid solution strengthening

Solid solution strengthening is a type of alloying that can be used to improve the strength of a pure metal. The technique works by adding atoms of one element to the crystalline lattice of another element forming a solid solution. The local non uniformity in the lattice due to the alloying element makes plastic deformation more difficult by impeding dislocation motion. In contrast, alloying beyond the solubility limit can form a second phase, leading to strengthening via other mechanisms. The strength of a material depends on how easily dislocations in its crystal lattice can be

propagated. Depending on their character, these dislocations creates stress fields within the material. When solute atoms are introduced, local stress fields are created that interact with those of the dislocations, blocking their motion and causing an increase in the yield stress of the material, which means an enhancement in strength of the material. This gain is a result of both modulus effect and the lattice distortion. When solvent and solute atoms differ in size, local stress fields are generated which can attract or repel dislocations in their vicinity. This is known as the size effect. By relieving compressive or tensile strain in the lattice, the solute size mismatch can put the dislocation in a lower energy state. In substitutional solid solutions, these stress fields are spherically symmetric, which means they have no shear stress component. As such, substitutional solute atoms do not interact with the shear stress fields characteristic of screw dislocations. In interstitial solid solutions, solute atoms cause a tetragonal distortion, creating a shear field that can interact with screw, edge, and mixed dislocations. The repulsion or attraction of the dislocation centers to the solute particles increase the stress to propagate the dislocation in any other direction. Increasing the applied stress necessary for the dislocation motion enhances the yield strength of the material [45,46].

2.7.3 Strain hardening

Work hardening, also known as strain hardening or cold working, is the strengthening of a metal by plastic deformation. This strengthening occurs because of dislocation movements and dislocation generation within the crystal structure of the material. Before work hardening, the lattice of the material shows a regular, nearly defect-free pattern (almost no dislocations). The defect-free lattice can be generated or restored any time by annealing. By work hardeneding the material, it becomes increasingly saturated with new dislocations, and new dislocations are prevented from

nucleating. This resistance to dislocation-creation manifests itself as plastic deformation resistance; hence, the observed strengthening [47].

2.7.4 Precipitation hardening and dispersion strengthening

Precipitation hardening, also called age hardening, is a heat treatment technique used to increase the yield strength of malleable materials, including most structural alloys of aluminium, magnesium, nickel, titanium, and some steels and stainless steels. In super alloys, it is known to enhance yield strength anomaly resulting in excellent high-temperature strength. Precipitation hardening relies on solid solubility change with temperature to produce fine impurity particles, which impede the dislocations movement, or defects in a crystal's lattice. Since dislocations are the dominant carriers of plasticity, this serves to harden the material. These impurities play the identical role as the particle substances in particle-reinforced composite materials. Unlike ordinary tempering, alloys must be kept at elevated temperature for hours to allow precipitation to take place. This time delay is called "aging". In dispersion strengthening, hard particles are mixed with matrix powder and consolidated and processed by powder metallurgy techniques. Here, second phase shall have very little solubility in the matrix, even at elevated temperatures. Because there is very little solubility, the particles resist growth or over-ageing to a much greater extent than the second phase particles in a precipitation hardening system. Theoretically, at least, it is possible to produce infinite number of dispersion-hardened systems by mixing finely divided metallic powders and second phase particles [48].

2.8 Corrosion

Corrosion is a process that involves deterioration or degradation of metal. When magnesium alloys are employed as an engineering material, in particular in automotive

and aeronautical industries, it is subjected to serious environments, thus their corrosion behavior is one of the main critical aspect. Magnesium has the lowest standard electrode potential (- 2.37 V) as compared to other engineering metals, this low electromotive force enables magnesium to displace hydrogen even at high pH values. But in 3.5% NaCl solutions, Mg has a standard electrode potential of -1.38 V, which indicates that the metallic surface is not in direct contact with the solution and is covered by a hydroxide layer. This natural outer layer is not dense, because its corresponding Pilling-Bedworth ratio is ≈ 0.81, which indicates that the underlying metal cannot be completely covered as a result, magnesium and its alloys are highly susceptible to corrosion.

2.8.1 Types of Corrosion

2.8.1.1 Galvanic corrosion

Dissimilar metals and alloys have different electrode potentials, and when two or more of these come into contact in an electrolyte, one metal acts as anode and the other as cathode. The electropotential difference between the dissimilar metals is the main driving force for an accelerated attack on the anode of the galvanic couple. The anode metal dissolves into the electrolyte, and the deposit collects on the cathodic metal. The more noble (higher potential) element is protected and the more active (lower potential) element corrodes at higher rate. Galvanic corrosion occurs on magnesium alloys mainly due to excessive levels of heavy metal or flux contamination, and also due to poor design and assembly practices. The metals such as Fe, Ni and Cu have low hydrogen overvoltage; they can serve as efficient cathodes, consequently causing severe galvanic corrosion. Metals such as Al, Zn, Cd and Sn that have active corrosion potential with high hydrogen over potential are less damaging. The galvanic corrosion consisting of substrate and intermetallic phase is macroscopically observed as

overall corrosion. The galvanic corrosion rate increases mainly due to high conductivity of the medium, large potential difference between anode and cathode, low polarizability of the anode and cathode, large area ratio of cathode to anode and small distance from the anode to the cathode [49].

2.8.1.2 Pitting corrosion

Pitting corrosion, or pitting, is a form of extremely localized corrosion that leads to the creation of small holes in the metal. The driving power for pitting corrosion is the depassivation of a small area, which becomes anodic while an unknown but potentially vast area becomes cathodic, leading to very localized galvanic corrosion. Magnesium is a naturally passive metal. Pitting corrosion will occur at free corrosion potential of magnesium, when exposed to chloride ions in a non-oxidizing medium. It is generally seen that corrosion pits starts at flaws adjacent to a fraction of the intermetallic phases such as $Mg_{17}Al_{l2}$ and AlMn as a result of the breakdown of passivity. This is followed by the formation of an electrolytic cell in which the intermetallic phases are the cathode type AlMn, AlMnFe, $Mg_{17}Al_{l2}$, Mg_2Cu, and the surrounding α-Mg matrix is the anode [50].

2.8.1.3 Intergranular corrosion

Intergranular corrosion (IGC), also known as intergranular attack (IGA), is a type of corrosion where the boundaries of crystallites of the material are more susceptible to corrosion than their insides. It is generally regarded that alloys with intermetallic phases or compounds cause selective attack to intergranular corrosion [51]. Recent studies show that intergranular corrosion can occur on Mg alloys. Arrabal et al. [52] have noticed that the grain boundaries for WE43 in 3.5% NaCl aqueous solution suffer preferred attack and intergranular corrosion.

2.8.1.4 Filiform corrosion

Filiform corrosion is a special type of corrosion that occurs under some thin coatings in the form of randomly distributed thread like filaments. Filiform corrosion is also known as "underfilm corrosion" or "filamentary corrosion". It is caused by active galvanic cells across the metal surface. Its head is anodic, whereas the tail is cathodic.

2.8.1.5 Crevice corrosion

Crevice corrosion refers to corrosion occurring in confined spaces to which the access of the working fluid from the environment is limited. These spaces are generally called crevices. It occurs in the metal-to-metal joint or metal-to-non-metallic material. This type of attack is usually combined with small volumes of inactive solution caused by holes, gasket surfaces, lap joints, surface deposits, and crevices under bolt and rivet heads .The major factors effect crevice corrosion are crevice type, crevice geometry, materials and environment. Ghali et al. [54] have suggested that crevice corrosion could be formed due to the hydrolysis reaction in case of Mg and Mg alloys, at least in certain conditions, where it is believed that oxygen has no severe role in the corrosion mechanism. The formation of $Mg(OH)_2$ should influence the properties of the interface between Mg and the solution in the crevice.

2.8.2 Factors Influencing the Corrosive Behavior

2.8.2.1 Metallurgical influence

2.8.2.1.1 Alloying elements

Fe, Ni and Cu are detrimental for the corrosion of magnesium alloys. The detrimental effect decreases in the following order: Ni > Fe > Cu. Fe is generally of most concern since it is introduced to the melt from steel pots and casting moulds and it is present as an impurity in the alloying elements. However, Ni is more harmful than

Fe, both in pure magnesium and in magnesium alloys, because of its lower tolerance limit. As nickel has a low solid solubility, it must be present as a separate phase, thus becoming more detrimental [50]. Corrosion resistance improves with increase in Al content. For example, the corrosion rate of AZ91, AZ61 and AZ31 in 5% NaCl solution is enhanced with the decrease of Al content. Mn can improve the corrosion resistance of Mg alloys; but this is not always the case. The corrosion rate of Mg alloys is related to Fe content and Fe/Mn ratio [50]. Rare earth improves the corrosion resistance of Mg alloys, but is affected by medium and pH value [55].

2.8.2.1.2 Microstructure and grain size

The rapid solidification process can refine the microstructure which is beneficial to the corrosion behavior. It can change the corrosion mechanism; turning pitting corrosion of Mg-A1 alloys into overall corrosion. The surface or skin layer of die-cast Mg-A1 magnesium alloys with very fine grains, high β volume fraction and continuous distribution of β phase along grain boundaries has a higher corrosion resistance than its core [56].

2.9 Wear

Wear is in the broadest sense, may be defined as “damage to a solid surface, generally involves progressive loss of a material due to the relative motion between the surfaces and a contacting substance or substances.” When two surfaces in contact slide over one another, one or both of the surfaces will suffer wear. Different wear mechanisms commonly seen in the materials are abrasion, adhesion, delamination, oxidation and plastic deformation. Wear is a complex phenomenon in which the real contact area between two solid surfaces compared with the apparent area of contact is very small, being limited to the points of contact between surface asperities. The applied load to the surfaces will be transferred through these points of contact and the

localized forces can be very large. The material intrinsic surface properties, the surface finish, temperature, speed, load, and properties of the opposing surfaces are important in determining the wear rate of a material. Wear, which can be said as the progressive loss of substance from the operating surfaces of the mechanically interacting element of a tribo-system can be measured in terms of weight loss or volume loss [57].

The wear behavior of Mg alloys is crucial concern, which has become one of the main subject of investigation during recent years because in certain applications, lightweight alloys and composites are subjected to sliding motion including automotive brakes, engine components (piston and cylinder bores). Therefore, sliding wear is also an important consideration in material processing by rolling, forging, etc. Abrasion is the prevailing wear mechanism at lower loads. Traces of parallel grooves can be distinguished on surfaces of most samples. These scratches may be attributed to hard asperities of counter face or detached particles that removed from disk or pin and placed in surface contact. With the wear process advancement, grooves become wider and deeper. Delamination mode of wear occurs when tests are conducted at sufficient high loads. Higher loads and longer sliding distances play an important role in increasing the probability of crack formation and growth. High loads at long sliding distances result in severe plastic deformation on materials. Due to intensive frictional heat of wear, the alloys locally melt and flows in the sliding direction [58].

2.9.1 Types of Wear Mechanisms

2.9.1.1 Adhesive wear

Adhesive wear can be found between surfaces during frictional contact and generally refers to unwanted displacement and attachment of wear debris and material compounds from one surface to another. When the adhesive force of the two metals exceeds the strength of either of the metal, adhesion and adhesive wear occurs. Particles

that are removed from surface of one material are either permanently or temporarily attached to the other material. When surfaces slide against each other and the pressure between the contacting asperities is sufficiently high enough to cause local plastic deformation. Hardness of a material determines the real area of contact between asperities of contacting materials [59].

2.9.1.2 Abrasion wear

Abrasive wear occurs when a hard rough surface slides across or along a softer surface. ASTM International defines it as the material loss due to hard particles or hard protuberances that are forced to move against or along a solid surface. Any material, even if the bulk of it is very soft, can cause abrasive wear if hard particles are present. Abrasive wear occurs under two conditions:

1. Two body abrasion: In this condition, one surface is harder than the other rubbing surface. Examples in mechanical operations are cutting, grinding, and machining.

2. Three body abrasion: Here a third body, usually a small particle of grit or abrasive, lodges between two softer rubbing surfaces, thereby abrading one or both of these surfaces.

2.9.1.3 Oxidation wear

The metal surface is normally covered with an oxide layer, which prevents metal-to-metal contact, and thus avoiding the formation of adhesion and thereby reducing the tendency of adhesive wear. In this way, oxide is a favourable factor in reducing wear rate of metallic materials. However, whether such positive effect can be realised or not is strongly dependent on the contact conditions and material properties. When the hardness of the metal underlying an oxide layer is low, or when the contact load is comparitively higher, the metal beneath the oxide layer will plastically deform,

and asperities in the hard surface will penetrate through the thin oxide layer, leading to the normal metal-to-metal contact. In this case, wear by abrasion or adhesion will occur depending on the chemical and mechanical properties of the contacting metals. The beneficial effect of oxide is minimal and wear rate is generally high. On the other hand, when the underlying metal is hard enough to support the oxide film, such as on a surface engineered hard surface, a process known as oxidation wear will occur [60]. During sliding, the high surface temperature generated by frictional heating, and the reduced activation energy of oxide formation caused by plastic deformation, can enhance the oxidation rate. Thus, rapid oxidation can be attained, and the oxide layer can grow thicker during sliding than under static conditions. This ensures that the fresh metal is rapidly covered with a new layer of oxide after the original oxide film is worn away. Oxidation wear is a mild form of wear.

2.9.1.4 Delamination wear

Delamination wear is an extension of the surface fatigue wear case with the surface fatigue applying over a larger surface area. Surfaces in constant contact with each other due to incorrect or inefficient lubrication will stress harden and case sub-surface deformation, which would ultimately result in cracking. Further, adhesive wear can eventually lift flat fragments from the surfaces affected [62]. Delamination wear is sometimes referred to as surface fatigue wear. It takes place in three stages:

1. Voids form near the surface.
2. Voids grow as cracks parallel to the surface.
3. Detachment of long thin wear particles when the crack reaches a critical length and breaks through to the surface.

Voids form at the location of inclusions or other imperfections in the material. Dislocations in the metal pile up at these impurities making the voids to grow. Because

metal impurities are key factor in the nucleation of these voids, materials with few inclusions will suffer less wear from delamination wear. A crack generating from a void will not initially go to the surface because it is under a tri-lateral compressive state of stress and there is plastic strain at the surface. Crack growth requires stress reversals; in this case the stress reversals are given by asperities on the surface. As an asperity slides over a surface the material facing the asperity sees alternating shear stresses. Since the crack grows parallel to the surface at a shallow depth, wear particles formed by this mode of wear will be long and thin [63,64].

2.9.1.5 Plastic deformation wear

In plastic deformation, permanent displacement or removal of material occurs in a single engagement. These processes result from the penetration of softer body by a harder body. Plastic deformation is favored when the load on the abrasive particles is small. This occurs as a result of small abrasive particles or low applied loads, when the abrasive is blunt or blunts during contact, and when the ratio of fracture toughness to hardness is high [61].

2.10 Mg Alloy Systems

2.10.1 Mg-Al System

Magnesium alloys are generally distingushed into aluminium containing and aluminium free alloys than those free from aluminium. Zr is the most effective grain refiner for non aluminium containing magnesium alloys and the Mg-Al alloys are more difficult to refine. The zirconium-free magnesium alloys include Mg-Al, Mg-Al-Zn, Mg-Al-(Rare-Earths), Mg-Al-(Alkaline Earths), Mg-Al-Si, and Mg-Li alloys that contain a number of alloying elements such as rare earths, alkaline earths, lanthanides or a combination of these. The Mg-Al, Mg-Al-Zn and Mg-Al-Si are the most common

and other alloy systems are either semi-commercial or being developed. Pure Mg has long columnar grains growing from the wall and hence the measurement of grain size is measured as the width of the columnar grains. Addition of small wt.% of Al (1 to 3 wt.%) triggers a transition to equiaxed grains and a significant reduction in grain size and this effect continues up to 5 wt.%. The grain size of Mg-9Al binary alloy is similar to AZ91. At low Al percentages (< 3 wt.%), the grain size is much higher than that found at higher Al contents and by adding 3 wt.% Al, the columnar grain growth is suppressed by about 75% and also produces much narrower columnar grains. The columnar structure is not present once the Al addition is above 5 wt.%.

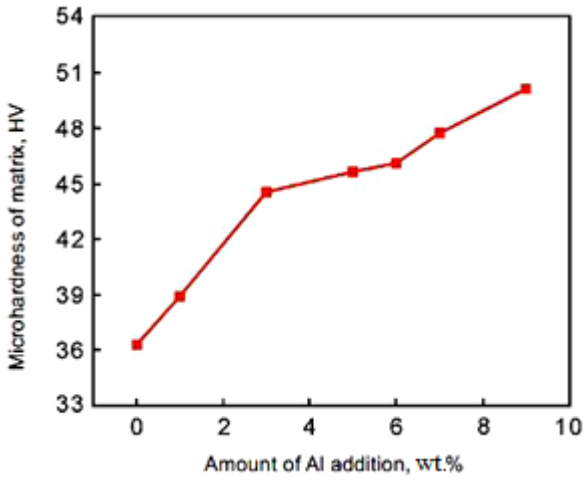

Fig. 2.4 *The effect of varying Al addition on the micro-hardness of α-Mg matrix [44].*

The effect of varying Al addition on the micro-hardness of α-Mg matrix are shown in Fig. 2.4. By the addition of 3 wt.% Al, the micro-hardness increased from 36.3 HV to 44.5 HV and further increases slowly to 50.1 HV by the addition of Al up to 9%. The increment in micro-hardness is mainly attributed to (a) solution strengthening due to Al atoms getting solubilized into the α-Mg matrix and (b) grain refinement strengthening due to the Al addition which refining the α-Mg grains and dendrite arms. Fig. 2.5 shows the microstructural changes with increasing aluminium content. A small addition of aluminium to pure magnesium leads to a morphological change of the

primary phase from a cellular to a dendritic structure. Rosette-like globular equiaxed grains form with aluminium rich solid solution between the dendrite arms. As the aluminium content is increased further to 5 wt.%, dendrites with pools of eutectic phase between the dendrite arms start to develop and, when the aluminium content is further increased, a fully developed dendritic structure with sharp tips is observed [44].

With an increase Al, the grain size of Mg-Al alloys becomes finer thereby enhancing the room temperature yield strength and ultimate tensile strength, but hinders the elevated temperature creep resistant property due to grain boundary sliding. The refinement of α-Mg grains and dendrites reduces the separation of alloying elements. An increase in $Mg_{17}Al_{12}$ phase can improve the corrosion potential thereby reducing the corrosion rate. As the percentage of Al increases, hot cracking susceptibility reduces considerably, but the amount of shrinkage cavity increases. The property trend of Mg-Al alloys by varying Al content is shown in Fig 2.6.

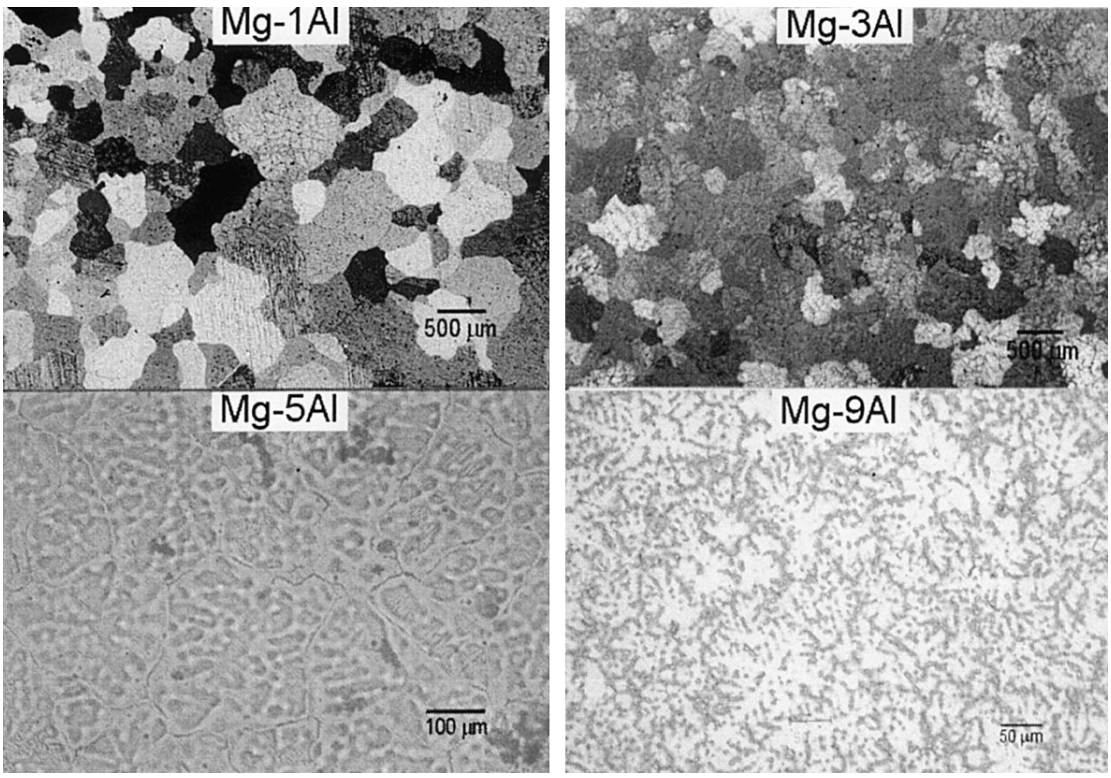

Fig. 2.5 *Microstructural changes with increasing aluminium content [44].*

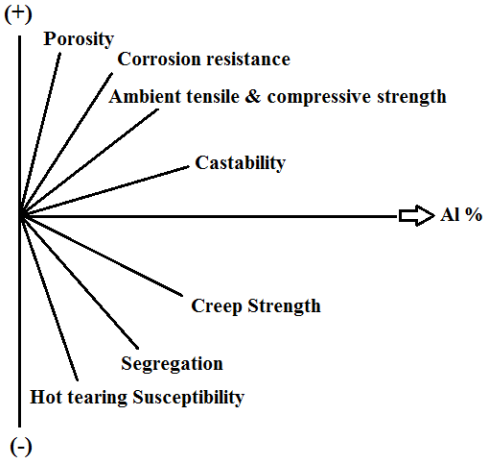

Fig. 2.6 *The property trend of Mg-Al alloys by varying Al content.*

2.10.2 Mg-Al phase diagram

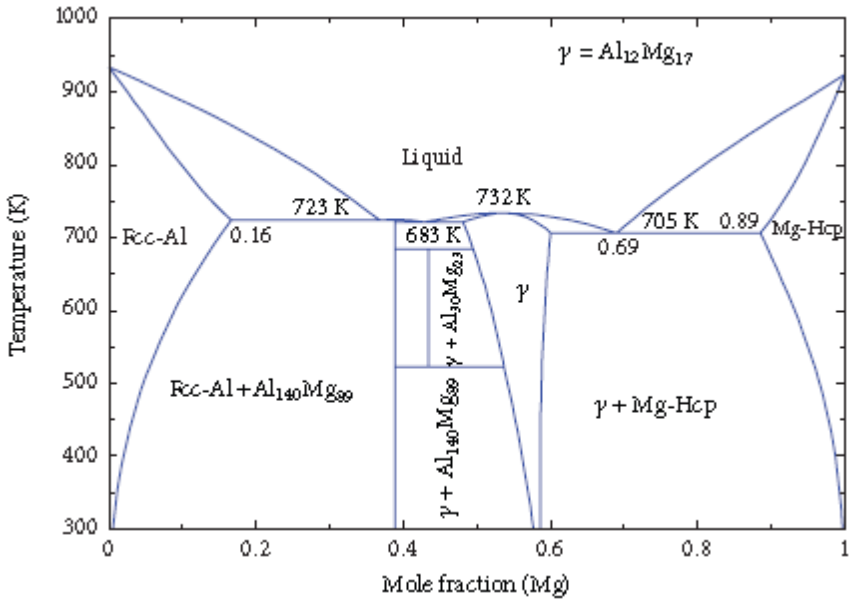

Fig. 2.7 *Mg-Al Phase diagram.*

The binary Mg-Al phase diagram is shown in Fig. 2.7. The Al solid solubility in Mg-Al system ranges from 2.1 wt.% at 25 ^{o}C to 12.7% at 437 °C (eutectic temperature). The eutectic composition consists of 33% Al and its composition is $Mg_{17}Al_{12}$. So, all the Mg-Al alloys have aluminium content less than 12.6 wt.% and that alloy solidifies with α-Mg phase. Depending on composition and cooling rate, the eutectic exhibits a wide range of morphologies in hypoeutectic Mg-Al alloys. Alloys

with aluminium content approaching the eutectic composition displays regular lamellar or eutectic microstructures [43], while those with aluminium contents less than about 10 wt.% Al exhibit eutectic morphologies that are generally referred to as fully or partially divorced. The two eutectic phases are completely separated in the microstructure in a fully divorced morphology. Each interdendritic region consists of a single β-$Mg_{17}Al_{12}$ particle surrounded by `eutectic' α-Mg, which has grown from the primary dendrites. A partially divorced eutectic morphology is characterized by `islands' of eutectic α-Mg within the β-$Mg_{17}Al_{12}$ phase, but the bulk of the α-Mg is still outside the $Mg_{17}Al_{12}$ particle, i.e. the volume fraction of α-Mg within the $Mg_{17}Al_{12}$ particle is much lower than the proportion predicted by the equilibrium phase diagram. Mg-Al alloys display a wide freezing range, and these alloys are therefore susceptible to a range of casting defects including segregation, porosity and hot tearing [44].

2.10.3 Precipitates of Mg-Al alloys

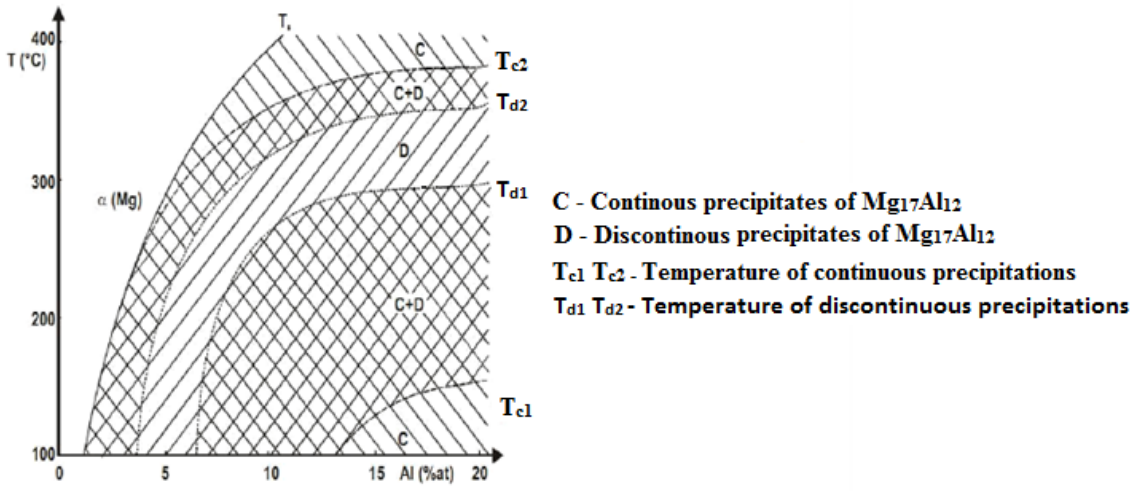

Fig 2.8 *Variation in precipitate morphology with respect to aging temperature and Al content in binary Mg-Al alloys.*

The trend of age hardening behavior of Mg-Al alloys shows rapidly increasing hardness and gradually reducing hardness. During ageing, the β-$Mg_{17}Al_{12}$ nucleates in the form of discontinuous precipitate from grain boundaries and grows into the α-

matrix. The hardness increment is not significant up to 5 wt.% Al but above 7 wt.% Al, hardness is significantly hiked and peak aged time can be clearly seen. Precipitation occurs over a wide aging temperature of 150 to 300 ^{o}C and the differences between continuous and discontinuous precipitation consists in the nucleation places and growth. Discontinuous precipitates (DP) is the cellular growth of alternating plates of secondary phase and near-equilibrium matrix phase at high angle boundaries, are detrimental to the age hardening response of Mg-Al alloy system. For Continuous precipitation (CP) the precipitates of the β phase nucleate and grow inside the matrix and are responsible for age-hardening of the Mg-Al alloys. Duly et al. [32] proposed a "morphology map" showing the in precipitate morphology variation with aging temperature and Al content in binary Mg-Al alloys as shown in Fig 2.8.

At $\mathbf{T < T_{c1}}$ temperature only continuous precipitations of phase $Mg_{17}Al_{12}$ forms.

At the temperature range of $\mathbf{T_{c1} < T < T_{d1}}$ both continuous and discontinuous precipitations of the $Mg_{17}Al_{12}$ phase occur in the alloy and as the temperature increases, the number of discontinuous precipitations increases.

For the temperature range of $\mathbf{T_{d1} < T < T_{d2}}$ only discontinuous precipitations of $Mg_{17}Al_{12}$ phase forms in the alloy.

In the temperature range of $\mathbf{T_{d2} < T < T_{c2}}$, both continuous and discontinuous precipitations of the $Mg_{17}Al_{12}$ phase occur in the alloy and with the rise in temperature, the number of discontinuous precipitations rises.

For the temperature range of $\mathbf{T_{c2} < T < T_s}$ (solubility limit temperature-solvus), only continuous precipitations $Mg_{17}Al_{12}$ phase occur in the alloy.

Critical temperature (T_{c1}) occurs mainly in alloys containing 18.8 at.% of Al. In Mg-Al alloys, at low and high temperatures, continuous precipitation prevails and for the temperatures range in between, discontinuous precipitation prevails [33].

2.10.4 Mg-Al-RE alloys

The mechanical properties of Mg-Al alloys decrease rapidly at temperatures above 100 ^{o}C. This is attributed to the fact that the magnesium alloys undergo creep deformation mainly by grain-boundary sliding. Due to the low melting point (437 ^{o}C) and poor thermal stability, β-$Mg_{17}Al_{12}$ phase gets coarsen and soften at the temperature exceeding 120 ^{o}C. Thus, the safe use of Mg-Al alloys are restricted to 120 ^{o}C and beyond this temperature considerable loss in strength occurs. Hence, to increase the mechanical performances of the Mg-Al alloys, it is necessary to modify the distribution and morphology of β-$Mg_{17}Al_{12}$ phase. Some methods used to enhance the mechanical properties of alloys are solid solution strengthening, precipitation hardening, particles strengthening by dispersing fine second phases and grain refining. One of the effective ways to improve the mechanical properties is by slightly modifying the alloy composition through various elemental additions like RE rather than developing a new alloy.

The RE additions effectively enhance the mechanical properties of the Mg alloys. Firstly, the solid solution hardening caused by RE addition contributes to the improvement of the strength. The solid solubility increases gradually from the light to heavy rare earth elements. This may be related to the progressive decrease of the rare earth metallic radius, which becomes nearer to that of Mg. The solubility of heavy rare earths is relatively high, so it can result in solid solution hardening. Solid solution strengthening by Gd and Y are much larger than that of Zn and Al. In addition to the size and/or modulus misfits between solute and solvent atoms, the valency effect is suggested to be possibly responsible [37]. It was suggested that the bond energy between Mg and Y is much stronger than that between Mg and Al. Secondly, the precipitation hardening introduced by RE addition also contributes to the strength improvement. Yttrium, cerium, lanthanum, gadolinium and neodymium are mainly used as rare earth elements for alloying. Studies regarding other REs in Mg-Al alloy are

very less. Microstructure of Mg-Al alloys consist of α-Mg and $Mg_{17}Al_{12}$. With the addition of almost all rare earths, microstructure is refined, amount of $Mg_{17}Al_{12}$ is decreased and new Al_2RE or $Al_{11}RE_3$/Al_4RE phases are formed irrespective of the RE. $Al_{11}RE_3$ and Al_4RE have almost same composition.

The maximum solubility of yttrium in solid Mg is about 11% at 567 °C [65] and about 7 wt.% at room temperature [66]. With the addition of Y, the microstructure is refined and the amount of $Mg_{17}Al_{12}$ phase is decreased. Only Al_2Y is formed as a new phase with the addition of Y and the Al_2Y phase increases with the increasing of Y [67,68]. The main reason for the grain refinement is the formation of fine Al_2Y dispersoid [69]. Al_2Y is formed during casting because melting point of Al_2Y is 1485 °C which is higher than eutectic reaction temperature. So, nucleation takes place at the sold-liquid interface and the solute atoms restrict the grain growth of primary and eutectic phase. So, the as-cast microstructure can be refined by the Y addition [55,66,70,71]. No Mg-Y compounds are formed, because the electronegativity difference between Mg and Y is less compare to Al and Y [20]. The reason decreasing $Mg_{17}Al_{12}$ phase is because Y consumes some of the Al by forming the Al_2Y intermetallic compound, leaving less Al to combine with the Mg matrix to form $Mg_{17}Al_{12}$. After solution treatment at sufficient temperature and time, the $Mg_{17}Al_{12}$ phase dissolved in the matrix and only Al_2Y distributed in the α-Mg matrix. Because Al_2Y phase has high melting point and thermally stable [20]. Sunghak Lee *et al.* [69] studied the aging of squeeze cast AZ91 alloy with 1% Y. The hardness of AZ91 alloy decreased when aged for 60 hours, because it passed the peak hardness. Whereas, the hardness of the AZ91-1Y alloy increase somewhat more than in the case of the 30-hour aging. It shows that the aging time required for reaching the peak hardness increases with the addition of Y, the Al_2Y dispersoid being stable at high temperatures. The wear

resistance of the Mg-3Al alloy increases with the addition of Y due to the formation of Al_2Y phase. The higher thermal stability of Al_2Y phase is also improved the wear resistance of the Y added alloy [58]. The corrosion resistance and corrosion evolution of as-cast AZ91 alloy with rare earth Y addition were investigated and the results show that the proper amount of Y in the alloys can improve the corrosion resistance of AZ91 alloys effectively. With the increase of Y content, the corrosion rate of the modified AZ91 alloys by Y addition was markedly less than that of AZ91 alloy. The corrosion rate of AZ91 alloy with 0.3 wt.% Y was the slightest, but further addition of Y content over 0.3 wt.% attributed to increased corrosion [73,74].

Solid solubility of Ce in Mg-matrix solid solution is low, almost negligible solubility at room temperature [75,76]. Mainly $Al_{11}Ce_3$ phase is formed with the addition of Ce, which increases with the increasing of Ce and the $Mg_{17}Al_{12}$ phase is decreased [75]. $Mg_{17}Al_{12}$ phase in AM50 and AM60 alloys distributes in bulk as well as lamellar like structure, but the distribution is dispersive and along grain boundaries as a network in Ce containing alloy. Grain refinement is taking place with the addition of Ce. Because $Al_{11}Ce_3$ appears between the $Mg_{17}Al_{12}$ phases, giving an obstruction to the growth of $Mg_{17}Al_{12}$, breaking up its networked structure. No MnAl intermetallics are found because of a small content of Mn [75]. $Mg_{17}Al_{l2}$ disappears completely with increase of Ce to 3% and 5% in Mg-7Al and Mg-5Al respectively and Al_2Ce intermetallic phase is formed along with $Al_{11}Ce_3$, where $Al_{11}Ce_3$ phase is the dominant secondary phase. $Al_{11}Ce_3$ has a body-centered orthorhombic structure and Al_2Ce has a face-centered cubic structure [77]. Guo Feng et al. [78] conducted heat treatment study on AZ91 alloy containing 0-1% Ce. During solution treatment at 420 ºC, the $Mg_{17}Al_{12}$ phase gradually decreases with the holding time increases, but the time of entire $Mg_{17}Al_{12}$ phase decomposition in both alloys is different. The decomposition of

$Mg_{17}Al_{12}$phase in AZ91 alloy is completed within 12 h. Ce added in AZ91alloy can retard the decomposition of $Mg_{17}Al_{12}$ phase during solution. If the Ce content is more, decomposition time becomes longer. It needs about 20 h for the alloy with 0.8% Ce to finish solid solution. Single solution is achieved by the decomposition of $Mg_{17}Al_{12}$ phase and diffusion as well as homogenization of Al atoms. The Ce in $Mg_{17}Al_{12}$ enhances the chemical stability of $Mg_{17}Al_{12}$ and inhibits decomposition of $Mg_{17}Al_{12}$ during solution. Similarly, the homogenization rate of Al atoms also decreases due to stronger affinity of Ce that tie the diffusion of Al atom. Alloys are aged at 175 ºC for different hours after the solution treatment at 420 ºC for 20 h. During aging $Mg_{17}Al_{12}$ phase precipitates on the grain boundary then grows towards the inside grain and composes lamellar structure mixtures with α-Mg phase. If the aging time increases, $Mg_{17}Al_{12}$ phase precipitates constantly and the amount of lamellar structure mixtures increases. For AZ91 alloy, when aging for 18 h, the microstructure is almost made of all lamellar structure mixtures, but some bulk $Mg_{17}Al_{12}$ phases would appear in the microstructure if extending the aging time. For Ce containing AZ91 alloy, Ce retard the precipitation and growth of $Mg_{17}Al_{12}$ phase during aging. Because, Al_4Ce phases distribute in the matrix of AZ91alloy which obstruct the growth of $Mg_{17}Al_{12}$ phases, resulting in the $Mg_{17}Al_{12}$ phases that had too round Al_4Ce phase. Maximum hardness of the alloys is at 18 hrs due to the entire lamellar structure mixture in the microstructure for this aging time. Higher Ce content declines the hardness because Ce inhibits the precipitation and growth of $Mg_{17}Al_{12}$ phase and the amount of lamellar structure mixture in microstructure is less. After 18 h, the hardness of AZ91 alloy decreases, because of the transformation from lamellar $Mg_{17}Al_{12}$ phase to blocky one happens. However, after the peak aging, decrease degree of hardness of higher Ce containing

alloy is relatively little. Because, the $Mg_{17}Al_{12}$ phase precipitates even after peak aging, which may bring on further increase in hardness [78].

Lanthanum has very low solid solubility in Mg. Mg-La alloys do not undergo age hardening because of the poor solid solubility of La in Mg [79]. The microstructure of Mg-Al consists of α-Mg and $Mg_{17}Al_{12}$ particles. With the addition of La, grain refinement is taking place and $Al_{11}La_3$ or Al_4La are observed in the microstructure but Al_2La phase is not present in this alloy [80]. The solid solubility of La in magnesium is relatively small, rapid enrichment of solute in the liquid ahead of the growing interface would be expected during solidification which restrict the growth hence grain refinement is taking place [81,82]. The $Mg_{17}Al_{12}$ phase is not observed in Mg-4Al alloy when La is greater than or equal to 1.5% [80-82]. While adding La MM also, $Al_{11}RE_3$ Phase is formed which are thermally stable barriers opposing grain coarsening during high temperature annealing [81]. While comparing the decomposition energy of $Al_{11}La_3$, $Al_{11}Ce_3$, $Al_{11}Pr_3$ and $Al_{11}Nd_3$ according to the reaction $Al_{11}RE_3 \rightarrow 3Al_2RE+5Al$, the decomposition energy of $Al_{11}La_3$ is the highest compare to other $Al_{11}RE_3$. Therefore, the stability of $Al_{11}La_3$ is the highest among other Al-RE intermetallic compounds [83]. The hardness of Mg-Al alloy increases with La addition and is due to the microstructure refinement results from the nucleation of $Al_{11}La_3$ phases [82]. After 24 h annealing, the dissolution of the $Mg_{17}Al_{12}$ particle take place, which cause the decrease of hardness in AZ91 alloy. But, No much change in hardness of AZ91+2La MM alloy. Because after annealing, undissolved $Al_{11}La_3$ intermetallic particles are present [84].

The amount of $Mg_{17}Al_{12}$ is decreased and grains are refined with the addition of Nd [85,86]. Al_3Nd and $Al_{11}Nd_3$ are formed with the addition of 1 to 1.5% Nd and the presence of Al_2Nd particles with the addition of 1.5% in AZ91 alloy [87]. The main

reason for the grain refinement is the formation of fine Al_2Nd dispersoid, which is formed during casting and hinder the grain growth [85]. The grain size is about 62 µm. After 0.5% Nd was added, the grain size decreases to about 46 µm. when the Nd content reaches to 1%, the grain size is about 27 µm [86]. After the heat treatment under T6 condition (solution treatment at 410 °C for 10 hours and aging at 170 °C for 30 hours) of squeeze cast AZ91 + 0.5Nd alloy, the discontinuous $Mg_{17}Al_{12}$phases are precipitated on grain boundaries in a coarse nodule shape. AZ91 and AZ91-0.5Nd alloys have almost similar hardness in the cast condition. After aging, however, the AZ91-Nd alloy show high hardness compared to the AZ91 alloy. When aged for 60 hours, the hardness of the AZ91 alloy decreases, as it has already passed the peak hardness, whereas the hardness of the AZ91-Nd alloy increase somewhat more than in the case of the 30-hour aging. It shows that the aging time required for reaching the peak hardness increases with the addition of Nd. Because the Al_2Nd dispersoid is stable at high temperatures [85].

Gadolinium has high solubility in Mg, at eutectic temperature the solubility is 23.49 wt.%. Therefore, Gd provide solid solution strengthening [6]. Microstructure of Mg-Al-Gd alloy consist of many other phases with varying the amount of Al and Gd [88,89]. Two kinds of secondary phases are present in the Gd containing AZ21 alloy. One is the $(Mg,Al)_3Gd$ phase with a lamellar morphology, which is the main intermetallic located within the interdendritic interstices. The other is a few of particles with angular morphology Al_2Gd phase, which are distributed within the matrix. The formation of the $Mg_{17}Al_{l2}$ phase was suppressed by the addition of Gd. The microstructure of each as-cast alloys is very similar except the volume fraction of the main secondary phase. The volume fractions of the intermetallic phases increases with an increase in the Gd content. The volume fractions of the $(Mg,Al)_3Gd$ phases in the

4% Gd containing alloy are probably twice as many as that in the 1% Gd containing alloy [88]. With addition of 1% Gd in AM50 alloy, grains are refined, $Mg_{17}Al_{12}$ phase decreases and small granular Al_2Gd_3 & $Al_{0.4}GdMn_{1.6}$ phases are present at the grain boundary. Gd improves the nucleation rate and leads to grain refinement and grain boundary strengthening the alloy. Al_2Gd_3 phase has high melting point which separates out first in front of solidification interface and inhibits $Mg_{17}Al_{12}$ phase separating [89]. H Yokobayashi et al. [90] observed Mg_5Gd phase in Mg-3.5at.%Al-5at.%Gd alloy. Similarly, Fumin Lu et al. [8] observed Mg_5Gd along grain boundaries and polygonal Al_2Gd phases locating at grain boundary intersection. A considerable part of Mg_5Gd dissolve after at 565 °C for 24 h, but Al_2Gd remain same. Yield strength increases with the amount of Gd at both room temperature and high temperature. Ultimate strength also increases with Gd at high temperature. The improvement of tensile strength is due to the grain refinement strengthening and grain boundary strengthening of Gd [88,89]. The strength is decreasing after reaching a maximum value for 3% Gd at room temperature. The branched $(Mg, Al)_3Gd$ phase is the main strengthening phase in the as-cast AZ21-xGd alloys. Because, coarsening of the phase take place after 3% Gd. The elongation decreases with the increasing of Gd, which is due to the increasing volume fraction of $(Mg, Al)_3Gd$ [88]. Creep result of the AZ21-xGd alloys carried out at 50 MPa and 200 °C for 100 h indicate that these alloys have excellent creep resistance performance and minimum creep rate decreases with an increase in Gd content. Minimum creep rate of AZ21-2Gd alloy is 11.3×10^{-8} s^{-1}, while that for AZ21-4Gd is 2.6×10^{-8} s^{-1}. The addition of Gd to the Mg-2Al-1Zn alloys could suppress the formation of the $Mg_{17}Al_{12}$ phase and the $(Mg,Al)_3Gd$ phase is so stable that it does not decompose even after the test creep. These are the main reasons for the improvement in the creep resistance. In addition, the glide of the non-basal dislocation controls the creep

behaviors of the alloys in our investigation. The $(Mg,Al)_3Gd$ phase can effectively impede the dislocation motion [88]. Microstructural evolution of Mg91.5Al3.5Gd5 (at.%) alloy during heat treatment and its corrosion behavior in 1 wt.% NaCl solution were investigated by morphological observation, hydrogen evolution and electrochemical measurements. The microstructure of the as-cast alloy mainly consists of α-Mg, network-like Mg_5Gd and polygonal Al_2Gd phases, while a considerable part of Mg_5Gd ones dissolve after T4 treatment. After T6 treatment, profuse micro-sized needle-like precipitates including crossed Mg_5Gd-type and parallel $Mg_{12}ZnY$-type ones appear and occupy different grains. These precipitates, resulting in homogeneous corrosion, continuous and compact oxidation film on the surface, have significantly improved the corrosion resistance of the Mg alloy [8]. In order to improve the corrosion and mechanical properties of AM50 magnesium alloy, 1 wt.% Gd was used to modify the AM50 magnesium alloy. it was observed that β-$Mg_{17}Al_{12}$ phase decreased and Al_2Gd_3 and $Al_{0.4}GdMn_{1.6}$ phase existed after Gd addition. Because of the Gd addition, the grain of AM50 magnesium alloy was refined significantly, which improved the tensile strength of AM50 magnesium alloy. The decreasing of β phase improved the corrosion resistance of the magnesium alloy. The fracture mechanism of the Gd modified AM50 magnesium alloy was quasi-cleavage fracture. The corrosion residual strength (CRS) of AM50 magnesium alloy was improved after 1 wt.% Gd addition [89].

Zhang et al. [91] developed Mg-Ca alloys with 2 wt.%, 3 wt.%, 5 wt.% Al content and extruded at 400 °C with the ratio of 16:1. The microstructures and mechanical properties of the alloys were seen to be influenced by Ca/Al ratio. Results showed that the category and amount of precipitated secondary phase were influenced obviously by Ca/Al ratio, which changed from Mg_2Ca and $(Mg, Al)_2Ca$ to Al_2Ca as the

Ca/Al ratio decreased from 1 to 0.4. Even though the secondary phase was cracked after the application of hot extrusion, the amount, size and distribution of secondary phase were strongly dependent on Ca/Al ratio. All the UTS, elongation and strain hardening rate of the as-extruded alloys increased with decreasing Ca/Al ratio, however, the YS exhibited the inverse variation tendency. Jiang et al. investigated the microstructure and mechanical properties of Mg-Al-Ca alloys containing different contents (1, 2, 4 and 6 wt.%) of the Al_2Ca phase have been investigated. The results show that the Al_2Ca phase formed along the interdendritic regions in as-cast alloys. As the content of the Al_2Ca phase is 4 wt.%, the finest microstructure of the as-cast Mg-Al-Ca alloy is observed. After hot extrusion, the extruded Mg-2.32Al-1.7Ca (Mg-4Al2Ca) alloy exhibits superior mechanical properties with the UTS of 324 MPa, the YS of 275 MPa and the elongation of 10.2%. This is mainly due to the combined effects of fine dynamically recrystallized grains, nano-scale plate-like Al_2Ca precipitation and high density of submicron Al_2Ca particles dispersion in the α-Mg matrix [92]. A study by Xiao et al. [93] on the microstructure, mechanical and creep properties of Mg-3.7Al-3.8Ca (AC4a), Mg-4.4Al-4.5Ca (AC4b) and Mg-4.9Al-5Ca (AC5) alloys. Direct water-cooling semi-continuous ingots were subject to hot extrusion at 400 °C with the extrusion ratio of 16:1. After being extruding, these Mg-Al-Ca alloys consisted of α-Mg (solid solution) and Al_2Ca. Such alloys showed high strength at elevated temperatures. The ultimate tensile strength of as-extruded AC4b at 175 °C and 250 °C are 200 MPa and 112 MPa, respectively. The strain rate sensitivity exponent, m, estimated from the slope of the stress-strain curve, was around 0.11 to 0.14, implying that climb controlled dislocation creep could be a dominant deformation process of AC4a, AC4b and AC5. During the creep test, the creep properties of as-extruded AC5 is better than that of as-extruded AC4a and AC4b, the total elongation of as-extruded AC5 is 0.97% under 60

MPa at 175 °C after 100 h and the total elongation increased to 1.3% under 70 MPa at 175 °C after 100 h. The stress exponent (n) value of as-extruded AC5 is 6.67, which implies that the dislocation climb is the dominant creep mechanism in the creep test at 175 °C.

2.10.2 Mg-Zn System

Among the Mg alloy systems, Mg-Zn alloys show a good combination of mechanical properties and corrosion behavior [9,10]. Zn is known to increase age hardening response as it produces intermetallic compounds and refines the grain size. A small amount of Zn contributes to overall strength due to solid solution and precipitation strengthening [11,94,95]. Using zinc the designer can save process costs, can reach a better precision, can have better corrosion resistance; in addiction zinc has a superior tensile strength and elongation and reach a superior formability. Some recent studies discussed the mechanical property and corrosion behavior of binary Mg-Zn alloys. Zheng et al. [96] studied the binary Mg-1Zn alloy and reported its enhanced mechanical properties and corrosion resistance by addition of Zn. A binary Mg-6Zn alloy revealed suitable tensile strength and elongation for implant application, as well as a reduced in vitro degradation rate and good in vivo biocompatibility [96,97]. Also, the findings of Mg-3Zn alloy by different heat treatments showed that solution treatment enhanced corrosion resistance while aging treatment decreased the corrosion resistance. A study by Boehlert et al. [98] on Mg-Zn alloys containing 0-4.4 wt.% Zn suggests that Zn was a potent grain refiner and strengthener for Mg, where the optimal Zn content is 4 wt.%. All these aforementioned studies showed the enhanced corrosion resistance and mechanical property of magnesium by the incorporation of zinc in magnesium and great potential of binary Mg-Zn alloys in biomedical applications. However, there is a lack of details on the influence of volume fraction and existence

format of secondary phases. Besides there were disagreements over the optimal Zn addition, which was either low (1 wt.%) or high (6 wt.%).

Pure Mg material exhibits a grain size of 350 μm as shown in Fig. 2.9(a), while the average grain sizes in Mg-1Zn, Mg-5Zn and Mg-7Zn are about 100 μm, 55 μm and 56 μm as seen in Fig. 2.9(b)-(d), respectively, indicating the addition of Zn element upto 5% of weight toMg can significantly refine the grain size, but the refinement efficiency is not significant with further addition of Zn over 7 wt.%. When the Zn content increased from 5 to 7 wt.%, the second phase formed a network structure of dentrite along the grain boundary, as shown in Fig. 2.9(d). Microstructure observation showed that the addition of Zn element significantly refined the grain size of as-cast Mg-Zn alloys and increased the volume percent intermetallic in the microstructure [99].

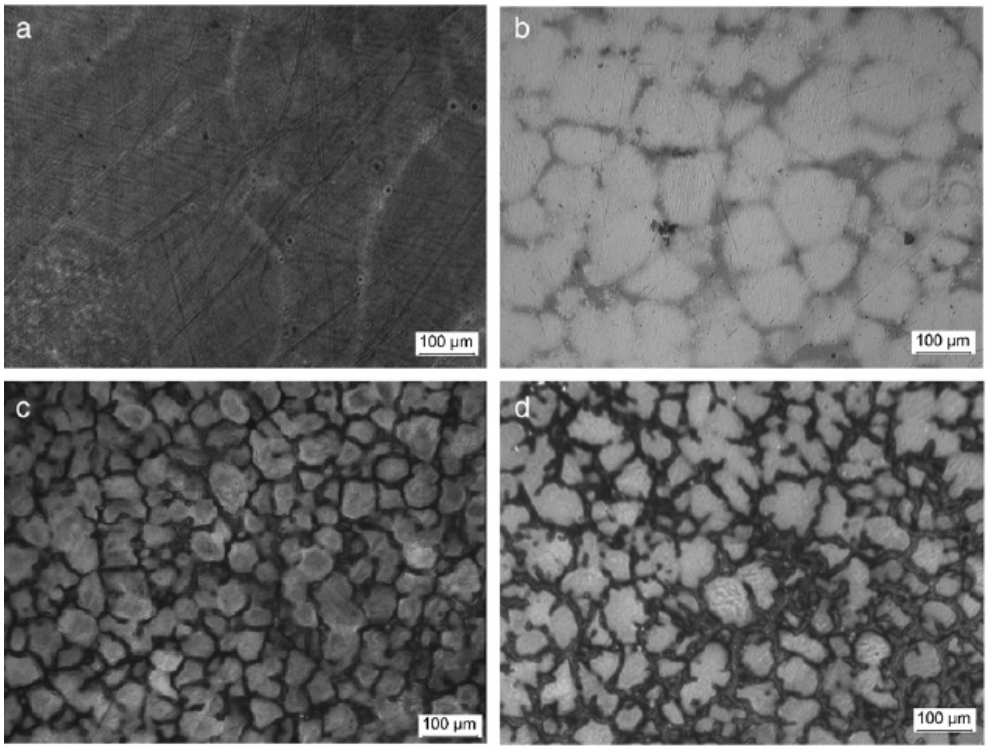

Fig. 2.9 *Average grain sizes in Mg, Mg-1Zn, Mg-5Zn and Mg-7Zn [99].*

The deleterious effects of metallic impurities like Fe and Ni can be reduced by the addition of Zn [12,13]. Some recent studies discussed the mechanical property and corrosion behavior of binary Mg-Zn alloys. Zhang et al. [12] studied the binary Mg-

1Zn alloy and reported its enhanced mechanical properties and corrosion resistance by addition of Zn as an alloying element.A binary Mg-6Zn alloy revealed suitable tensile strength and elongation for implant application, as well as a reduced in vitro degradation rate and good in vivo biocompatibility [96,97]. Also, the findings of Mg-3Zn alloy by different heat treatments showed that solution treatment enhanced corrosion resistance while aging treatment decreased the corrosion resistance [100].

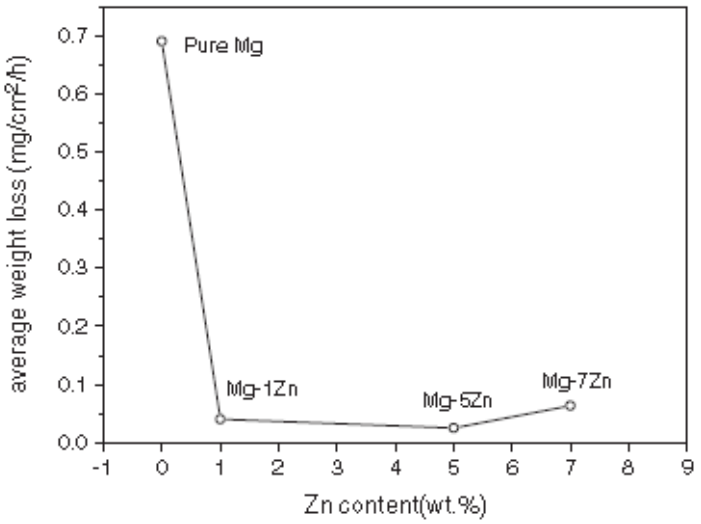

Fig. 2.10 *Average weight loss after corrosion test in Mg-Zn [12].*

A study by Boehlert [98] on Mg-Zn alloys containing 0-4.4 wt.% Zn suggests that Zn was a potent grain refiner and strengthener for Mg, where the optimal Zn content is 4 wt.%. All these studies showed the enhanced corrosion resistance and mechanical property of magnesium by the incorporation of zinc in magnesium and great potential of binary Mg-Zn alloys. However, there is a lack of details onthe influence of volume fraction and existence format of secondary phases. Besides there were disagreements over the optimal Zn addition, which was either low (1 wt.%) or high (6 wt.%).There is a high demand to design magnesium alloys with controllable corrosion rates and suitable mechanical properties. Taking this into consideration, Cai et al. [12] performed microstructure, mechanical property and corrosion tests on Mg-x

wt.% Zn alloys (x = 1, 5, 7) alloys . It was observed that Mg-5Zn alloy showed the lowest anodic current and noblest corrosion potential followed by a simultaneous increase of the breakdown potential, indicative of the best corrosion resistance among the three alloys. As confirmed in the microstructure characterization, both Mg-5Zn and Mg-7Zn alloys are mainly composed of primary Mg matrix phase with similar grain size and second phase distributed along grain boundary with the same chemical composition of MgZn intermetallic. Fig. 2.10 depicts the average weight loss after corrosion test in Mg-Zn.

2.10.2.1 Mg-Zn phase diagram

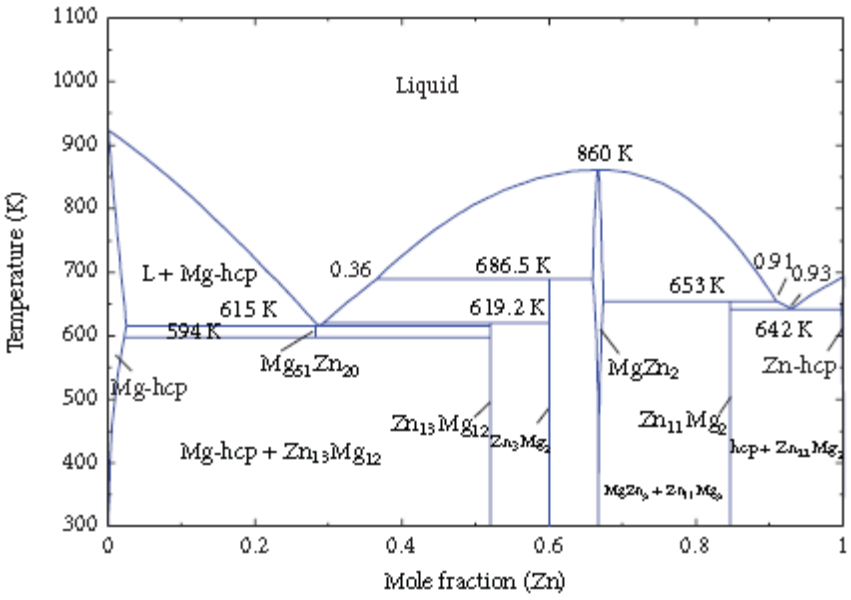

Fig. 2.11 *Binary Mg-Zn phase diagram*

Zn is commonly alloyed with Mg in AZ, EZ, ZK and in smaller amounts in AM and AE series alloys. Fig. 2.11 shows the binary Mg-Zn phase diagram. The eutectic temperature of Mg-Zn system at Mg rich side is about 341 °C, and the maximum solid solubility of Zn in Mg is 6.2 wt.% at the eutectic temperature. There are five intermetallic phases formed in the system, namely Mg_7Zn_3 (also known as $Mg_{51}Zn_{20}$), MgZn, Mg_2Zn_3 (also known as Mg_4Zn_7), $MgZn_2$ and Mg_2Zn_{11}. The liquidus in the Mg-

Zn phase diagram was determined by Boudouard [101] using thermal analysis and he introduced the Mg_4Zn phase. Grube [102] corrected Boudouard's discovery that Mg_4Zn phase did not exist and that the error was due to contaminations. Moreover, he found the intermetallic compound, $MgZn_2$ that melts at 868 K. The compound forms a eutectic with pure Zn at 97 at.% Zn and 641 K. No solid solution areas were found in the system [101,102]. Chadwick [103] found a new solid solution β near the composition $MgZn_5$ and reported that $MgZn_2$ forms a wide range of solid solution. However, his results showed increased content of zinc due to the presence of Si impurity. He also measured the liquidus line in the Mg-Zn phase diagram using thermal analysis and the reported values agree with the liquidus suggested by Grube [102].

The compound $MgZn_5$ was first discovered by Chadwick [103] and later replaced by Mg_2Zn_{11} by Samson [104]. On the other hand, Park and Wyman [105] reported the maximum solubility of Zn in Mg as 2.5 at.% Zn at 340 °C; also, they measured the narrow homogeneity range of $MgZn_2$ as 1.1 at.% Zn (from 66 at.% Zn at 416 °C to 67.1 at.% Zn at 654 K). Hume-Rothery [106] studied the system in the composition range of 30 to 100 at.% Zn using thermal analysis and microscopic inspection. Accordingly, the maximum limited solubility of Mg in Zn was determined as 0.3 at.% at 673 K. Laves [107] identified Mg_2Zn_3 phase by means of XRD and metallography inspection; he also proved that the phase is at equilibrium with Mg terminal solid solution at room temperature. The phase equilibria of Mg-Zn system from 0 to 67.8 at.% Zn were analyzed by Clark and Rhins [108] using XRD and microscopic analysis and confirmed the thermal stability range of MgZn from 366 to 608 K. They also identified the temperature of the eutectoidal decomposition, $Mg_7Zn_3 \rightleftharpoons \alpha\text{-}Mg + MgZn$ at near 598 K. After careful crystal structure study, Higashi et al.[109] replaced the compound Mg_7Zn_3 by $Mg_{51}Zn_{20}$ using XRD techniques. Afterwards, the

Mg-Zn system was assessed by Clark et al. [103] based on the experimental work of [110-114]. Using computational thermodynamics, Liang et al. [111] performed phase diagram calculations on the Mg-Zn system. Five intermetallic compounds $Mg_{51}Zn_2$ $Mg_{12}Zn_{13}$, Mg_2Zn_3, $MgZn_2$, and Mg_2Zn_{11} and two terminal solid solutions were reported in their models.

2.10.2.2 Precipitates of Mg-Zn system

The magnesium-rich side of the Mg-Zn binary phase diagram is much more complex than that of the Mg-Al binary phase diagram. The eutectic temperature is 340 ºC, and the maximum solid solubility of Zn in magnesium is 6.2 wt.% at the eutectic temperature [112]. The eutectic reaction is that the liquid phase solidifies into a mixture of α-Mg and Mg_7Zn_3 phases. The Mg_7Zn_3 phase has an orthorhombic structure, and it is thermodynamically stable only at temperatures above 325 ºC. At temperatures at and below 325 ºC, the Mg_7Zn_3 phase decomposes into α-Mg and MgZn via an eutectoid reaction. The intermetallic phase that is in equilibrium with a-Mg at temperatures below 325 ºC is a base-centered monoclinic MgZn [113]. During heat treatment of Mg-8Zn alloy at temperatures below 325 ºC, it was observed that the primary intermetallic particles of the Mg_7Zn_3 phase that had formed during the solidification process decompose into a divorced lamellar structure of α-Mg and Mg_4Zn_7. The base-centered monoclinic Mg_4Zn_7 phase is metastable, and it gradually replaced by the equilibrium phase MgZn after prolonged heat treatment. The equilibrium solid solubility of Zn in magnesium decreases with temperature, and the controlled decomposition of the supersaturated solid solution of Zn in magnesium can produce age-hardening effect [110-117]. Depending on the alloy composition and aging temperatures, it is commonly accepted in the literature [118] that the decomposition of the supersaturated solid-solution matrix phase reportedly involves the formation of G.P. zones, b01 ($MgZn_2$),

b02 ($MgZn_2$), and b (Mg_2Zn_3). A recent electron microscopy study of precipitate phases in a Mg-8 wt.% Zn alloy aged at 200 ºC [113] indicates that the precipitate structures and orientation relationships are more complicated than those reported in early studies it was reported that the b01 rods contain a mixture of Mg_4Zn_7 and $MgZn_2$ phases. Some domains of a face centered cubic structure (C15) were also proposed to exist inside the b01 rods. A small fraction of the b01 phase was also found [113] to adopt a rarely reported blocky shape and a different orientation relationship with the α-Mg phase. The recent studies have confirmed that the b02 phase has the $MgZn_2$ structure Surprisingly, the structure and composition of the equilibrium β phase have been accepted as those of the Mg_2Zn_3 phase, i.e., the triclinic and the Mg_2Zn_3 composition, even though the alloy composition lies in the (α-Mg + MgZn) two-phase field. Based on the Mg-Zn binary phase diagram and a more recent electron microscopy study, it seems more appropriate to suggest that the equilibrium β phase has a MgZn composition and a base-centered monoclinic structure. Although some information has been gained in recent years with the help of advanced characterization facilities on the structure and morphology of precipitates in Mg-Zn based alloys, there still is lack of reports in the literature that describe the details of the full precipitation process and provide some insightful understanding of the nucleation and growth behaviors of the precipitate phases in this group of alloys.

2.10.2.2.1 Mg-Zn-RE alloys

The RE additions change effectively the mechanical properties of the Mg alloys. Firstly, the solid solution hardening caused by RE addition contributes to the improvement of the strength. The solid solubility increases gradually from the light to heavy rare earth elements. This may be related to the progressive decrease of the rare earth metallic radius, which becomes nearer to that of Mg. The solubility of heavy rare

earths is relatively high, so it can result in solid solution hardening. Solid solution strengthening by Gd or Y is much larger than that of Zn and Al. In addition to the size and/or modulus misfits between solute and solvent atoms, the valency effect is suggested to be possibly responsible [119]. Secondly, the precipitation hardening introduced by RE addition also contributes to the strength improvement. The solubility drops intensely as the temperature drops. This enables remarkable precipitation hardening during the decomposition of the supersaturated solid solution. During the aging process, intermetallics with high melting point and thermal stability form and improve the strength. With RE additions, an important alloy system has been developed: Mg-Zn-RE alloys. This alloy system has been heavily studied due to the presence of peculiar secondary phases, e.g. icosahedral quasicrystalline phase (I-phase) and long period stacking ordered (LPSO) phase, which result in excellent mechanical performance at room and elevated temperatures. The LPSO phase has a long period ordered stacking sequence in the c direction of Mg and segregated Zn and Y was found in certain stacking layers [14,15].

The Mg-Zn-RE alloys has been heavily studied due to the presence of peculiar secondary phases, e.g. icosahedral quasicrystalline phase (I-phase) and long period stacking ordered (LPSO) phase, which result in excellent mechanical performance at room and elevated temperatures. The key microstructures of these Mg-Zn-RE alloys are a novel type of long-period structure phases, which are believed to play a crucial role to realize the superior mechanical properties. The novel structures are long-period chemical-ordered as well as stacking-ordered; a unique long-period stacking/order (LPSO) structure (this wording follows the sense that, in metallurgy, the “order” specifically means a chemical order, which is generally termed for configurational ordering of different atom species on the fixed atomic sites). Studies [120-122] have shown that in Mg-Zn-Y ternary alloys, the Zn to Y ratio plays a key role in the stability of secondary phase. With increasing Zn/Y ratio, the following precipitates forms in a

sequence, $Mg_{24}Y_5 \rightarrow LPSO \rightarrow W \rightarrow I\text{-}phase$ [121,122]. However, it is difficult to determine the boundary values of the Zn/Y ratio for formation of secondary phases in the as-cast condition. Wang et al. [56] reported that W-phase and LPSO phase co-exist when the Zn/Y ratio is 1.23, but the LPSO phase disappears when the ratio is greater than 1.9. Lee et al. [121] reported that I-phase and W-phase are the secondary phases when the Zn/Y ratio is between 1.8 and 6 in Mg-Zn-Y alloys. When two or more secondary phases co-exist, the alloying elements distributions are very important because they will affect the types and the area fractions of the secondary phases. A systematic study of the Zn and Y distributions in the secondary phases and Mg matrix has not been carried out in as-cast Mg-Zn-Y alloys, and how the alloying elements affect the secondary phases is unclear. Although the RE elements are quite similar, they have different roles in forming LPSO phase. For example, LPSO forms in as-cast Mg97Zn1Y2, but not in as-cast Mg97Zn1Gd2. Based on the formation of LPSO, Mg-Zn-RE alloys are divided into two categories: I) Mg-Zn-RE alloys including Y, Dy, Ho, Er and Tm elements, normally develop 18R type LPSO phase during solidification. The 18R type LPSO can transform into 14H type after heat treatment; II) In Mg-Zn-Gd and Mg-Zn-Tb, 14H type LPSO phases normally precipitate from supersaturated solid solution or transforms from other secondary phases during annealing at high temperatures. No LPSO phase is observed in as-cast ingots. Kawamura et al. [122] proposed general criteria for RE which forms LPSO phase in Mg-Zn-RE systems. The RE elements should have negative mixing enthalpy for the pairs Mg-RE and Zn-RE, exhibit hcp structure at room temperature, large solubility limits (above approximately 3.75 at.%)) in Mg and have larger atomic size than Mg by 8.4 to 11.9%. However, why the various RE performs differently in forming LPSO phase is still unknown. As Y and

Gd are the most common RE elements used in the Mg alloys, it is of great interest to investigate the effect of Gd addition in the Mg-Zn alloys with different Zn/Gd ratios.

Li et al. [123] studied the solidification and age hardening behaviour of an Mg-6Zn-2Gd (wt.%) alloy and it was seen that the microstructure of the as-cast samples comprised of equiaxed α-Mg grains surrounded by some eutectic compound both at triple points and along grain boundary. The eutectic compound was composed of $MgZn_2$, Mg_5Gd phases and α-Mg matrix. After solution treatment at 500 °C for 18 h, the eutectic compound almost dissolved, but some discontinuous second phase particles still survived at grain boundaries. The $Mg_3Gd_2Zn_3$ phase also formed during subsequent ageing. The Gd addition not only improved the thermal stability of the second phase formed during solidification, but also postponed the overaging during ageing at 200 °C up to 100 h. The precipitates were seen with three different morphologies: $[0001]_\alpha$ rods/lath, $(0001)_\alpha$ plates and blocky particles in the α-Mg matrix. The solute elements of Zn and Gd were found to partition into the precipitates, especially for the blocky particles. This significant partition can be correlated directly to the improved mechanical properties at higher temperature. The as-cast microstructure of ZG62 alloy consisted of α-Mg matrix and a eutectic phase ($\alpha+Mg_5Gd+MgZn_2$). During the subsequent heat treatment, $Mg_3Gd_2Zn_3$ phase also forms. The addition of Gd not only improved the thermal stability of the second phase formed during solidification, but also postponed the overaging during ageing at 200 °C up to 100 h. Juncai et al. [124] carried out different solution treatments at 480, 500 and 520 °C on the semi-continuously cast Mg96.34Gd2.5Zn1Zr0.16 alloy. It was found that different solution temperatures lead to the formation of different phases. Besides the α-Mg matrix and Zn-Zr compounds, the secondary phases along the grain boundaries change with solution temperature. At 480 °C and 500 °C, long period stacking ordered (LPSO)

structured X phases and residual eutectic compounds (Mg, Zn)$_3$Gd are seen, while at 520 °C, only residual eutectic compounds (Mg, Zn)$_3$Gd existed. The different microstructures solution treated at different temperatures lead to different mechanical properties and aging response. Higher solution temperature results in higher aging response and enhanced mechanical properties. The alloy solution treated at 520 °C for 8 h and aged at 200 °C for 64 h shows the best tensile properties at room temperature: ultimate tensile strength of 405 MPa, yield strength of 292 MPa and elongation of 5.3%. The influences of existing forms of Gd and Zn elements on tensile properties of Mg-Gd-Zn alloy were discussed, which indicates that the existing of Gd and Zn elements as precipitates lead to better strengthening effect than that in the form of LPSO structured X phase. Phase equilibria and transformations in ternary Mg-Gd-Zn alloys were studied by Joachim et al. [125] by investigating 22 samples with up to 40 at.% Gd and 60 at.% Zn. The results, combined with a critical review of literature data, were used to develop the thermodynamic descriptions of the Gd-Zn and the Mg-Gd-Zn systems and to formulate the Mg-Gd-Zn phase diagram in the entire composition range. In the ternary system the hexagonal long-period stacking ordered structure 14H, the hexagonal phase H1, $Gd_{11}Mg_{24}Zn_{64}$, and five solid solution phases with ternary compositions, $GdMg_5$, $GdMg_3$, $GdMg_2$, Gd(Mg,Zn), and W were found to be stable, whereas the icosahedral phase I, $GdMg_3Zn_6$, and other hexagonal phases were metastable. In addition, a new face-centered cubic stable phase $Gd_{20}Mg_{19}Zn_{81}$ was identified in the Mg-Gd- Zn system. The corrosion behavior of Mg-10Gd-xZn (x = 2, 6 wt.%) alloys in 0.5 wt.% NaCl solution was investigated by Srinivasan et al. [126] Microstructures of both alloys consisted of (Mg,Zn)$_3$Gd phase and lamellar long period stacking ordered (LPSO) phase. The morphology of the second phase at the grain boundary differed in both alloys: it was a continuous network structure in Mg10Gd6Zn,

whereas it was relatively discrete in Mg10Gd2Zn. The dendrites were finer in size and highly branched in Mg10Gd6Zn. The corrosion results indicated that the increase in Zn content increased the corrosion rate in Mg10GdxZn alloys. Micro-galvanic corrosion occurred near the grain boundary in both alloys initially as the grain boundary phase was stable and acted as a cathode, however, filiform corrosion dominated in the later stage, which was facilitated by the LPSO phase in the matrix. Severe micro-galvanic corrosion occurred in Mg10Gd6Zn due to the higher volume of second phase. The second phase stability at the grain boundary was altered and dissolved after the long immersion times. The NaCl solution chemically reacted with the grain boundary phase and de-stabilized it during the long immersion times, and was removed by the chromic acid used for the corrosion product removal. Another study by Srinivasan et al. [127] on the microstructure, mechanical and corrosion properties of four alloys, Mg-2Gd-2Zn, Mg-2Gd-6Zn, Mg-10Gd-2Zn and Mg-10Gd-6Zn (all in wt.%), prepared by gravity permanent mold casting showed that the intermetallic phases in the Mg-2Gd-2Zn alloy shows mainly (Mg, Zn)$_3$Gd phase whereas the Mg-2Gd-6Zn alloy exhibited both I (Mg_3Zn_6Gd) and (Mg, Zn)$_3$Gd phases. In addition, few Mg-Gd and Mg-Zn binary phases were also present in both alloys. Lamellar long period stacking ordered (LPSO) phase was observed in alloys containing high concentrations of Gd (Mg-10Gd-2Zn and Mg-10Gd-6Zn alloys) in addition to the continuously distributed (Mg,Zn)$_3$Gd phase along the grain boundaries and interdendritic regions. A small fraction of X phase ($Mg_{12}ZnGd$) was also present in Mg-10Gd-2Zn alloy. Mg-10Gd-xZn alloys (x = 2, 6) showed higher yield strength due to the higher solute contents and the presence of LPSO phase in the matrix, but showed poor elongation due to the coarse continuous second phase at the boundary. Low Gd-containing alloys exhibited better elongation to failure and moderate strength due to the lower volume fraction of fine scale second

phases. Corrosion resistances of the alloys declined with increase in the total amount of alloying elements. Increase in Zn content from 2% to 6% in Mg-2Gd-xZn alloys did not alter the corrosion properties much; however, this enhancement in the high Gd-containing alloys had significant detrimental effects on the corrosion properties due to the significant increase in the volume of the second phases. In all alloys, galvanic corrosion due to the second phase and filiform corrosion dominated the earlier stages of corrosion, and after long immersion times, the second phase, $(Mg,Zn)_3Gd$, was found to become unstable and dissolved, leading to intergranular corrosion.

Yang et al. [128] investigated the as-cast microstructures, tensile and creep properties of Mg-3.8Zn-2.2Ca-xGd (x = 0, 0.36, 0.88, 1.49 and 2.52 wt.%) magnesium alloys and the additions of 0.36 wt.% and 0.88 wt.% Gd to the Mg-3.8Zn-2.2Ca ternary alloy do not cause the formation of any new phases but the extra $Mg_3Gd_2Zn_3$ phases are formed in the two alloys with the addition of 1.49wt.% and 2.52wt.% Gd. Furthermore, the additions of 0.36-2.52 wt.% Gd to the Mg-3.8Zn-2.2Ca ternary alloy can effectively refine the grains of the alloy, and an increase in Gd content from 0.36wt.% to 2.52 wt.% causes the grain size to gradually decrease. In addition, the additions of 0.36-2.52 wt.% Gd to the Mg-3.8Zn-2.2Ca ternary alloy cause the $Ca_2Mg_6Zn_3$ phase to change from the initial continuous and/or quasi-continuous net to the quasi-continuous and/or disconnected shapes. The additions of 0.36-2.52 wt.% Gd to the Mg-3.8Zn-2.2Ca ternary alloy can improve the tensile properties of the alloy, and the alloy with the addition of 1.49 wt.% Gd showed the best tensile properties. In addition, the additions of 0.36- 2.52 wt.% Gd to the Mg-3.8Zn-2.2Ca ternary alloy didnot change the creep mechanism of the alloy. However, the creep properties of the Gd-containing alloys were improved, and an increase in Gd content from 0.36 to 2.52 wt.% cause the creep properties to gradually increase.

Amongst the Gd containing alloys with the additions of 0.36wt.%, 0.88 wt.%, 1.49 wt.% and 2.52 wt.% Gd, the alloy with the addition of 1.49 wt.% Gd exhibits the relatively optimal tensile and creep properties. Magnesium alloys are considered as good candidates for biomedical applications, the influence of Ce/La microalloying on the microstructure, mechanical property and corrosion performance of extruded Mg-5.3Zn-0.6Ca (wt.%) alloy has been investigated by Tong et al. [129] After Ce/La addition, the conventional $Ca_2Mg_6Zn_3$ phases are gradually replaced by new Mg-Zn-Ce/La-(Ca) phases (T1'), which can effectively divide the $Ca_2Mg_6Zn_3$ phase. The $Ca_2Mg_6Zn_3$/T1' structure in Mg-Zn-Ca-0.5Ce/La alloy was favorably broken into small particles during the extrusion, resulting in an obvious refinement of secondary phase. The dynamic recrystallized grain size is dramatically decreased after 0.5Ce/La addition, and the tensile yield strength is improved, while further addition reverses the effect, due to the grain coarsening. However, the corrosion resistance of extruded Mg-Zn-Ca alloy deteriorated after Ce/La addition, because the diameter of secondary phase particle was remarkably decreased, which increased the amount of cathodic sites and accelerates the galvanic corrosion process. A high-strength low-cost Mg-2.5Zn-0.3Ca-0.4La (mass%) alloy was fabricated by hot extrusion following direct chill casting by Du et al. [130] The as-cast alloy contains two intermetallics: $Ca_2Mg_6Zn_3$ and Mg-Zn-La-Ca phase of orthorhombic structure. Both distribute either at grain boundaries or in grains. The extrusion causes a bimodal microstructure containing fine DRXed grains and the deformed region. The average grain size of the DRXed region was 1.5 μm. Such bimodal microstructure was related to the undissolved coarse second phase promoting dynamic recrystallization and addition of trace elements retarding recrystallization through pinning grain boundaries and/or dislocation movement by segregating at grain boundaries and forming fine dynamic

precipitates. Fine $Ca_2Mg_6Zn_3$ and Mg_4Zn_7 particles precipitate during extrusion in both the deformed region and the DRXed region. Texture of the DRXed region is weaker than the deformed region, and no RE texture was observed in the DRXed region due to the low concentration of La in the matrix and/or very fine grain size. The strength improvement of the extruded alloy was mainly attributed to precipitate strengthening, dislocation strengthening in the deformed region and grain boundary strengthening in the DRXed grains. Yield strength (YS), ultimate tensile strength (UTS) and elongation to failure of the alloy are 325 MPa, 341 MPa and 15%, respectively. The high strength of the extruded Mg-2.5Zn-0.3Ca-0.4La alloy was mainly due to dense precipitation, grain refinement, and high density of dislocations. The extruded alloy exhibits a bimodal microstructure containing fine dynamic recrystallized (DRXed) grains and deformed regions. High density of dislocations was stored in the deformed regions while dense precipitates were homogeneously distributed in both the DRXed grains and the deformed regions. However, precipitates in the DRXed regions show in spherical shape only, while they were in rod-like shape and spherical shape in the deformed regions.The effect of Ce/La misch metal addition on the microstructural evolution of as-cast and as-soluted Mg-5.3Zn-0.5Ca (wt.%) alloys was systematically investigated by Zhang et al. [131] It was found that Ce/La could effectively refine the as-cast alloy and restrain grain growth during solution treatment, which was derived from the constitutional supercooling during solidification process and the formation of stable intermetallic compounds $CeMg_{12}$ and $Mg_{17}La_2$. Furthermore, Ce/La microalloying and solution treatment resulted in a transformation from the lamellar $Ca_2Mg_6Zn_3$/α-Mg to the divorced eutectic structure. The thermal stability of Mg-Zn-Ca alloy could be effectively enhanced by Ce/La addition, because the low-melting-point binary Mg-

Zn phase was transformed to Mg_xZn_y-Ca-(Ce/La) phase with higher thermal stability and the amount of $Ca_2Mg_6Zn_3$/α-Mg eutectic structure was reduced. The as-cast microstructures, tensile and creep properties of Mg-3.8Zn-2.2Ca-xGd (x = 0, 0.36, 0.88, 1.49 and 2.52 wt.%) magnesium alloys were investigated and compared by Yang et al. [128] The results indicate that the additions of 0.36-2.52 wt.%Gd to the Mg-3.8Zn-2.2Ca ternary alloy can refine the grains of the alloy, and an increase in Gd content from 0.36 to 2.52 wt.% causes the grain size to gradually decrease. Furthermore, the additions of 0.36-2.52 wt.% Gd to the Mg-3.8Zn-2.2Ca ternary alloy can also improve the tensile properties of the alloy, and the alloy with the addition of 1.49 wt.% Gd exhibited the best tensile properties. In addition, the additions of 0.36-2.52 wt.% Gd to the Mg-3.8Zn-2.2Ca ternary alloy do not change the creep mechanism of the alloy. However, the creep properties of the Gd-containing alloys are improved, and an increase in Gd content from 0.36 wt.% to 2.52 wt.% causes the creep properties to gradually increase. Amongst the Gd-containing alloys with the additions of 0.36 wt.%, 0.88 wt.%, 1.49 wt.% and 2.52 wt.% Gd, the alloy with the addition of 1.49 wt.% Gd exhibited the relatively optimal tensile and creep properties.

2.11 Shortcomings in the Literature

Due to the interest in lightweight automotive parts, the prime focus is on the research and development of magnesium alloys, which is extensively reported in the literature. As discussed earlier, Mg-Al and Mg-Zn alloys have numerous applications in automobile and aeronautical industries. Although Mg-Al alloys are one of the most successful commercial alloys and has been subject of research for the last 50 years, their application is still limited due to its limited strength and relatively low corrosion resistance when compared to its main competitor, the aluminium alloys. The poor high

temperature properties of Mg-Al alloys are attributed to the presence of thermally unstable $Mg_{17}Al_{12}$ phase at the grain boundaries. Minor alloying element addition is extensively used to enhance the tensile strength and corrosion resistance by modifying the microstructure of Mg-Al alloys. The aim is to suppress the discontinuous precipitates formation and/ or create thermally stable intermetallic precipitates. Enhancement in the corrosion resistance with respect to rise in high temperature tensile properties is a best option for increasing the application of Mg-Al alloy. RE addition is the best choice for attaining the aforementioned properties. Grain refinement and formation of RE-containing intermetallic phase results in improvement in high temperature tensile properties of Mg-Al alloys. The corrosion resistance of Mg-Al alloy by RE addition is due to (a) reduction impurities due to the formation of RE-intermetallic compound, (b) the Al-RE intermetallic phase formed by the reduction of $Mg_{17}Al_{12}$ phase is found to be less cathodic and therefore suppress micro-galvanic couples, (c) grain refinement and formation of more continuous $Mg_{17}Al_{12}$ phase. Gadolinium (Gd) is one of the active rare earth elements that have high affinity to aluminium and thus can reduce the formation of β- $Mg_{17}Al_{12}$ phase by consuming aluminium to form thermally stable intermetallic Al_2Gd phase and also it has an electro chemical potential almost near to that Mg. Wear is another major concern which restricts wide application of Mg alloys in automobile sector. Introduction of hard intermetallic phase by RE addition can greatly enhance the wear resistance at room as well as high temperatures. This is attributed to the thermally stable $Al_{11}RE_3$ intermetallic phase, which acts as a barrier to the dislocation movement and further plastic deformation. Thus, wear resistance is seen to improve by changes in microstructure, morphology and grain size. Literature reveals that very few works have been done on the wear behavior of Mg-Al alloys with RE addition and the combined

addition of Gd with other elements to improve high temperature tensile and corrosion properties. Expanding the potential application of Mg-Al is the primary purpose of the study. Hence, studies on increasing the application of Mg-Al magnesium alloy for powertrain application with supportive wear and corrosion resistance with individual and combined effect of Gd with Ca is highly essential.

Recently, a lot of studies have been carried out on the strengthening effects of the icosahedral quasicrystal phase (I-phase) in Mg-Zn-RE alloys, such as Mg-Zn-Y, Mg-Zn-Gd, and Mg-Zn-Ho etc systems, using hot deformation process etc. These alloys show a good combination of strength and ductility due to the strong interface between the I-phase and the Mg-matrix, which coming from the high symmetry and the quasiperiodicity of the I-phase. From the point of view for the mechanical improvement of Mg alloys, it seems that the formation of I-phase is very helpful. In addition, the presence of I-phase particles in the matrix was the effective method of improving the fracture toughness of Mg alloys. Due to high hardness and low friction coefficient of I-phase, Mg alloys reinforced with I-phase particles usually have superior wear resistance. Mg-Zn-Gd is one of the very important systems as its microstructure consists of many different phases, such as I, W, X and laves phases, depending on the ratio of Zn to Gd contents, thus resulting in different mechanical behaviors [22,25]. Thus, the mechanical properties of these alloys can be tailored accordingly by altering the Zn and Gd contents. The presence of the W-phase in Mg-Zn-Gd alloys is still contentious as some of the recent literature suggested that this phase was $(Mg,Zn)_3Gd$ type with fcc structure similar to the W-phase observed in Mg-Zn-Y systems but with slightly different lattice parameters. In order to fabricate the Mg alloy reinforced with I-phase, it is firstly crucial to explore the formation range of I-phase in one alloy system. Alloys with Zn/Gd ratio in the range of 0.25-1 consist of α-Mg and W-phase which is

one MgZnGd compound with f.c.c. structure. In the range of 1.5-6 for Zn/Gd ratio, I-phase (Mg_3Zn_6Gd) was detected besides α-Mg and W-phase ($(Mg,Zn)_3Gd$) and with further increasing Zn/Gd ratio, in the range of 10-40 for alloys with 5 at.% Zinc, as shown in Fig. 1(b), Mg-Zn-Gd alloys consist of only two phases, α -Mg and I-phase. Quasilattice parameter of I-phase in Mg-Zn-Gd alloys does not change with the alternation of Zn/Gd ratio of alloy. The presence of these phases was first identified in Mg-Zn-Y systems, and subjected to many investigations [132-135]. The relation between composition, microstructure and properties of Mg-Zn-Y based system in both as cast and heat treated conditions is well documented in the literature. However, the Mg-Gd-Zn system is relatively new, and has not been investigated in detail. Hence, to develop new Mg-Gd-Zn alloys with high strength, high creep and corrosion resistance, a thorough knowledge on the structure-property correlation of these alloys is essential. In the present investigation, Mg-Zn alloys containing individual and combined effect of Gd with Ca were prepared, and their microstructure, mechanical corrosion and wear properties are evaluated in the as-cast condition.

Chapter 3 Materials & Experimental Details

3.1 Introduction

Processing of the Mg-Al and Mg-Zn alloys with varying Gd and Ca additions, studies on their microstructural characterization, phase analysis, evaluation of mechanical (hardness and tensile), corrosion and wear properties are discussed here. The experimental procedure adopted for this study is shown as a flow chart (Fig. 3.1). The work mainly comprises of two parts:

Part I deals with the microstructural characterization and their effects on the mechanical, corrosion and wear properties of different Mg-Al-Gd and Mg-Al-Gd-Ca alloys and

Part II deals with the preparation and property evaluation of Mg-Zn-Gd and Mg-Zn-Gd-Ca alloys. The details of materials used and experimental procedures followed are given in the following sections:

3.2 Materials

3.2.1 Metals and alloying elements

The starting materials chosen to prepare the base Mg-Al and Mg-Zn binary alloys were

1. Pure magnesium ingots (99.7% purity)
2. Pure Al ingots (99.5% purity) and
3. Pure Zinc granules (99.98 % purity)

The following element and master alloy were used to modify the selected Mg-Al / Mg-Zn alloys:

1. Gadolinium (Gd) and
2. Magnesium-calcium master alloy (Mg-10Ca)

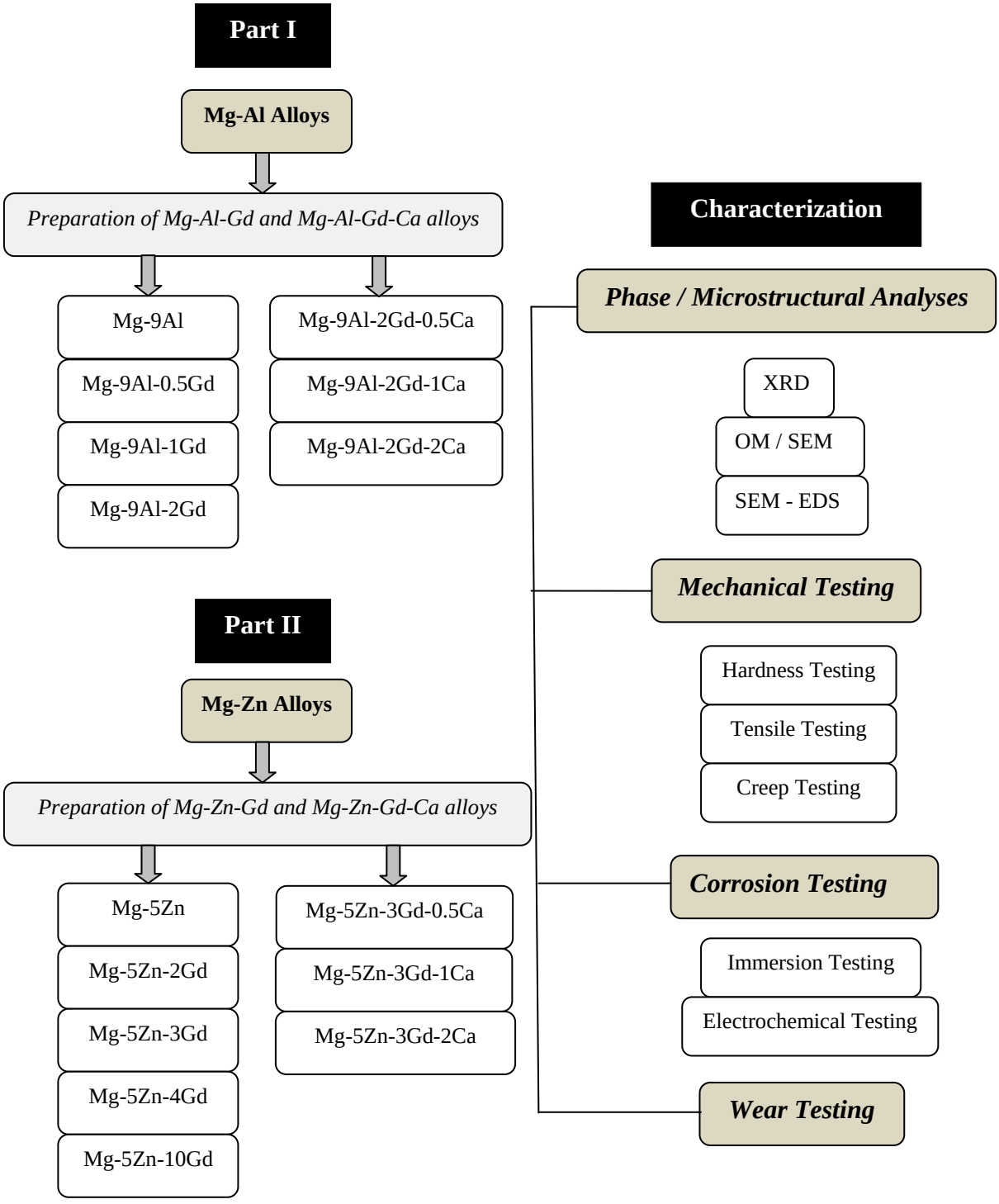

Fig. 3.1 *Flow chart of experimental procedure.*

3.2.2 Crucibles

Two stainless steel crucibles (grade: AISI 304, composition: C-0.08, Mn-2.0, P-0.045, S-0.03, Si-1.6, Cr-18.0/20.0 and Fe-66.3/74) having capacities of melting around 8 Kg and 5 Kg respectively were used to process the magnesium alloys. To avoid the

atmospheric contact as well as to reduce the oxidation of the Mg melt, the crucibles were covered with stainless steel lids during melting. The dimensions of the crucibles used for experiments are given in Fig. 3.2.

3.2.3 Mould

Rectangular cast iron moulds having magnesium castings capacity of 5 kg, and 2.8 kg were used. The schematic diagram of the moulds used in the experiments is shown in the Fig. 3.3.

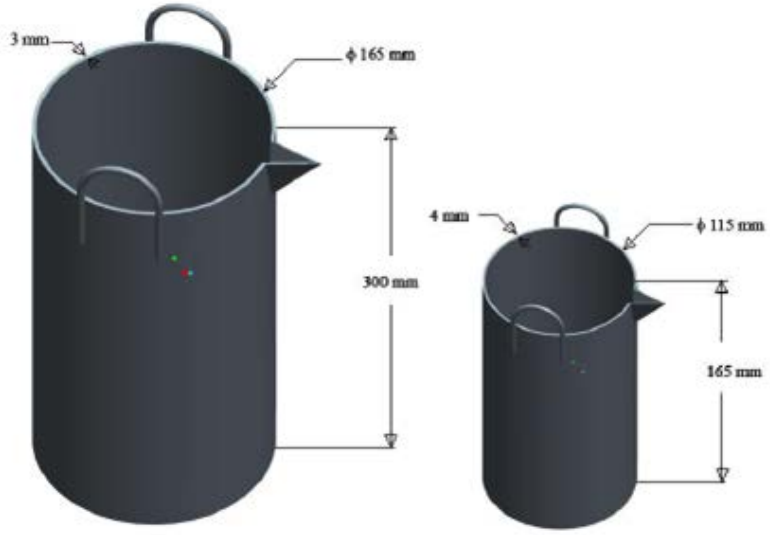

Fig. 3.2 *The stainless steel crucibles used to process Mg alloys.*

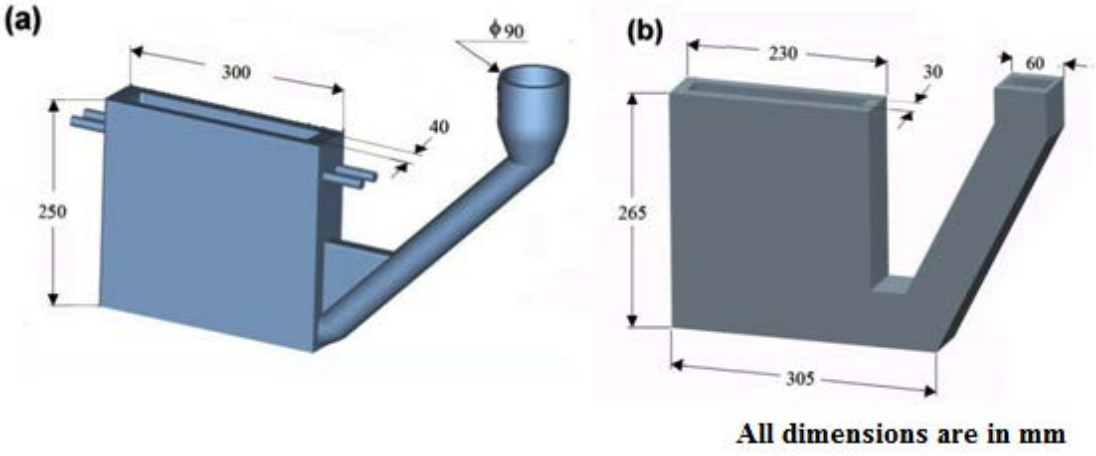

Fig. 3.3 *Schematic diagram of the moulds used.*

3.2.4 Protective gases

The Mg alloys should be protected against oxidation and burning during melting, alloying and subsequent casting. The porous MgO layer formed during Mg melting do not offer resistance to oxidation/burning. Protective gas mixture of SF_6 : Ar was used to counteract the same.

3.3 Melting and Refining

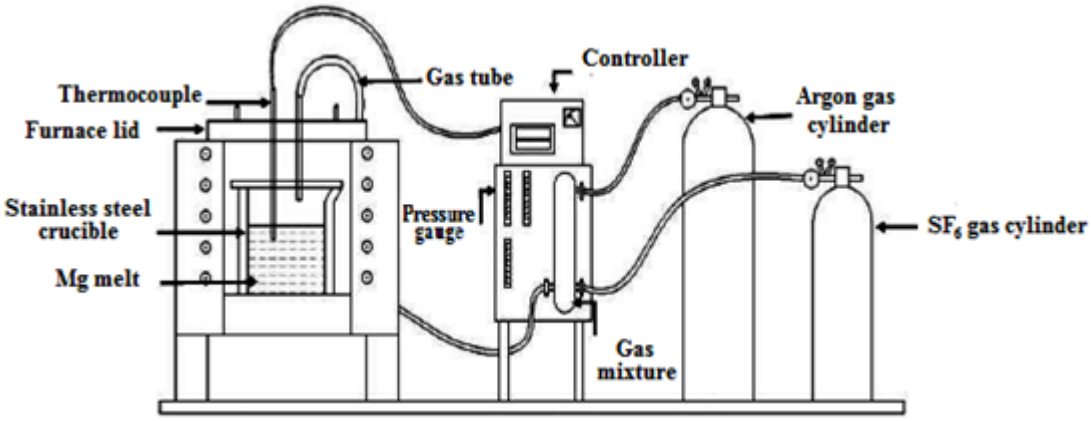

Fig. 3.4 *Schematic diagram of melting arrangement of Mg alloys.*

The schematic diagram showing the melting arrangement of magnesium alloys is presented in Fig 3.4. Resistance box furnace was used for melting. To prevent the oxidation and subsequent burning of Mg at high temperatures some form of oxidation prevention is always required. During the course of these experiments, a protective cover gas mixture of SF_6 : Ar in the ratio 1:100 was used to prevent reaction between the magnesium alloy and the surrounding air, thereby preventing oxidation of the melt. The cover gas was introduced to the furnace through a specially designed lid that contained holes for gas intake, exhaust, and for the positioning of a K-type thermocouple for temperature measurement.

After the crucible reached the red hot condition (750 ^{o}C), the preheated Mg ingots were charged into the crucible. Initially, only a part of the total Mg ingots was

charged. After melting of the charged ingots, the remaining ingots were immersed into the molten magnesium. This kind of charging practice of metal ingots avoided excessive oxidation during melting. Crucible was covered with furnace lid to minimize the air contact with the molten metal. Protective gas was given at the top of the melt to prevent oxidation. Before the addition of alloying elements, the top layer of oxides was completely removed and a fresh layer of flux was applied. The required amount of master alloys were weighed and wrapped in aluminium foil and slowly immersed into the melt. After the additions, the melt was gently stirred for dissolution of the added elements and again, the top oxide layer was removed and protective gas mixture was given. The melt was held for 10 minutes to ensure complete dissolution of elements into the melt. After complete melting of the metals in the crucible, the refining of the melt was carried out at a temperature of approximately 740 ^{o}C. The top layer (oxide layer) of the melt was then removed and the melt was rigorously stirred for 2-3 min. Continuous protective gas mixture was given throughout the top surface of the molten metal. After thorough mixing, the top surface of molten melt was removed and then the molten metal was poured into the preheated moulds (300 ^{o}C) in a heating oven for 1 hour just before the casting. The pouring was carried out smoothly without any jerk in the melt, since any jerks disturbs the settled oxide inclusions in the bottom. Protective gas mixture was also given on the mouth of the mould to avoid oxidation during poring. Three fourth of the melt was poured into the mould and the remaining melt was poured separately as scrap.

3.4 Material Characterization

Samples for different analyses such as chemical analyses, microstructure, hardness, tensile, corrosion and wear were machined out from the same location of the castings.

3.4.1 Chemical analyses

The analyzed alloy compositions are presented through Tables 3.1 - 3.4.

Table 3.1 *The chemical composition of the developed Mg-Al-Gd alloys.*

Alloy code	Composition	Al (wt.%)	Gd (wt.%)	Fe (wt.%)	Ni (wt.%)	Mn (wt.%)	Mg (wt.%)
0 Gd	Mg-9Al	8.55	-	0.0047	0.0001	0.0034	Rest
0.5 Gd	Mg-9Al-0.5Gd	8.54	0.57	0.0032	0.0001	0.0041	Rest
1 Gd	Mg-9Al-1Gd	9.10	1.25	0.0016	0.0001	0.0022	Rest
2 Gd	Mg-9Al-2Gd	8.77	1.97	0.0031	0.0001	0.0042	Rest

Table 3.2 *The chemical composition of the developed Mg-Al-Gd-Ca alloys.*

Alloy code	Composition	Al (wt.%)	Gd (wt.%)	Ca (wt.%)	Fe (wt.%)	Ni (wt.%)	Mn (wt.%)	Mg (wt.%)
0.5 Ca	Mg-9Al-2Gd-0.5Ca	8.63	1.93	0.47	0.0026	0.0001	0.0017	Rest
1 Ca	Mg-9Al-2Gd-1Ca	8.78	1.86	0.95	0.0033	0.0001	0.0023	Rest
2 Ca	Mg-9Al-2Gd-2Ca	8.77	1.84	1.93	0.0027	0.0001	0.0029	Rest

Table 3.3 *The chemical composition of the developed Mg-Zn-Gd alloys.*

Alloy code	Composition	Zn (wt.%)	Gd (wt.%)	Fe (wt.%)	Ni (wt.%)	Cu (wt.%)	Mg (wt.%)	Zn/Gd at ratio
0 Gd	Mg-Zn	4.87		0.006	0.0003	0.002	Rest	0
2 Gd	Mg-Zn-2Gd	5.13	1.95	0.004	0.0002	0.004	Rest	7
3 Gd	Mg-Zn-3Gd	5.22	3.06	0.005	0.0004	0.003	Rest	4
4 Gd	Mg-Zn-4Gd	4.96	3.89	0.007	0.0002	0.005	Rest	3
10 Gd	Mg-Zn-10Gd	5.26	9.95	0.004	0.0002	0.004	Rest	1

Table 3.4 *The chemical composition of the developed Mg-Zn-Gd-Ca alloys.*

Alloy code	Composition	Zn (wt.%)	Gd (wt.%)	Ca (wt.%)	Fe (wt.%)	Ni (wt.%)	Cu (wt.%)	Mg (wt.%)
0.5 Ca	Mg-5Zn-3Gd-0.5Ca	4.92	2.88	0.48	0.0039	0.0002	0.0023	Rest
1 Ca	Mg-5Zn-3Gd-1Ca	4.87	3.12	1.05	0.0001	0.0034	0.0001	Rest
2 Ca	Mg-5Zn-3Gd-2Ca	5.33	3.08	2.11	0.0025	0.0001	0.0027	Rest

3.5 Microstructural Characterization

3.5.1 Metallographic specimen preparation

3.5.1.1 Polishing

Cylindrical samples of 15 mm diameter and 10 mm height were machined from the castings and polished progressively with emery papers of different grades having 80, 100, 220, 400 and 600 and 1000 grits. After paper polishing, all the samples were cleaned using water and polished on a rotating disc of proprietary cloth (selvyte cloth) charged with a diamond paste of 6, 3 and 0.25 μm particle size in sequence. Filtered kerosene was used as lubricating agent during cloth polishing. During cloth polishing, samples were gently pressed against the rotating wheel. Since Mg is a soft material, much care was taken during polishing to avoid scratches and excessive surface contamination. Since, cleaning the polished samples with water (even with distilled water) was found to be inefficient to remove surface contaminants, ethanol with ultrasonic cleaner was used to clean the polished samples to remove the contaminants.

3.5.1.2 Chemical etching

Picric acid found to be an efficient etchant which clearly revealed the micro constituents in the Mg alloys. During cloth polishing, samples were gently pressed against the rotating wheel. Since Mg is a soft material, much care was taken during polishing to avoid scratches and excessive surface contamination. Since, cleaning the polished samples with water (even with distilled water) was found to be inefficient to remove surface contaminants, ethanol with ultrasonic cleaner was used to clean the polished samples to remove the contaminants.The composition of the etchant used in the present study is: *Picric acid – 6 grams; Acetic acid – 5 ml; Ethanol – 100 ml and Distilled water – 10 ml.* The etching time was found to be optimum with 10-30 seconds

for different element added alloys. During etching, more care was taken to avoid over etching of the samples which would otherwise spoil the surface of the samples.

3.5.2 Optical microscope (OM)

Microstructural specimens (after polishing and etching) were observed under a Leica DMRX optical microscope. The microscope had six magnification lenses: 5x, 10x, 20x, 50x, 100x and 150x. Micrographs were taken at different location with various magnifications to understand various microstructural changes in the alloys with respect to different additions.

3.5.3 Phase fraction analyses

Quantitative microstructural analyses were carried out using a Leica 2001 image analyzer in conjunction with the optical microscope. The fields of observations were selected randomly at different locations of the sample. Q-Win image analysis software attached with OM is used for phase fraction analysis. The software was calibrated before taking any measurement using standard ruler provided by the manufacturer. At least 20 random fields were analyzed in different regions of the studied alloys. For each case, at least ten fields were analyzed from a single specimen and the average value is reported.

3.5.4 Scanning electron microscope (SEM)

To understand the microstructural aspects and to identify the type of phase formations in various castings with higher magnification, using JEOL, JSE 35C scanning electron microscope (SEM) was used with an accelerating voltage of 15-30 KeV. The same optical microstructural samples were used for SEM studies also. For SEM images, the extracted powders were gold coated to reduce the charging and to improve image quality. The compositions of various phases and intermetallics were

analyzed using Energy dispersive spectroscope (EDS) attached to SEM. Most SEM images were taken using secondary electrons (SE) although some images have been acquired from back scattered electrons (BSE).

3.5.5 Grain Size Measurements

Grain size measurements were carried out using linear intercept method from different locations and the average is taken, outlined in the ASTM standard E112-96, 2003. The samples are solutionized, quenched and aged for measuring the grain size.

3.6 Phase Identification

3.6.1 X-ray diffraction (XRD)

X- ray diffraction was carried out on all the cast alloys to study the kind of intermetallics present in the developed alloys. For these purpose, fine chips drilled from the castings and made into fine powder which was used for XRD analyses purpose. The study was carried out on Phillips PW 1710 Powder Diffractometer with Cu-Kα radiation (wavelength of 1.54 Å). The X-ray source was operated at a voltage of 40 kV and current of 20 mA. The diffraction angle (2θ angle) selected for these alloys were such that all the major intense peaks of the phases expected in the sample were covered. Subsequently, the XRD raw data were analyzed with the help of JCPDS data file and X′Pert software, which use the Bragg's law to identify the peaks of the constituent phases.

3.6.2 Energy dispersive spectroscope (EDS)

The composition of various phases and intermetallics were analyzed using energy dispersive spectroscope (EDS) microanalyser attached with SEM and it was interfaced with ISIS software for EDX line scan, surface scan and X-ray elemental mapping analyses. Same samples prepared for microstructural studies were used for

these analyses. An average of 10 EDS measurements were used to approximate the composition of phases.

3.7 Mechanical Properties

3.7.1 Hardness test

The macro hardness of the alloys were measured using INTENDEC hardness machine with a load of 62.5 kgf with a dwelling time of 20 sec and the ball indenter diameter of 2.5 mm on polished specimens. 5 indentations were made and the average values are taken. Samples used for hardness measurements were aptly polished to do the measurements. The opposite surfaces were parallel to each other to obtain accurate measurements. The Brinell Hardness Number (BHN) is given by the formula:

$$BHN = 2P/ [\pi D (D-(D^2-d^2)^{1/2})]$$

Where P is applied load (Kgf), D is diameter of the indenter ball (mm), and d is diameter of the impression (mm).

3.7.2 Tensile test

Room and high temperature (150 ^{o}C) tensile tests were carried out using computer controlled INSTRON 8801 universal testing machine. For high temperature testing, the samples were heated in an oven attached with the INSTRON machine and kept for 15 min after the required temperature (150 ^{o}C) was reached so as to ensure the homogenization of temperature throughout the sample. Ultimate tensile strength, yield strength and elongation values were obtained directly from the computer interfaced with the machine. The tensile specimens were prepared as per ASTM E8 specifications. The room and high (150 °C) temperature tensile tests were performed using an Instron universal testing machine (Instron Corp., England) with a crosshead speed of 2 mm/min. At least six specimens were tested from each casting and the average values

were reported. The schematic diagram of tensile test specimen used for the present study is given in Fig. 3.5. Ultimate tensile strength (UTS), yield strength (YS) and elongation (% E) were obtained directly from the computer interfaced with the machine. An extensometer was used to get the % elongation during tensile testing.

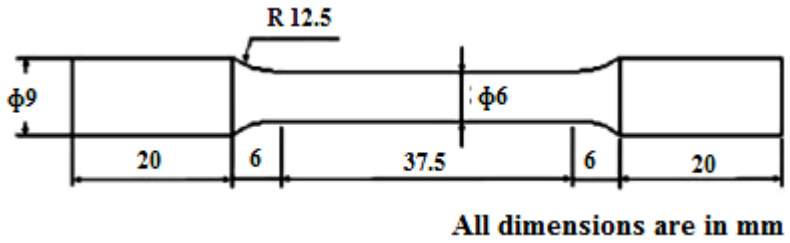

Fig. 3.5 *Tensile test specimen.*

3.7.3 Creep test

The constant load creep tests upto failure were performed on the developed alloys at constant temperature and initial stress of 150 ºC and 50 MPa respectively, as per the ASTM test standard of E-139, on a 5 ton servo electric creep testing machine (STS make India). The temperature of the sample during creep testing was maintained within ±1 ºC using a three zone heating furnace. The sample was mounted in a four rod in tube extensometer, and creep extension was measured using a dial gauge. The schematic diagram of creep test specimen is depicted in Fig. 3.6.

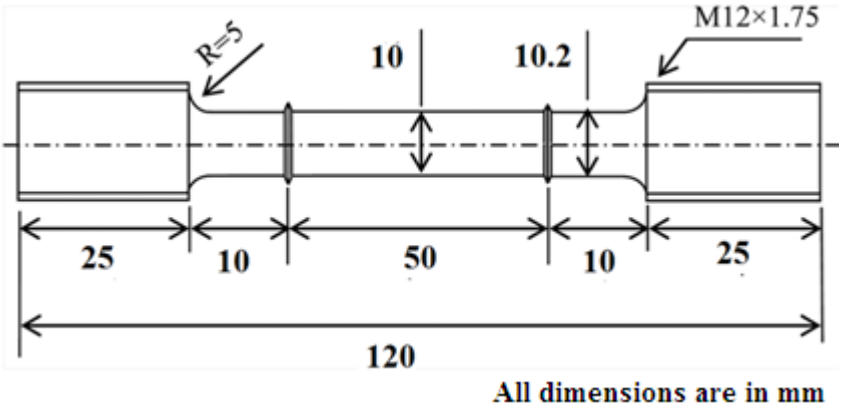

Fig. 3.6 *Creep test specimen.*

3.8 Corrosion Test

3.8.1 Immersion test

For constant immersion testing, samples of size 15mm x 15 mm were subsequently polished and cleaned with acetone. These samples were weighed and immersed in 3.5 % NaCl solution for 72 h. After the immersion test, these samples were cleaned using a solution containing 200 g/ltr CrO_3 and 19 g/ltr $AgNO_3$ for 10 minutes to remove corrosion products. Finally they were cleaned, dried and weighed. 3 sets of samples were used from each casting for carrying out the immersion testing and the average values were reported. The corrosion rate was calculated using the equation given below:

$$\boldsymbol{CR\ (mm/year) = \frac{8.76 \times 10^4 \times \Delta g}{A \times t \times \rho}}$$

Where, Δg is the weight loss in g, A is the surface area exposed in cm^2, t is the total immersion time in hours and ρ is the density of the alloy in g/cm^3.

3.8.2 Electrochemical test

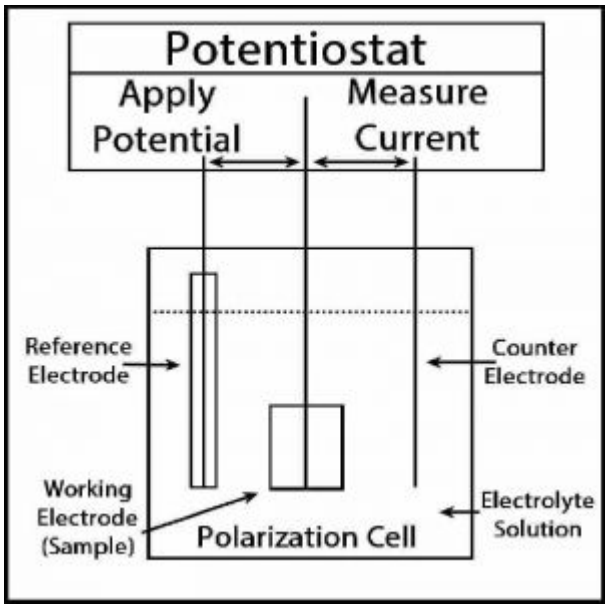

Fig. 3.7 *Schematic diagram of the electrochemical cell.*

The electrochemical properties were analyzed using a PGSTAT30 electrochemical workstation at room temperature (27±1 °C) and 3.5 wt.% NaCl solution was used as the electrolyte. A three-electrode cell was employed in this test, where the sample acted as the working electrode, a saturated calomel electrode (SCE) as the reference electrode, and a platinum sheet as the counter electrode. The scanning rate used was 2 mV/s. Based on the Tafel extrapolation method, the CH instrument software was used to measure the corrosion current density (i_{corr}) of the specimens. A schematic diagram of the electrochemical cell is shown in Fig. 3.7

3.9. Dry Sliding Wear Test

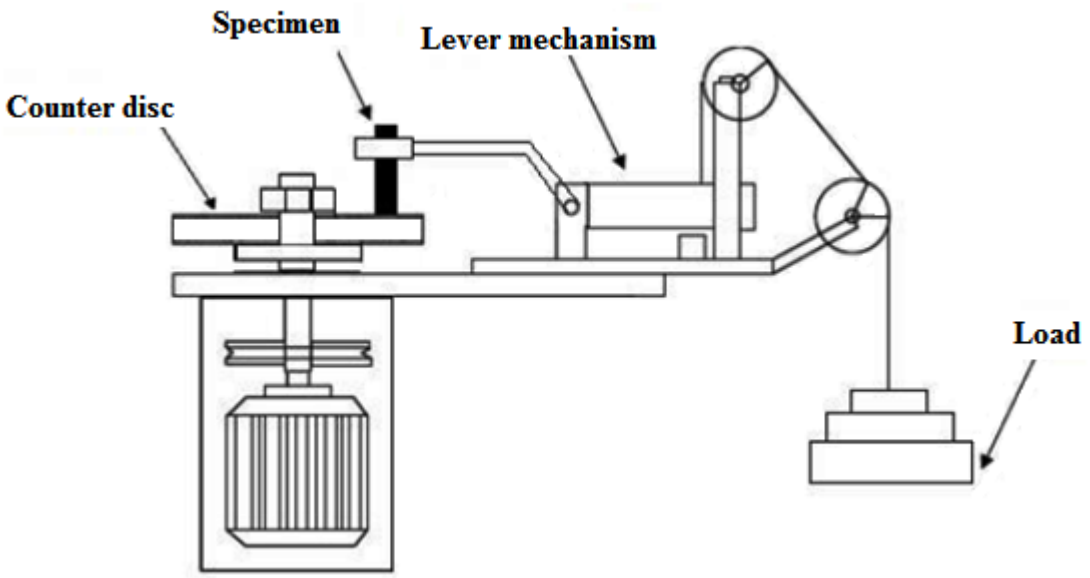

Fig. 3.8 *Schematic diagram of the Pin-on-Disc type wear testing machine.*

Dry (unlubricated) sliding wear tests were performed using a computerized pin on disc wear testing machine (Model type TR-20, DUCOM) according to ASTM G99-05 (ASM, 1992) standard to evaluate the wear behavior of the experimental alloys. The schematic diagram of the wear testing machine used in this study is shown in the Fig. 3.8. The disc used was EN-32 steel having hardness value of HRC 65, diameter of 160 mm and thickness of 8 mm. Specimens of 6 mm diameter and 30 mm length machined

out from the castings were used as the test samples. Wear test were carried under varying loads of 5, 10, 20, 30, 40 and 50 N at 240 rpm and a constant sliding distance of 1800 m. Room temperature wear tests were carried out without any lubrication. The process of sliding was carried out on a track of 50 mm radius, such that the linear circumferential (in tangential direction) speed was 1 m/s prior to the tests, both pin and disc were polished to have a uniform surface roughness.

A computer-aided data acquisition system was used to record both weight loss and frictional force simultaneously, with the volumetric loss being calculated from the former data. For each condition, 5 samples were tested and the average values were used for further calculation. The wear rate was calculated by measuring the weight loss of the specimen before and after the test as shown in the equation below:

Wear rate = volume loss (mm^3) / sliding distance (m)

Chapter 4 Microstructure Study of the Developed Alloys

4.1 Introduction

The present chapter deals with the detailed microstructural characterization of Mg-Al alloys with varying Gd additions. Mg-Zn-RE are relatively new alloy systems and their microstructure consists of many phases such as I, W, X and laves phases, depending on Zn/RE ratio which imparts different mechanical behaviors [136-138]. These phases were first identified in Mg-Zn-Y alloy systems, and the relationship between microstructure, composition, and properties of the same in both as cast and heat treated conditions is well documented. However, the Mg-Zn-Gd system is comparatively new and has not been investigated in detail. Hence, to develop high strength, corrosion and wear resistant new Mg-Zn-Gd alloys, a thorough study on the microstructure of the alloys is essential. Modification is a well-known foundry practice employed for refining/modifying the large particles/phases into fine particulates during solidification In the present study, Ca in varying wt.% is added to the optimal Mg-Al-Gd and Mg-Zn-Gd alloys and the microstructures are studied.

4.2 Mg-Al-Gd Alloys

4.2.1 XRD and microstructure analyses

The XRD pattern of the developed alloys (Fig.4.1) mainly consists of peaks corresponding to α-Mg and β-$Mg_{17}Al_{12}$ phase of bcc crystal structure. For the Gd added alloys, the peaks corresponding to Al_2Gd (fcc crystal structure) are of low intensities due to relatively low quantities of Gd addition.

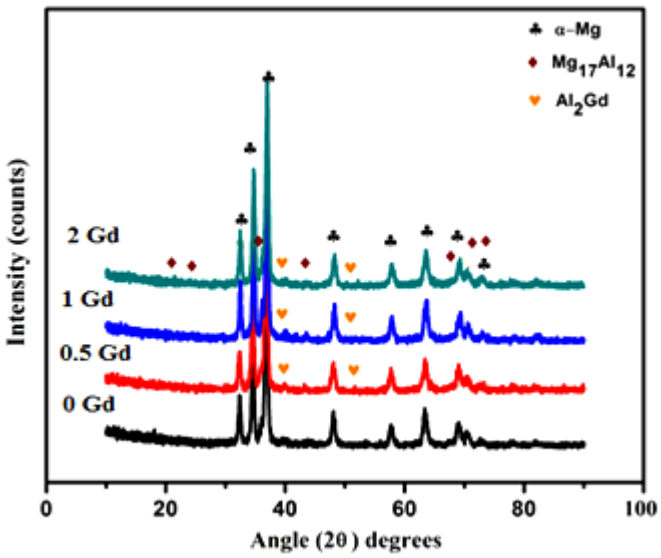

Fig. 4.1 *XRD results of the Mg-Al-Gd alloys.*

Fig. 4.2 depicts the optical and SEM microstructures of the Mg-9Al-xGd alloys and the various phase formations and the phases are further confirmed using EDS analysis (Fig. 4.3). Some dispersed particles and eutectic areas are seen in the alloys, which increase with increase in Gd content monotonically. The electronegativity difference between two elements can be used to predict the possibility of formation of intermetallics. The larger the electronegativity difference, the stronger the bond and higher the possibility of formation of intermetallics. As the electronegativity difference between Al and Gd is higher (0.3) than that between Mg and Gd (0.11), the formation of Al-Gd phase is favored than Mg-Gd phase in the Mg-Al-Gd system, and it is observed that the Gd addition decreased the quantity of $Mg_{17}Al_{12}$ phase [139-143]. The variation of β phase for the developed alloys quantified using Image Analyzer. The volume fraction of β phase in 0 Gd, 0.5 Gd, 1 Gd, and 2 Gd alloys are found to be decreasing in the order 19.5, 17.2, 16.5 and 15.3% respectively. The results indicate that the microstructure of the Mg-9Al alloy consists only coarse $Mg_{17}Al_{12}$ (Fig. 4.2(a)). With the addition of 0.5 wt.% Gd, the microstructure of the Mg-9Al-0.5Gd alloy show granular Al_2Gd intermetallic particles sparsely distributed in the Mg-Al matrix (Fig.

4.2(b)). Increasing the content of Gd to 1 and 2 wt.% in the Mg-9Al-xGd alloy increase the Al_2Gd phase distribution in the matrix. As seen from the optical microstructures, it can be seen that microstructure becomes refined with decrease in the volume fraction of $Mg_{17}Al_{12}$.

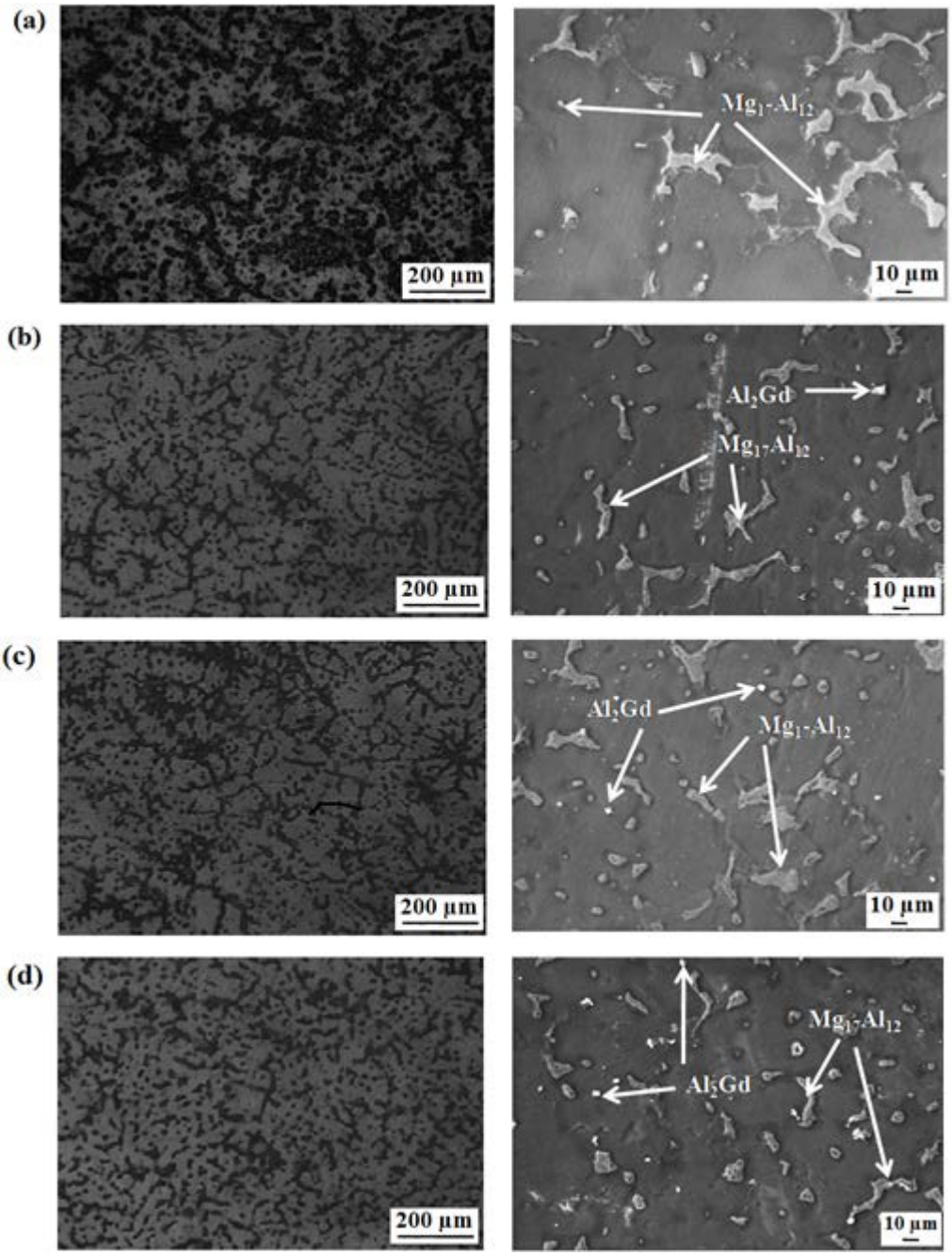

Fig. 4.2 *Optical and SEM microstructures of (a) 0 Gd, (b) 0.5 Gd, (c) 1 Gd, and (d) 2 Gd alloys.*

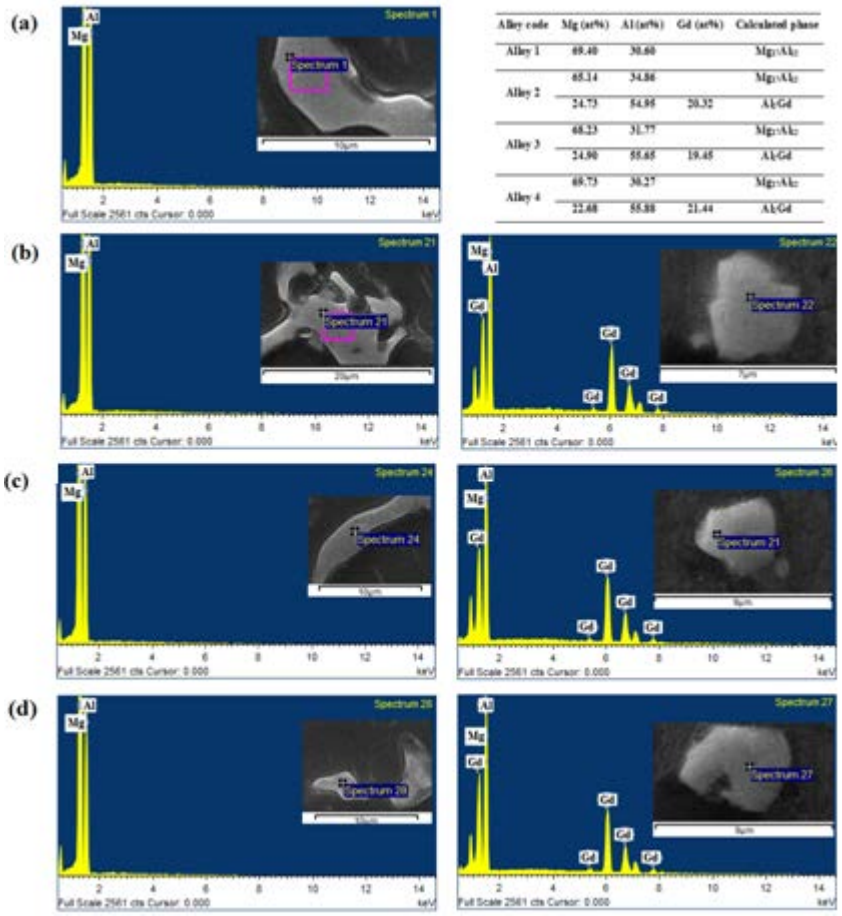

Alloy code	Mg (at%)	Al (at%)	Gd (at%)	Calculated phase
Alloy 1	69.40	30.60		$Mg_{17}Al_{12}$
Alloy 2	65.14	34.86		$Mg_{17}Al_{12}$
	24.73	54.95	20.32	Al-Gd
Alloy 3	68.23	31.77		$Mg_{17}Al_{12}$
	24.90	55.65	19.45	Al-Gd
Alloy 4	69.73	30.27		$Mg_{17}Al_{12}$
	22.68	55.88	21.44	Al-Gd

Fig. 4.3 *EDS results of (a) 0 Gd, (b) 0.5 Gd, (c) 1 Gd, and (d) 2 Gd alloys.*

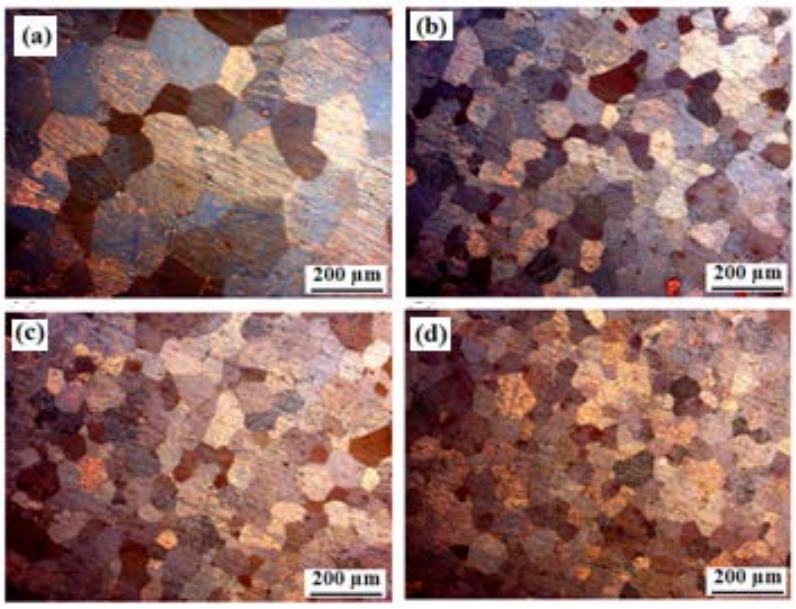

Fig. 4.4 *Grain size of (a) 0 Gd, (b) 0.5 Gd, (c) 1 Gd, and (d) 2 Gd alloys.*

For the Mg-Al system, the samples are solutionized at 420 ºC for 48 hours and aged at 200 ºC for 1 hour to measure the grain sizes. Due to the rise of temperature, the solid solubility of Al in the Mg matrix increases and the β-$Mg_{17}Al_{12}$ phase along the grain boundary dissolves in α-Mg matrix gradually. In the following cooling process, β-$Mg_{17}Al_{12}$ phase precipitates from α-Mg supersaturated solid solution due to the higher temperature, and disperses in α-Mg matrix as small particles along grain boundaries. The average grain size is seen to be around 200, 140, 120, and 100 μm for the 0 Gd, 0.5 Gd, 1 Gd, and 2 Gd alloys respectively (Fig. 4.4). The first solid phase in the molten pool is Al_2Gd, as a result of its highest melt point of 1525 °C. In the next moment, the α-Mg matrix starts nucleation around along the Al_2Gd particles. The higher the Gd content is, the more the Al_2Gd particles are dispersed in the liquid phase and thus the further the grain sizes of α-Mg matrix are decreased.

4.3 Mg-Al-Gd-Ca Alloys

4.3.1 XRD and microstructure analyses

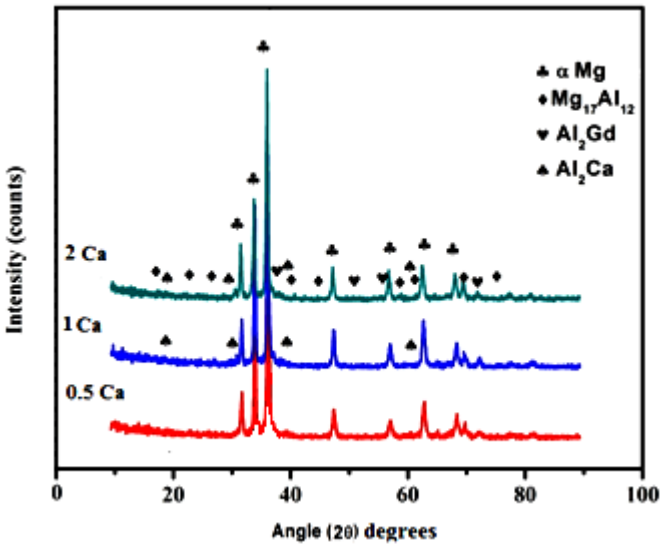

Fig. 4.5 *XRD results of the Mg-Al-Gd-Ca alloys.*

The XRD patterns of Mg-9Al-2Gd alloy with varying Ca (0.5, 1 and 1.5 wt.%) are presented in Fig. 4.5. The major peaks correspond to α-Mg, β-$Mg_{17}Al_{12}$ and Al_2Gd phases. Additional peaks for Al_2Ca phase are observed in the 1 wt.% and above Ca added alloys. The peaks corresponding to Al_2Gd and Al_2Ca are of low intensities due to relatively low quantities of Gd and Ca addition.

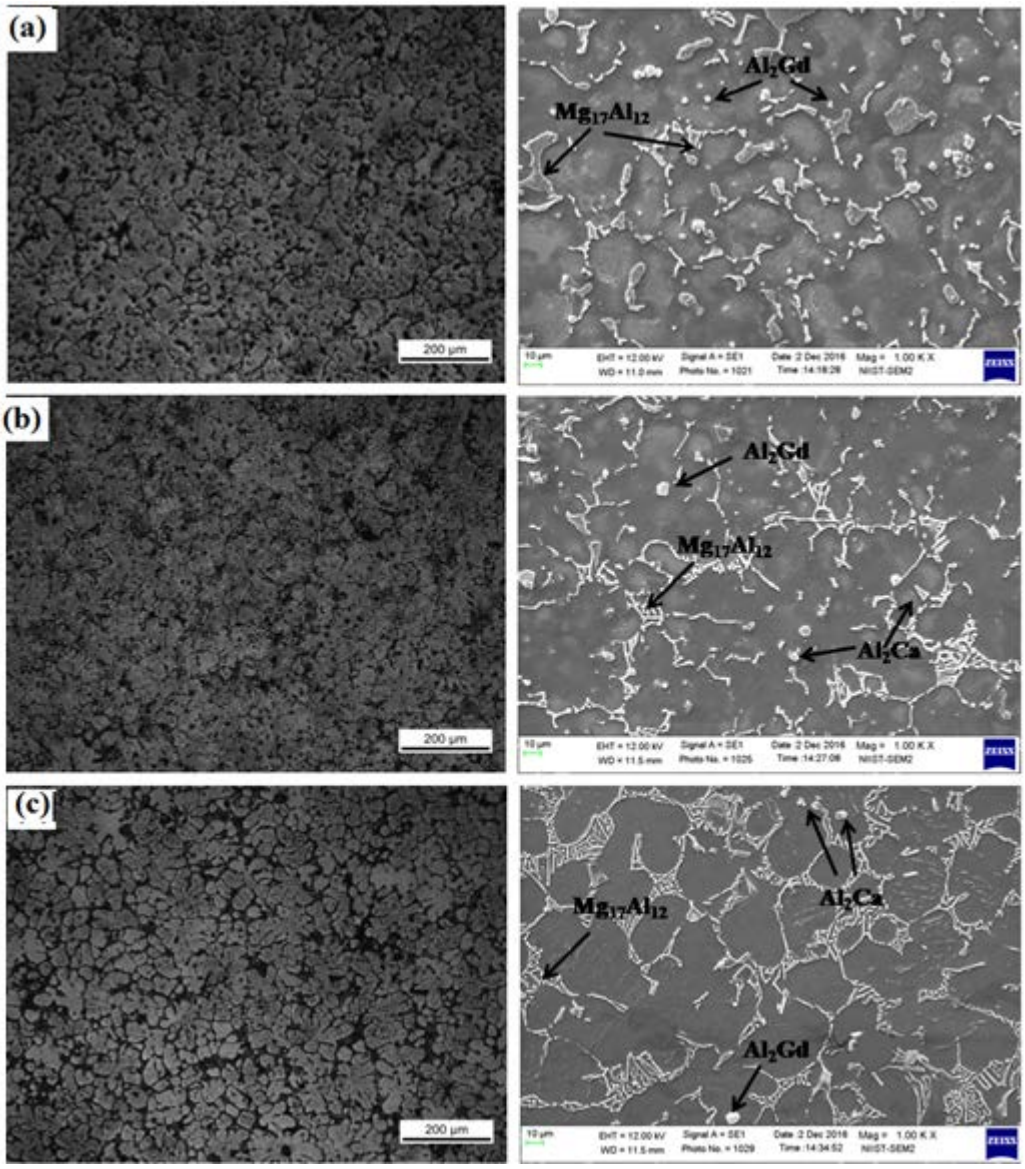

Fig. 4.6 *Optical and SEM microstructures of (a) 0.5 Ca, (b) 1 Ca, and (c) 2 Ca alloys.*

From the optical and SEM microstructures (Fig. 4.6), it is seen that the amount of massive β-$Mg_{17}Al_{12}$ phase has been significantly reduced. The EDS analyses of the different phases are shown in Fig. 4.7. Previous studies show that the Al_2Gd and Al_2Ca

compounds forms before β-$Mg_{17}Al_{12}$ phase by the consumption of Al atoms, resulting in the decrease of the volume fraction of β-$Mg_{17}Al_{12}$ phase [144-149]. The $Mg_{17}Al_{12}$ phases in all the alloys are incorporated with Ca atoms. Additional Al_2Ca phases are formed as the Ca content reached 1 wt.% and the volume fraction of these phases increased above 1 wt.% Ca addition. The electronegativity of Mg, Al and Gd are 1.31, 1.61 and 1.2, respectively. Due to the large electronegativity difference between Al and Gd, new Al-Gd rich phases are formed. Furthermore, Ca has a strong affinity to Al, and hence with decreasing temperature, the Ca and Al are pushed to the solid/liquid interface front, resulting in the formation of Al_2Ca phase. A large quantity of Al is consumed when Al_2Ca and Al_2Gd phase forms thereby suppressing the generation of $Mg_{17}Al_{12}$ phase and inhibiting the dendritic growth; therefore, adding Ca and Gd reduces the volume fraction of $Mg_{17}Al_{12}$ phase. As seen in Fig. 4.8, the grain size of Mg-Al-Gd-Ca alloy can be said to be decreasing till 1 wt.% Ca addition. The average grain size is seen to be around 94, 86, and 130 μm for the 0.5 Ca, 1 Ca, and 2 Ca alloys respectively (Fig. 4.8). During solidification, the Al_2Gd phase first precipitates among the inter-dendritic α-Mg phase and hinder other element diffusion. The $Mg_{17}Al_{12}$ phase is seen to be refined and its distribution becomes more uniform. It can be presumed that the Al_2Ca phase can dissolve into the melt and subsequently precipitate during solidification, eventhough the melting point of Al_2Ca (1079 °C) is higher than the melt temperature (720 °C). So, at the initial stage of solidification, the solute segregation of Ca at solid/liquid interface can provide stronger constitutional undercooling for nucleation. It can be said that grain refinement by the Al_2Ca compounds was mainly attributed to the combined effects of solute and heterogeneous nucleation. With further increase in Ca adition above 1 wt.%, the Al_2Ca phase becomes coarse and the nucleating particles are difficult to disperse. Correspondingly, the number of effective

heterogeneous nuclei decreases, which decreases the grain refining efficiency of Al_2Ca. Since the Ca/Al ratios are lower than 0.50, phases like $(Mg,Al)_2Ca$ and Mg_2Ca are absent [150-152].

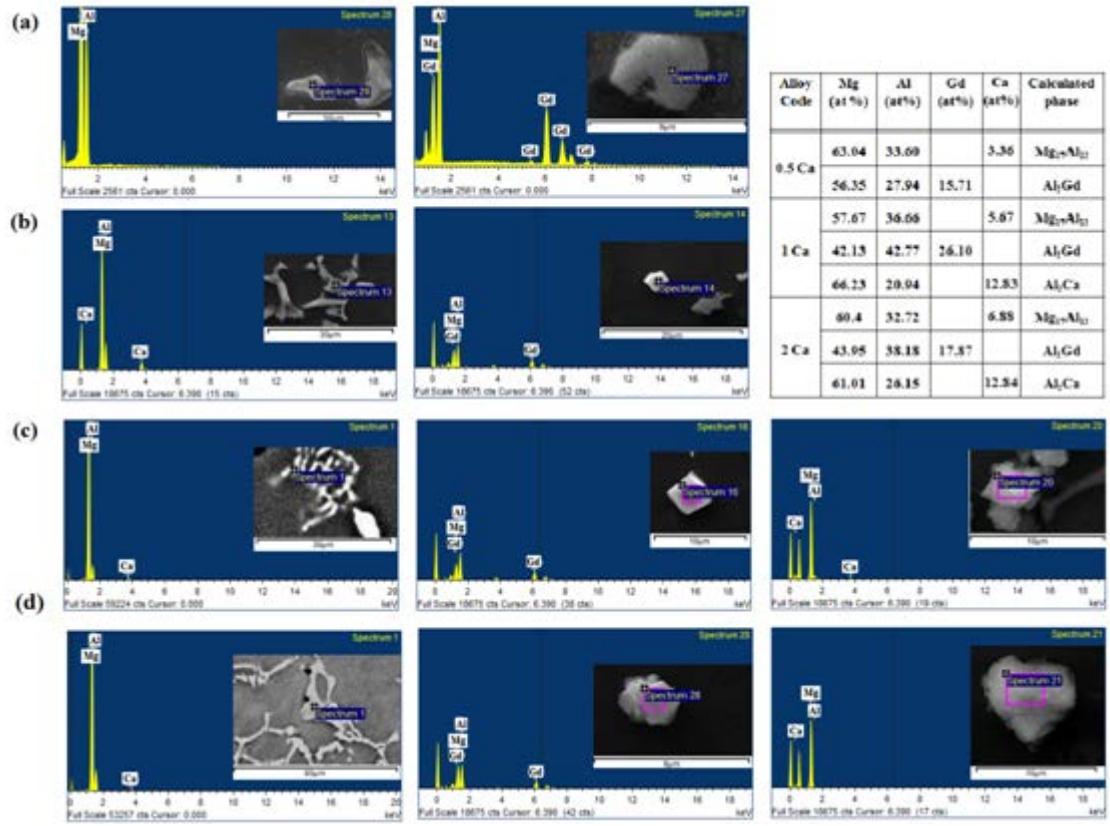

Alloy Code	Mg (at %)	Al (at%)	Gd (at%)	Ca (at%)	Calculated phase
0.5 Ca	63.04	33.60		3.36	$Mg_{17}Al_{12}$
	56.35	27.94	15.71		Al_2Gd
1 Ca	57.67	36.68		5.67	$Mg_{17}Al_{12}$
	42.13	42.77	26.10		Al_2Gd
	66.23	20.94		12.83	Al_2Ca
2 Ca	60.4	32.72		6.88	$Mg_{17}Al_{12}$
	43.05	38.18	17.87		Al_2Gd
	61.01	26.15		12.84	Al_2Ca

Fig. 4.7 *EDS result of (a) 0.5 Ca, (b) 1 Ca, and (c) 2 Ca alloys.*

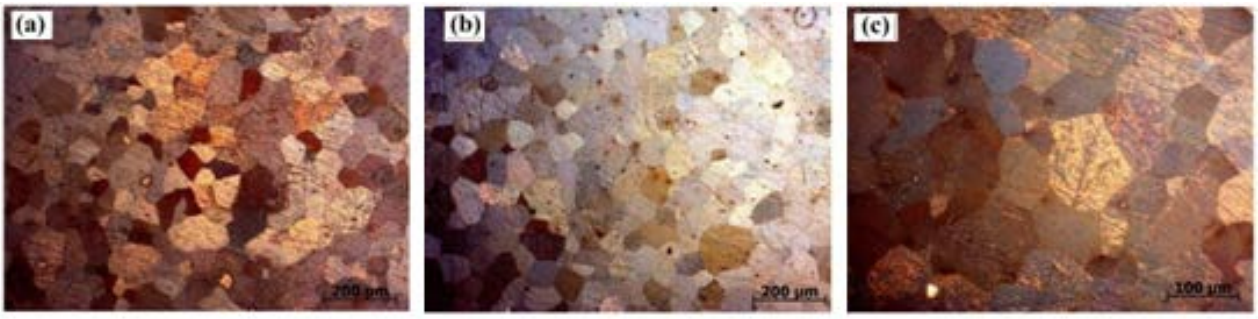

Fig. 4.8 *Grain size of (a) 0.5 Ca, (b) 1 Ca, and (c) 2 Ca alloys.*

4.4 Mg-Zn-Gd Alloys

4.4.1 XRD and microstructure analyses

Fig. 4.9 reveals the XRD diffraction patterns of the developed alloys. Apart from the common magnesium peaks, the patterns are different from each other, suggesting that the alloys contained different second phases. The diffraction pattern of Mg-5Zn showed peaks that correspond to the $MgZn_2$. In 2 Gd, 3 Gd, 4 Gd and 10 Gd, peaks that correspond to the Mg_3Gd type phase are seen with a small deviation in 2θ from the standard peaks due to the dissolution of Zn in the Mg_3Gd phase. This phase could be identified as $(Mg, Zn)_3Gd$ phase. In addition to $(Mg, Zn)_3Gd$ phase, peaks corresponding to Mg_3GdZn_6 are also observed in 2 Gd, 3 Gd and 4 Gd alloys. In contrast, 10 Gd alloy showed peaks for $Mg_{12}GdZn$ (X-phase), in addition to those of $(Mg, Zn)_3Gd$. The diffraction patterns of Mg–Zn-Gd alloys in the present study are indexed with reference to Mg–Zn–Y phases as the data available for Mg–Zn-Gd phases are limited. It is seen that the peaks for Gd containing phases deviated slightly from the standard peaks of Y containing phases. No peaks for Mg–Zn or Mg–Gd binary phases are seen in the XRD patterns of the ternary alloys.

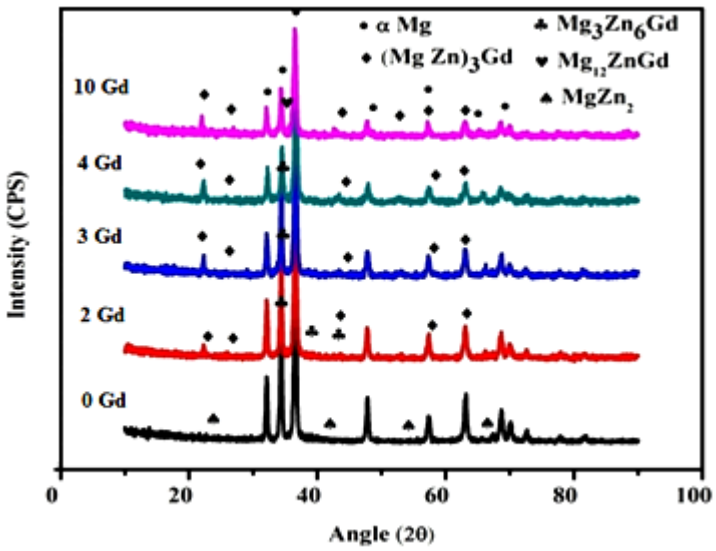

Fig.4.9 *XRD results of the Mg-Zn-Gd alloys.*

Fig. 4.10 presents the optical and SEM images of the developed alloys. Discontinuous secondary phases are seen to disperse in the matrix and the secondary phases are identified by means of EDS analysis. From the XRD and EDS analysis the phase formation in 0 Gd is confirmed to be $MgZn_2$. It is seen that the volume fraction of the second phases increased from 2 Gd to 10 Gd alloys, due to the increase in Gd content. 2 Gd alloy shows a less number of second phases but with different morphologies like small sized spherical particles, rod shaped structure and bulk sized phases. 3 Gd alloy shows the presence of a small fraction of a network like structure in addition to the earlier mentioned morphologies. From the EDS analyses, it is seen that for both 2 Gd and 3 Gd alloys, the spherical and network like phases contained more Zn than Gd in both the alloys. The Zn/Gd ratio as seen in Table 4.1, are found to be close to the ideal Zn/Gd ratio of 1.5 for $(Mg,Zn)_3Gd$ (W-phase) for the spherical and rod shaped phases [153-160]. For the bulk phases, the Zn/Gd ratio is around 6, the ideal ratio for Mg_3GdZn_6 (I-phase) [160,161]. When the Gd content is increased from 3 to 4 wt.%, the microstructure appeared to have a higher number of second phases than 3 Gd alloy. A semi continuous network rib bone shape morphology in 4 Gd alloy is identified to be $(Mg,Zn)_3Gd$ and the bulk sized phases have the ratio close to the I-phase. For 10 Gd alloy, a network shaped continuous phase is seen. The volume of the second phase is increased drastically in 10 Gd alloy compared with other alloys. The EDS results is similar to the composition of $(Mg,Zn)_3Gd$ phase in 3 and 4 Gd alloys. A few small particles containing almost equal amounts of Gd and Zn are also observed. The phases are expected to be $Mg_{12}ZnGd$ (X-phase) from the EDS and XRD analyses [161-163].

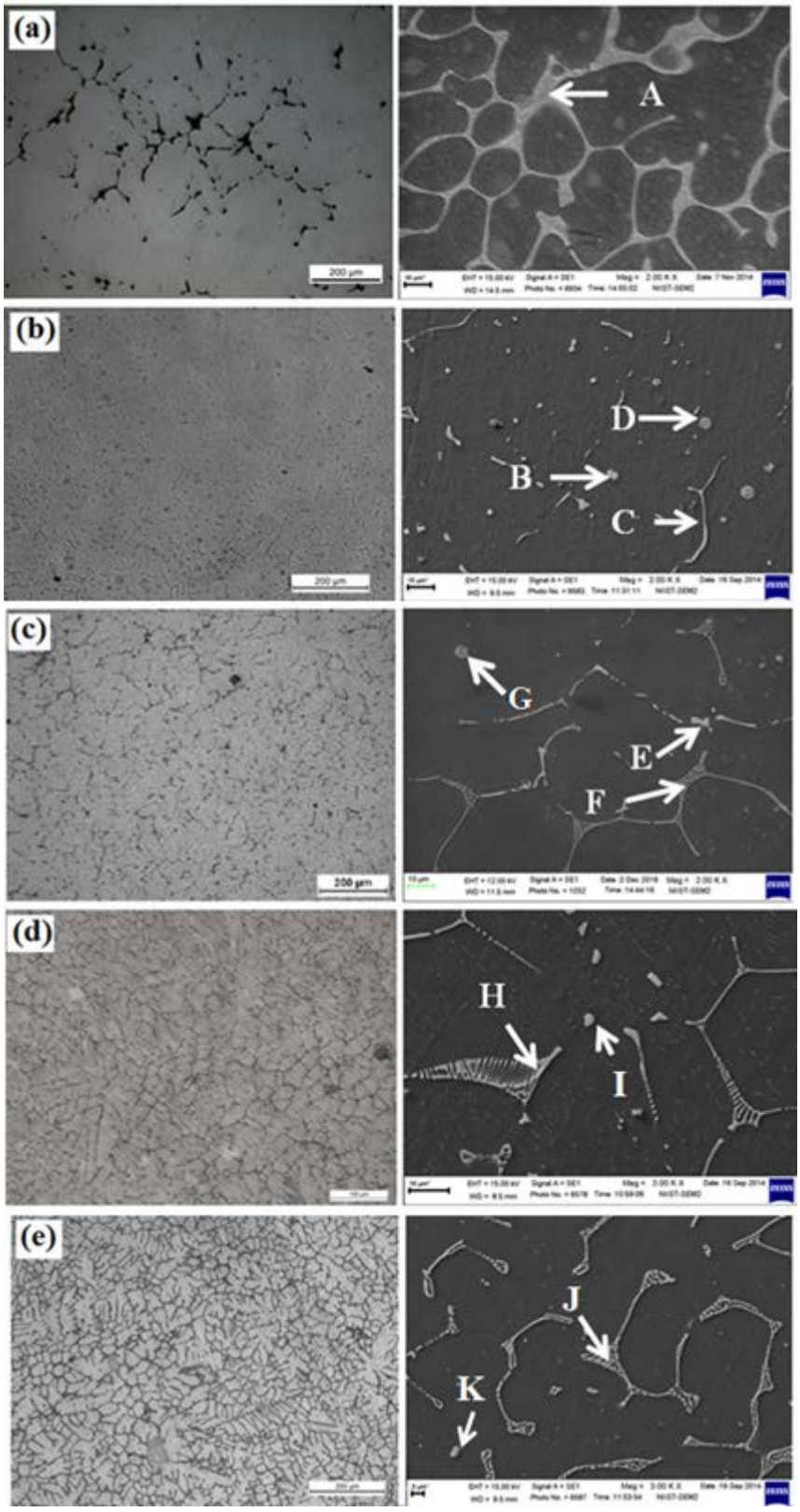

Fig. 4.10 *Optical and SEM microstructures of (a) 0 Gd, (b) 2 Gd, (c) 3 Gd, (d) 4 Gd, and (e) 10 Gd alloys.*

Table. 4.1 *EDS analyses results of the different phases present in the Mg-Zn-Gd alloys.*

Alloy Code		Mg (at.%)	Zn (at.%)	Gd (at.%)	Calculated Phase
0 Gd	**A**	66.39	33.61	-	$MgZn_2$
	B	42.59	48.93	8.48	Mg_3GdZn_6
2 Gd	**C**	54.22	24.74	21.04	$(Mg,Zn)_3Gd$
	D	49.45	25.31	25.24	$(Mg,Zn)_3Gd$
	E	43.6	48.6	7.8	Mg_3GdZn_6
3 Gd	**F**	48.55	29.4	22.05	$(Mg,Zn)_3Gd$
	G	47.62	26.53	25.85	$(Mg,Zn)_3Gd$
	H	53.44	23.21	23.35	$(Mg,Zn)_3Gd$
4 Gd	**I**	44.3	45.75	9.95	Mg_3GdZn_6
	J	52.25	24.64	23.11	$(Mg,Zn)_3Gd$
10 Gd	**K**	81.55	9.17	9.28	$Mg_{12}ZnGd$

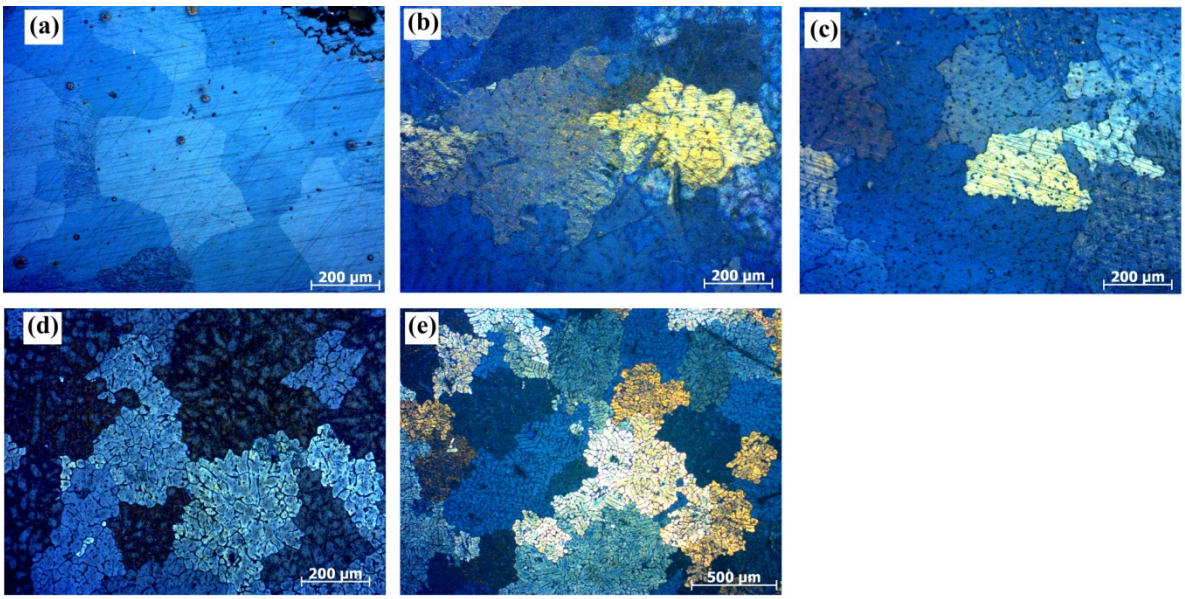

Fig. 4.11 *Grain size of (a) 0 Gd, (b) 2 Gd, (c) 3 Gd, (d) 4 Gd, and (e) 10 Gd alloys.*

In the present study, as expected, different phases are present with different Zn/Gd ratios and it can be said that the volume of secondary phases decreases as the Zn/Gd ratio increases. In addition, among the alloys investigated, the morphology of the $(Mg,Zn)_3Gd$ is different with varying Zn/Gd ratios. For the Mg-Zn system, the

samples are solutionized at 500 ºC for 20 hours and aged at 200 ºC for 1 hour to measure the grain sizes. The average grain size is found to be decreasing till 3 wt.% Gd addition and further addition caused coarsening of the grains. As seen in Fig. 4.11, the average grain size is seen to be around 300, 250, 200, 300 and 500 µm for the 0 Gd, 2 Gd, 3 Gd, 4 Gd, and 10 Gd alloys. The formation of I-phase can effectively restrain the grain growth and the low diffusibility of Gd contributes to suppression of grain growth.

4.5 Mg-Zn-Gd-Ca Alloys

4.5.2 XRD and microstructure analyses

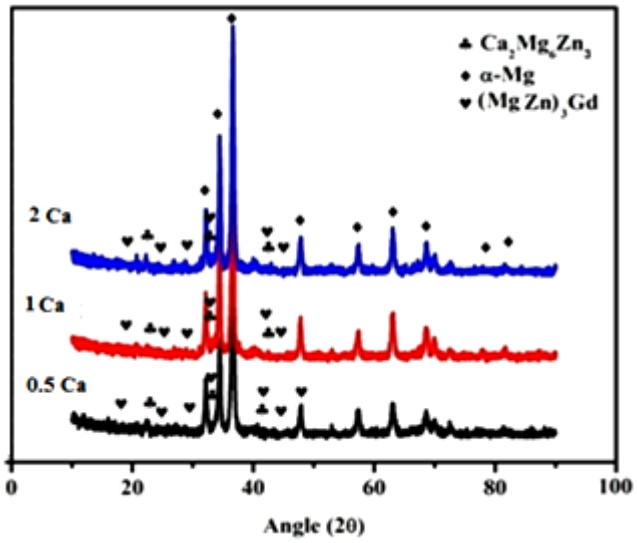

Fig. 4.12 *XRD results of the Mg-Zn-Gd-Ca alloys.*

Fig. 4.12 shows the XRD results of the as-cast experimental alloys. It is observed that the alloys are mainly composed of α-Mg, $(MgZn)_3Gd$ and $Ca_2Mg_6Zn_3$ phases [164-169]. These are further confirmed by the EDS analyses. The optical and SEM images of as-cast Mg-5Zn-3Gd-xCa alloys (0.5, 1 and 2 wt.%) are depicted in Fig. 4.13. For the alloy with 0.5 wt.% Ca, semi continuous precipitates appear both in the interdendritic region and along the grain boundaries, as shown in Fig. 4.13. It is

observed that the volume of precipitates along grain boundaries increases and become more continuous as the Ca content increases above 0.5 wt.%.

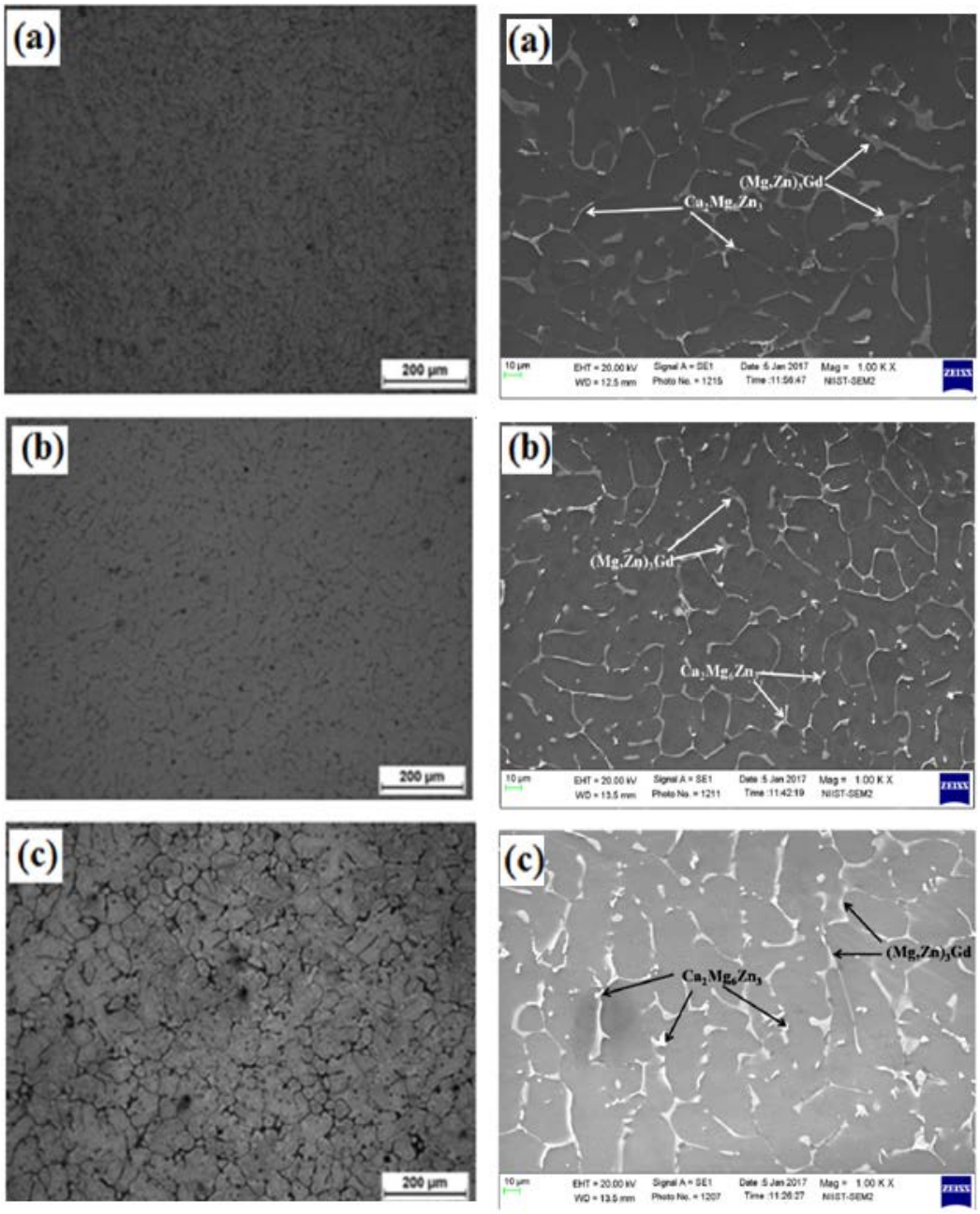

Fig. 4.13 *Optical and SEM microstructures of (a) 0.5 Ca, (b) 1 Ca, and (c) 2 Ca alloys.*

The EDS results (Fig. 4.14) of the different phase formations are given in Table 4.6. It is seen that for 0.5 Ca alloy, the main phases present are W-phase with traces of Ca content and $Ca_2Mg_6Zn_3$. When the Ca addition is increased to 1 wt.% and above, in

addition to the W-phase, the volume fraction of $Ca_2Mg_6Zn_3$ phase increases in both 1 Ca and 2 Ca alloys. The Mg content in W-phase also changes with the increase in Ca content as seen in Table. 4.2 [167-170]. The Mg content in the W-phase is 64.76 at.% as the Ca content is 0.5%, while it decreases to 59.7 at.% and 52.13 at.% as the ca content increases to 1 and 2 wt.% respectively. As the Ca content increases from 0.5 to 2.0 wt.%, the W-phase deceases and the volume of $Ca_2Mg_6Zn_3$ phase increases. The average grain size (Fig 4.15) of the alloys changes from approximately 223 µm to 424 µm and 510 µm respectively. As discussed earlier, the grain size of Mg-5Zn-3Gd alloy was in the range of 200 µm. It is observed that Ca addition will not significantly contribute to reduction in grain size due to the coarsening of $Ca_2Mg_6Zn_3$ particles.

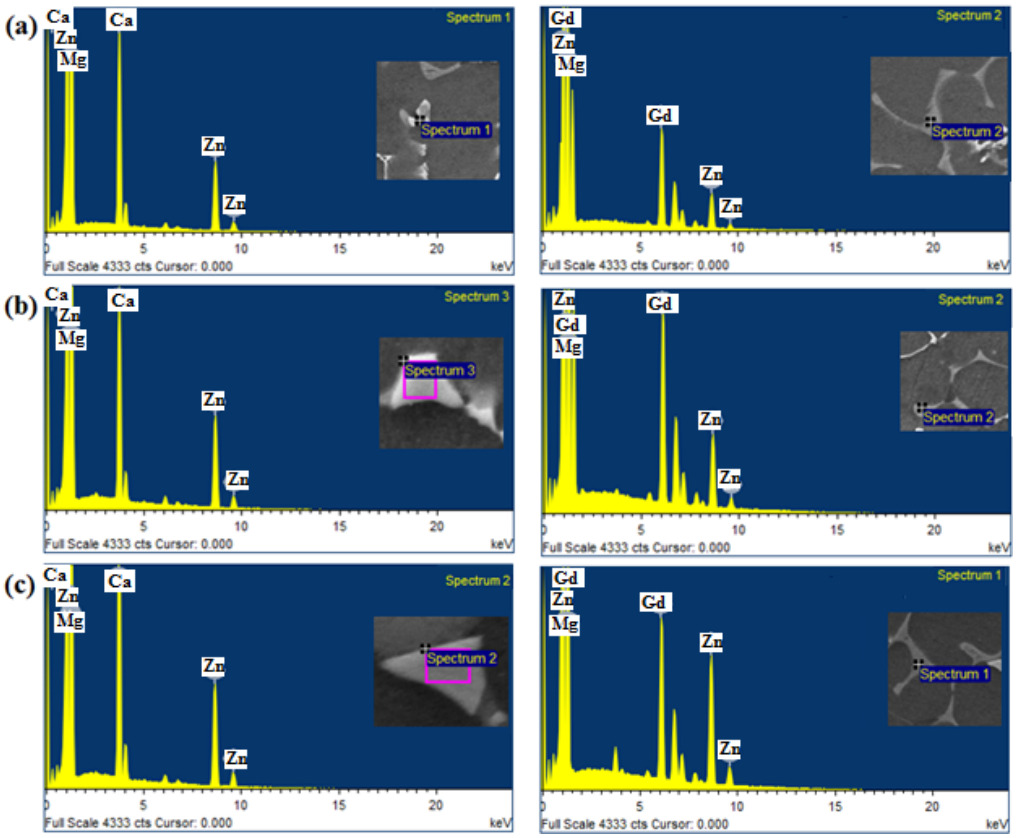

Fig. 4.14 *EDS results of (a) 0.5 Ca, (b) 1 Ca, and (c) 2 Ca alloys.*

Table. 4.2 *EDS analyses results of the different phases present in the Mg-Zn-Gd-Ca alloys.*

Alloy Code	Mg (at.%)	Zn (at.%)	Gd (at.%)	Ca (at.%)	Calculated phase
0.5 Ca	73.55	15.44		11.01	$Ca_2Mg_6Zn_3$
	64.76	17.19	16.63	1.42	$(Mg,Zn)_3Gd$
1 Ca	81.47	10.95		7.58	$Ca_2Mg_6Zn_3$
	59.70	20.38	18.92	1.30	$(Mg,Zn)_3Gd$
2 Ca	76.12	13.66		10.22	$Ca_2Mg_6Zn_3$
	52.13	22.31	23.54	2.02	$(Mg,Zn)_3Gd$

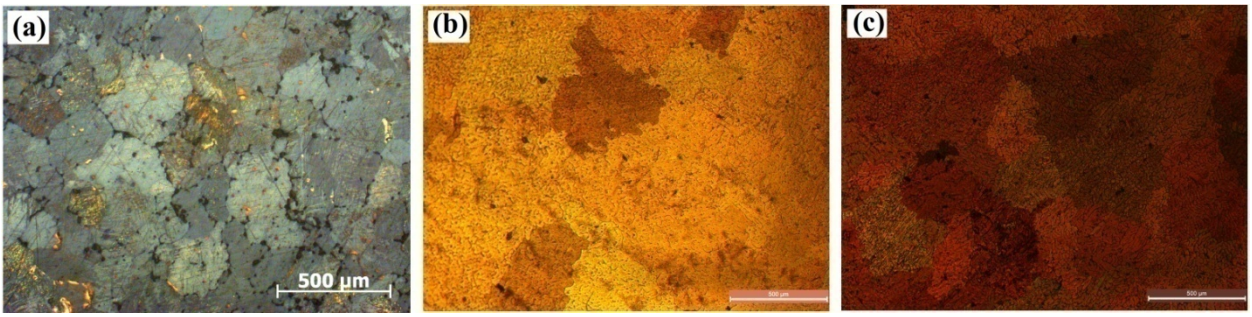

Fig. 4.15 *Grain size of (a) 0.5 Ca, (b) 1 Ca, and (c) 2 Ca alloys.*

4.6 Conclusions

From the present study, it is understood that the addition of rare earth element Gd and Ca has significant effect on the microstructures of the Mg-Al and Mg-Zn alloys. The main conclusions are as follows.

- When Gd is added in varying wt percentages to Mg-Al alloy, a thermally stable Al_2Gd phase is formed in the matrix and the $Mg_{17}Al_{12}$ phase is found to be refined.
- When Ca is added to Mg-Al-Gd alloys, the Ca atoms are incorporated into the β- $Mg_{17}Al_{12}$ phases and in addition to Al_2Gd phases, Al_2Ca phases are formed above 1 wt.% Ca addition. The grain size is found to be decreased till 1 wt.% Ca content.

- Microstructures of Mg-Zn-Gd alloys varied with Zn/Gd ratio. It is observed that as the Zn/Gd ratio increases, volume of secondary phases decreases. When the Zn/Gd ratio is in the tested range of 7-3, the main phases present in the alloys are $(Mg,Zn)_3Gd$ and Mg_3Zn_6Gd. It is observed that the continuity and volume fraction of $(Mg,Zn)_3Gd$ phase increases with increase in Gd content. In addition to the $(Mg,Zn)_3Gd$ phase, $Mg_{12}ZnGd$ phase is formed when the Zn/Gd ratio is decreased to 1. It is seen that the morphology of $(Mg,Zn)_3Gd$ phase becomes more continuous with decrease in Zn/Gd ratio.
- With increasing Ca content to Mg-Zn-Gd alloys, the volume of W-phase decreases and the $Ca_2Mg_6Zn_3$ phase increases. The grain size is found to be increased with increase in Ca content.

Chapter 5 Mechanical Properties of the Developed Alloys

5.1 Introduction

The mechanical properties evaluation of the Gd and Ca added Mg-Al and Mg-Zn alloys are discussed in this chapter. The mechanical properties such as macro hardness, room and high temperature (150 °C) tensile properties (UTS, YS and % Elon) of the developed alloys are evaluated and correlated with microstructures.

5.2 Mg-Al-Gd Alloys

Table 5.1 *Mechanical properties of the Mg-Al-Gd alloys.*

Alloy Code	Hardness (BHN)	RT			HT (150 °C)		
		UTS (MPa)	YS (MPa)	Elon (%)	UTS (MPa)	YS (MPa)	Elon (%)
0 Gd	50.1 (±1.5)	165.21 (±13.52)	84.61 (±14.57)	4.0 (±0.1)	115.87 (±5.68)	58.10 (±7.75)	5.5 (±0.4)
0.5 Gd	53.9 (±2.8)	179.33 (±12.34)	96.22 (±12.23)	4.2 (±0.2)	143.44 (±10.67)	65.22 (±9.43)	5.6 (±0.3)
1 Gd	60.3 (±1.2)	187.75 (±13.31)	112.42 (±9.65)	4.3 (±0.5)	152.02 (±3.43)	69.32 (±5.21)	5.9 (±0.4)
2 Gd	66.2 (±1.6)	210.03 (±10.73)	116.21 (7.17)	4.6 (±0.7)	159.34 (±9.49)	74.22 (±5.53)	6.4 (±0.5)

The mechanical properties of as-cast Mg–9Al–xGd alloys at RT and 150 °C are presented in Table 5.1. Addition of Gd yields significant beneficial effects on the mechanical properties. The lattice constant of Gd is very similar to that of Mg. The lattice constants of Gd and Mg are a = 0.36360 and c = 0.57826 nm, and a = 0.32094 and c = 0.52104 nm respectively. Due to size difference between Gd (0.233 nm) and Mg (0.162 nm) atoms, Gd is difficult to solid solute in Mg alloy, but tends to form rare

earth compounds. It is seen that by the Gd addition, the hardness value of alloy increases from 50.1 BHN, and the highest value of 66.2 BHN is obtained for 2 Gd alloy. Moreover, the hardness of alloys are increased by increasing the percentage of Gd addition, mainly due to increase in the volume of Al_2Gd phase and the Gd dissolution into the matrix. Moderate improvement in UTS (8%) and YS (12%) are noticed with 0.5 wt.% Gd added alloy can be attributed to solid solution strengthening and reduction in the stress concentration by refining the microstructure [8,77,141,171]. The 2 Gd alloy at room temperature shows 27% and 36% increase of UTS and YS respectively compared to 0 Gd alloy due to the formation of Al_2Gd phase which restricts the dislocation movement and grain boundary sliding [171-177]. The strength of the grain boundary is greater than the strength of the grain at room temperature. During tensile deformation, the dislocations move inside the grain until they reach the grain boundary, where the motion is opposed. More dislocations get piled up as a cluster at the boundaries thereby generating a repulsive stress field. Then the dislocations apply the driving repulsive force to reduce the energy for dislocation diffusing across the boundary. The higher the repulsive stress applied to move the dislocation, the higher the yield strength would be [178]. So, a decrease in the grain size favors the increment of yield strength. The average grain size is seen to be around 200, 140, 120, and 100 μm for the 0 Gd, 0.5 Gd, 1 Gd and 2 Gd alloys respectively (Fig. 4.4). At 150 °C, the maximum strength values (UTS & YS) are obtained for 2 Gd alloy (159.34 and 74.22 MPa, respectively). In 0.5 Gd alloy, $Mg_{17}Al_{12}$ is the main strengthening phase, which has a low melting point of 462 °C and has poor thermal stability. The $Mg_{17}Al_{12}$ phase can readily coarsen and soften at the temperatures above 120 °C. The cubic crystal structure of $Mg_{17}Al_{12}$ is incoherent with the h.c.p. magnesium matrix, leading to the fragility of Mg: $Mg_{17}Al_{12}$ interface. All of the above lead to the

poor high temperature tensile properties of Mg–9Al alloys at 150 °C [179,180]. It is observed that the addition of Gd helps in improving the strength at 150 °C. The maximum strength values obtained for 2 Gd alloy is possibly due to the formation of thermally stable intermetallic Al_2Gd precipitates. At higher temperatures, the strength of the grain boundaries are weak compared to the strength of the grains and fine-grain strengthening would be less effective but they do serve as an obstacle during dislocation motion. The presence of thermally stable Al_2Gd particles restrict the dislocation motion and increase the alloy density both at room and high temperatures. More Al_2Gd dispersion yields higher tensile and yield strengths [181].

5.3 Mg-Al-Gd-Ca Alloys

Table 5.2 *Mechanical properties of the Mg-Al-Gd-Ca alloys.*

Alloy Code	Hardness (BHN)	RT			HT (150 °C)		
		UTS (MPa)	YS (MPa)	Elon (%)	UTS (MPa)	YS (MPa)	Elon (%)
0 Ca	66.2 (±1.6)	210.03 (±10.73)	116.21 (7.17)	4.6 (±0.7)	159.34 (±9.49)	74.22 (±5.53)	6.4 (±0.5)
0.5 Ca	69.4 (±1.7)	224.33 (±11.31)	129.05 (±6.23)	4.8 (±0.4)	174.16 (±9.49)	91.27 (±5.75)	5.7 (±0.3)
1 Ca	78.1 (±1.5)	236.45 (±4.52)	140.11 (5.23)	5.4 (±0.5)	186.07 (±9.49)	99.74 (±5.35)	5.8 (±0.4)
2 Ca	71.6 (±1.1)	220.63 (±5.25)	115.53 (±6.42)	4.7 (±0.4)	172.04 (±7.43)	76.82 (±3.52)	5.2 (±0.2)

The influences of Ca addition on the mechanical properties of Mg-9Al-2Gd are given in Table 5.2. Compared to the base Mg-9Al-2Gd (0 Ca) alloy, at room and high temperatures, the ultimate tensile strength and yield strength of 1 wt.% Ca added alloy are significantly increased. The Gd dissolution into α-Mg matrix plays the role of solid solution strengthening, while Al-Gd compounds formed in the matrix and at grain

boundaries effectively prohibit the growth of grains and the dislocation movement, thus giving enhanced mechanical properties. The 0.5 wt.% Ca addition refined the $Mg_{17}Al_{12}$ phase and increase in Ca content above 1 wt.% leads to the formation of a reticular $Mg_{17}Al_{12}$ phase. By increasing Ca upto 1 wt.%, the ultimate tensile strength, yield strength and elongation of the alloys are found to be increased. The solid solubility limit of Ca in magnesium is around 0.43 at.% at 517 °C and the further Ca addition leads to the formation of Al_2Ca phase along grain boundaries, resulting in the improvement of ultimate tensile strength and elongation [182]. The grain size of Mg-Al-Gd-Ca alloy (Fig. 4.8) are seen to be decreasing till 1 wt.% Ca addition, thereby enhancing the grain boundary strength and in the improvement of YS. Compared to the 0 Ca and 0.5 Ca alloys, the presence of Al_2Ca phase attributes to the increment in strength of 1 Ca alloy. The presence of coarse Al_2Ca particles would reduce alloy strength and ductility in the alloys. Although the formation of phases like Al_2Ca and Al_2Gd increases the thermal stability of the alloy, the presence of $Mg_{17}Al_{12}$ partly impairs it. The bcc β-$Mg_{17}Al_{12}$ phase being incoherent with the hcp α-Mg matrix is also a limiting factor in strengthening. At high temperatures, the decomposition of Al_2Ca is more difficult than that of $Mg_{17}Al_{12}$. This Al_2Ca phase is capable of effectively blocking the movement of the dislocations and the sliding of the grain boundaries, and thus increasing the high-temperature stability of the materials. It can be deduced that Ca has two distinct effects on the mechanical properties of materials; one is the enhancement of hardness and strength and the other one is the retention of these properties after exposure to high temperature. It is well accepted that, according to the Hall–Petch relationship, the strength and hardness both increase as the size of the microstructural elements decreases. Particle hardening and solid solution hardening caused by the dissolution of Ca atoms in the matrix and second phase particles

promotes the hardness and strength of the Ca-containing alloys. The slightly reduced strength of the alloys with higher percentage of Ca, however, could be due to the grain growth and disintegration of the Al_2Ca phase as a result of exposure to high temperatures and reduction in grain boundary coverage by this phase. So, it can be concluded that the role of Al_2Ca phase is ambivalent: strengthening and weakening can be observed. The Al_2Ca particles being relatively small, strengthening is found to be predominant till 1 wt.% Ca addition.

5.3.1 Creep properties

Table 5.3 *Creep properties of the selected Mg-Al-Gd-Ca alloys.*

Alloy Code	Min Creep Rate (/sec)	Time (Hours)
0 Gd	2.94×10^{-7}	56
2 Gd	9.6×10^{-9}	289
1 Ca	1.50×10^{-9}	553

Out of various developed Mg-Al alloys, the Mg-9Al, Mg-9Al-2Gd and Mg-9Al-2Gd-1Ca alloys are selected to study the creep properties. Table 5.3 illustrates the minimum creep rate of alloys at 150 ºC with an initial stress of 50 MPa. Mg-9Al-2Gd-1Ca exhibits the lowest creep rate among the investigated alloys. As discussed earlier, the presence of Al_2Gd and Al_2Ca intermetallic in Mg-9Al-2Gd-1Ca alloy effectively creates back stress that slow down the dislocation movement. The higher thermal stability of Al_2Gd and Al_2Ca phase restricts the softening and coarsening at elevated temperature which resulted in better creep resistance. The existence of high melting point phases offered high thermal and structural stability to the alloys; hence the deformation at elevated temperature was limited. In addition, diffusion of elements also

contributed to the coarsening of the intermetallics during creep. For instance, Al has high diffusivity in Mg matrix at high temperatures that contributes to the poor creep resistance of Mg-Al alloys. However, the addition of Gd and Ca reduced the amount of Al available to diffuse by forming thermally stable phases. In general, the high creep properties of Mg-9Al-2Gd-1Ca could be attributed to the higher melting point intermetallics.

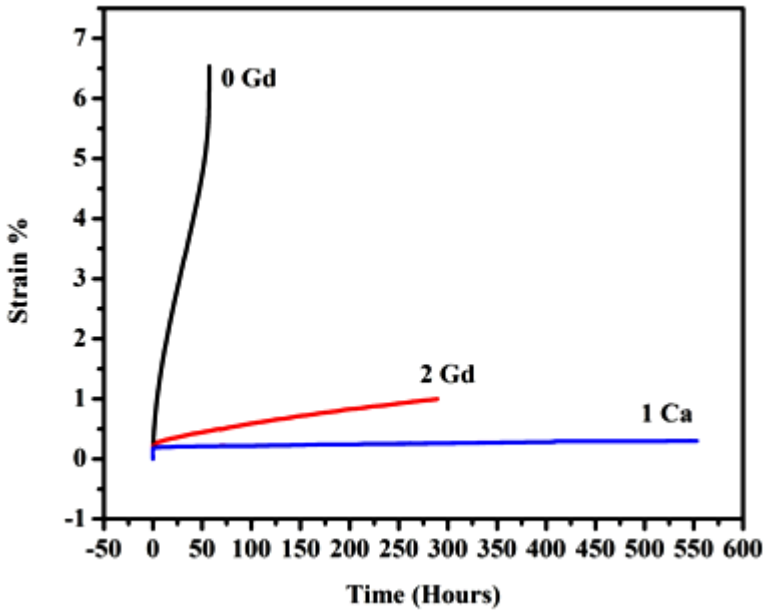

Fig. 5.1 *Creep curve of 0 Gd, 0.5 Gd, and 1 Ca alloys.*

5.4 Mg-Zn-Gd Alloys

Table 5.4 shows the related mechanical properties of the alloys at room temperature as well as at elevated temperatures. It shows that addition of Gd can notably increase the YS of the alloy, but after a certain limit the YS values are found to be decreasing with increasing Gd content. The highest strength level is obtained in 3 Gd alloy, and the UTS and YS are 212 MPa and 102 MPa respectively. This is attributed to the volume fraction of second phases and the presence of Mg_3Zn_6Gd phase (I-phase). The I-phase with its quasiperiodic lattice leads to coherent interface with Mg matrix [133]. Due to the coherent interface, I-phase particles are stable against moving and

coarsening. Therefore, the I-phase particles can effectively obstruct dislocations slipping and so significantly strengthen the alloy. Earlier works on Mg–Zn–Y alloy show that the mechanical property is seen to degrade greatly with the increasing volume fraction of the W-phase. The interface between the cubic structured W-phase and the Mg matrix is incoherent and thus weak. Pile up of dislocations at the interface leads to the initiation of crack and easy propagation along the interface [183-186]. This reduces both UTS and ductility. The $(Mg,Zn)_3Gd$ phase observed here is similar to the W-phase. Additionally, it is seen that the $Mg,Zn)_3Gd$ phase (W-phase) and $Mg_{12}ZnGd$ phase (X-phase) formations increase and become more continuous with increasing Gd and these are known to deteriorate the mechanical properties due to their coarseness and their location on grain boundaries. This is another reason for the decrease in strength with increasing Gd after 3 wt.%. Hence, it can be said that the I-phase particles found in the microstructure contributed to the improvement in strength. Low interface energy and quasi-periodic lattice structure make the I-phase to have good bonding properties with matrix. The high symmetry make I-phase isotropic in nature, thereby imparting better plastic compatibility with matrix during deformation and the activity of non-basal slip systems, thus I-phase dispersing in grain boundary would largely improved deformation capability of 3 Gd alloy. Higher mechanical properties would have been obtained, if the I-phase was finer in size and distributed uniformly throughout the matrix. To obtain good particle strengthening at the grain boundary, the interface between the particle and the matrix should be coherent. Hence the weak interface between $(Mg,Zn)_3Gd$ phase and the α-Mg matrix in these alloys significantly lowers the elongations in Gd added alloys compared to 0 Gd alloy. With the increasing $(Mg,Zn)_3Gd$ phase, the interface becomes weaker. Thus, the strength of the alloys decreases with increasing Gd after 3 wt.%. The reason for low elongation for the alloy

containing large number of intermetallic particles can be the same case of Mg-Zn-Y alloys, where the low elongation was due to formation of geometrically necessary dislocations were surrounding the secondary particles, eventuating in decohesion from the matrix [162]. According to the well-known Hall-Petch relation, grain refinement has an effect on the increase of yield strength. The average grain size (Fig. 4.11) is found to be decreasing till 3 wt.% Gd addition and further addition caused coarsening of the grains. Gd is a surface active element and can easily segregate at the liquid–solid interface or get absorbed onto the growth front [128]. It can then change both the solid–liquid interfacial energy and surface energy of the crystal, thereby poisoning the growth steps possibly resulting in grain refinement. As the test temperature increased to 150 °C, the YS, UTS reduced significantly and the elongation to failure increased correspondingly.

Table. 5.4 *Mechanical properties of the Mg-Zn-Gd alloys.*

		RT			HT (150 °C)		
Alloy Code	**Hardness (BHN)**	**UTS (MPa)**	**YS (MPa)**	**Elon (%)**	**UTS (MPa)**	**YS (MPa)**	**Elon (%)**
0 Gd	51.3 (±1.6)	155.22 (±11.12)	91.58 (±5.62)	6.1 (±0.2)	121.34 (±12.22)	68.06 (±5.13)	6.5 (±0.3)
2 Gd	62.1 (±2.3)	189.54 (±15.26)	94.66 (±12.04)	5.6 (±0.1)	142.87 (±10.06)	84.24 (±10.72)	6.1 (±0.5)
3 Gd	65.4 (±1.5)	212.16 (±10.77)	102.22 (±7.52)	4.6 (±0.1)	155.34 (±11.41)	98.02 (±3.42)	5.4 (±0.1)
4 Gd	66.3 (±1.3)	192.66 (±13.42)	91.68 (±10.50)	4.4 (±0.3)	132.45 (±8.07)	67.40 (±11.58)	5.4 (±0.1)
10 Gd	70.7 (±2.4)	154.41 (±9.54)	81.57 (±6.22)	3.2 (±0.1)	123.92 (±6.09)	61.76 (±7.61)	5.2 (±0.2)

5.5 Mg-Zn-Gd-Ca Alloys

The mechanical properties at room temperature and high temperature (150 °C) including hardness and tensile properties are listed in Table. 5.5. It is seen that, within the tested range, the highest properties are obtained for the Mg-5Zn-3Gd (0 Ca) alloy and the addition of Ca is found to be detrimental to the tensile properties of the alloys. As mentioned earlier, the addition of Ca decreases the amount of $(Mg,Zn)_3Gd$ along grain boundaries, which may lead to decrease in YS and improvement in elongation [167,187].

Table. 5.5 *Mechanical properties of the Mg-Zn-Gd-Ca alloys.*

		RT			HT (150 °C)		
Alloy Code	**Hardness (BHN)**	**UTS (MPa)**	**YS (MPa)**	**Elon (%)**	**UTS (MPa)**	**YS (MPa)**	**Elon (%)**
0 Ca	65.4 (±1.5)	212.16 (±10.77)	102.22 (±7.52)	4.6 (±0.1)	155.34 (±11.41)	98.02 (±3.42)	5.4 (±0.1)
0.5 Ca	66.4 (±2.4)	198.61 (±10.22)	95.24 (±9.20)	5.1 (±0.5)	157.18 (±6.33)	89.53 (±5.47)	5.8 (±0.2)
1 Ca	68.3 (±1.3)	177.16 (±11.04)	90.67 (±13.71)	5.7 (±0.2)	142.44 (±14.57)	84.11 (±5.88)	6.3 (±0.2)
2 Ca	72.2 (±1.8)	164.77 (±14.20)	81.45 (±7.25)	5.9 (±0.3)	121.68 (±11.60)	71.06 (±8.04)	6.5 (±0.3)

As the Ca content is increased beyond 0.5 wt.%, the volume of $Ca_2Mg_6Zn_3$ increases and mainly distribute along the grain boundaries. Among the Ca added alloys, 0.5 wt.% Ca alloy yields relatively high tensile properties, which is possibly due to the difference in the size and distribution of the $(Mg\ Zn)_3Gd$ phases along the grain boundaries. It is well known that fine, uniform phases along the grain boundaries act as an obstacle to dislocation motion thereby enhancing the mechanical properties [188,190]. It is seen that as the volume fraction of $Ca_2Mg_6Zn_3$ phases increase with

increase in Ca content and the tensile properties are found to decline. The grain size of the developed alloys (Fig. 4.15) are increased after 0.5% Ca addition, and the large $Ca_2Mg_6Zn_3$ phases and cannot effectively restrict the grain growth and detoriates the properties [191]. Therefore, the hindering effect of coarse secondary phase on grain growth is weakened, thereby resulting in grain coarsening and the YS value decreases. So, to design Mg-Zn-Gd alloys with Ca additions for high properties, the aim should be to reduce the $Ca_2Mg_6Zn_3$ content.

5.6 Conclusions

From the present study, it is understood that the addition of rare earth element Gd has a positive effect on the mechanical properties of the Mg-Al and Mg-Zn alloy systems. The main conclusions are as follows:

- The hardness of the Gd-containing Mg-Al alloys is evidently improved by the Gd addition and the maximum hardness of 66.2 BHN is obtained with 2 wt.% Gd addition.
- The tensile properties of the Mg-Al alloys alloys are enhanced by the Gd addition both at room and high temperature and the optimum combination of properties are obtained with 2 wt.% Gd, which is attributed due to the presence of thermally stable intermetallic Al_2Gd precipitates at the grain boundaries which effectively suppress the dislocation motion and grain boundary sliding.
- The hardness of the Ca containing Mg-Al-Gd alloys are evidently improved and the maximum hardness of 78.1 BHN is obtained with 1.0 wt.% Ca addition.
- The ultimate tensile strength and yield strength of 1 wt.% Ca addition in Mg-Al-Gd alloys are significantly increased due to the presence of Al_2Gd and Al_2Ca phases at the grain boundaries which effectively suppress the dislocation motion and grain boundary sliding.

- Mg-5Zn-3Gd alloy exhibited higher UTS, YS at RT as well as at high temperatures (150 °C), due to the presence of Mg_3Zn_6Gd (I-phase), which effectively strengthened the material. However, the elongation was poor due to the brittle and coarse $(Mg,Zn)_3Gd$ phase at the boundaries. Due to the lower volume of Mg_3Zn_6Gd phases and continuous $(Mg,Zn)_3Gd$ phase, alloys with Gd content greater than 3 wt.% showed lesser strength properties compared to that of Mg-5Zn-3Gd alloy. The beneficial effect of I-phase on the tensile properties were not fully achieved in Mg–5Zn–3Gd, as most of the I-phase particles were bulk in the as cast condition.
- With increasing Ca content to Mg-Zn-Gd alloys, the UTS and YS of the as-cast alloys decrease and an improvement in % Elon is observed which is due to decline in the volume fraction of the $(Mg,Zn)_3Gd$ phase.

Chapter 6 Corrosion & Wear Behavior of the Developed Alloys

6.1 Introduction

Detailed corrosion (immersion and electrochemical tests) and wear properties of the developed Mg-Al and Mg-Zn alloy systems are discussed in this chapter. All the corrosion tests are done at room temperature in 3.5 wt.% NaCl solution. Dry sliding wear experiments were carried out using the pin-on-disc wear testing machine operated under the normal loads of 10, 20, 30, 40 and 50 N. The wear rates at constant sliding speed (2 m/s) have been estimated and analyzed. Furthermore, wear surface of each wear-tested sample have been examined. The corrosion and wear properties are correlated with the respective microstructures.

6.2 Corrosion Properties

6.2.1 Mg-Al-Gd Alloys

6.2.1.1 Electrochemical test

The potentiodynamic polarization behavior of the developed alloys are depicted in Fig. 6.1(a) and the polarization features such as i_{corr} and E_{corr} of the alloys, measured from polarization curves are presented in Table **6.1.**

Table 6.1 *Electrochemical results of the Mg-Al-Gd alloys.*

	0 Gd	0.5 Gd	1 Gd	2 Gd
i_{corr} (mA/cm^2)	1.535 (±0.031)	0.275 (±0.021)	0.102 (±0.042)	0.085 (±0.004)
E_{corr} (V)	-1.565 (±0.024)	-1.556 (±0.033)	-1.560 (±0.010)	-1.530 (±0.036)

The E_{corr} values of the investigated alloys varied between -1.565 V and -1.530 V. It is seen that the Gd additions have shifted the cathodic portion of the curves

towards lower current densities. The corrosion current is an actual measure of corrosion rate, representing the material's corrosion behavior in a greater degree. The current density values are seen to decrease with increase in the amount of Gd addition suggesting that the increase in corrosion resistance. It is noticed from Table 6.1 that the corrosion current densities (i_{corr}) of the alloys with Gd addition is lower than that of the 0 Gd alloy with appreciable reduction for 2 Gd alloy which is two order magnitude lower than that of 0 Gd alloy implying that the 2 Gd alloy has highest corrosion resistance. The corrosion process of Mg-Al alloys in NaCl solution undergoes two main reactions. One is the anodic dissolution reaction and the cathodic hydrogen evolution reaction [176]. The reaction equations are listed in Equations (3-7).

Anodic Reaction: $Mg \rightarrow Mg^{2+} + 2e^{-}$ **(1)**

$Al \rightarrow Al^{3+} + 3e^{-}$ **(2)**

Cathodic Reaction: $2H_2O + 2e^{-} \rightarrow H_2\uparrow + 2OH^{-}$ **(3)**

Corrosion Product: $Mg^{2+} + 2OH^{-} \rightarrow Mg(OH)_2\downarrow$ **(4)**

$Al_3^{+} + 3OH^{-} \rightarrow Al(OH)_3\downarrow$ **(5)**

The electrochemical results indicate that Gd is effective in enhancing the corrosion resistance of Mg-Al intermetallic alloys by suppressing the hydrogen evolution. Grain boundaries play an important role in affecting the alloy's corrosion resistance. Some investigations show that the secondary phases at grain boundaries act as the hindrance for corrosion, thereby attributing to better corrosion resistance [192,193]. When the Gd content reaches to 2 wt.%, the grain size is smaller compared to the other alloys imparting the best corrosion resistance. The variations in corrosion current with the addition of gadolinium due to the reduction of $Mg_{17}Al_{12}$ or compositional homogenization. The $Mg_{17}Al_{12}$ precipitates act as microcathodes, causing internal galvanic corrosion thereby accelerating the corrosion process [175].

When gadolinium is added, the Al present in the alloys are utilized to form Al-Gd phases thereby lowering the Al content available to form $Mg_{17}Al_{12}$ precipitates. It has been validated that the potential difference between $Mg_{17}Al_{12}$ and the α phase, is relatively larger than the potential difference between Al_2Y and α phase [194]. Similarly, the micro-galvanic cathode caused by the potential difference will be weakened with Al_2Gd gradually replacing $Mg_{17}Al_{12}$. Eventhough the Al_2Gd acts as the main corrosion resisting phase, it also acts as cathode, inducing galvanic effects, because the Al_2Gd surrounding Mg matrix gets preferentially dissolved suggesting the cathodic nature of the same relative to the Mg matrix [6,68,175,176]. But the additions upto 2% do not produce many such micro-electrodes and results in corrosion resistance.

The electrochemical impedance spectroscopy (EIS) behavior of the studied samples is represented as Nyquist plot and the simulated fittings are presented in Fig. 6.1(b) and found to be well fitted with the experimental spectra. The diameter of the capacitive semicircle in nyquist plot is highly associated with corrosion resistance; larger diameter implies higher corrosion resistance [72]. Among the studied alloys, 2 Gd alloy exhibited a larger diameter whereas, 0 Gd alloy showed the lowest diameter indicating that corrosion resistance of alloys increased with increase in Gd content. The fitted EIS values of the experimental alloys are summarized in Table 6.2. In the equivalent circuit (Fig. 6.1(c), R_s represent the solution resistance between the reference electrode and specimen. A constant phase element (CPE), usually represented as Q, is an equivalent electrical circuit component that models the behavior of a double layer that is an imperfect capacitor. Q_1 and Q_2 represent the two constant phase elements which are used to obtain a good fit, considering the inhomogeneous reaction rates at the electrode surface, electrode surface roughness, varying thickness and non-uniform current distribution during corrosion [195]. R_1 and R_2 are the respective resistance

elements corresponding to Q_1 and Q_2. The R_1 values of the samples (in the high frequency domain) are increased in the following order: 0 Gd < 0.5 Gd < 1 Gd alloy < 2 Gd. Among the studied alloys, 2 Gd alloy showed the highest resistance indicating its increased corrosion resistance. The Q value is related to corrosion reaction area i.e. low Q value implies that relatively low area of the exposed surface is corroded. The fitted values of Q shows continuous decrease in the following order: 0 Gd > 0.5 Gd > 1 Gd alloy > 2 Gd. The thin layer of oxide due to the interaction of alloy surface with air and the corrosion product formed during the corrosion acted as a protective cover to the surface in the NaCl solution to some extent. Similar values of Q obtained with all the tested alloys indicated that the protection offered by the corrosion product was similar.

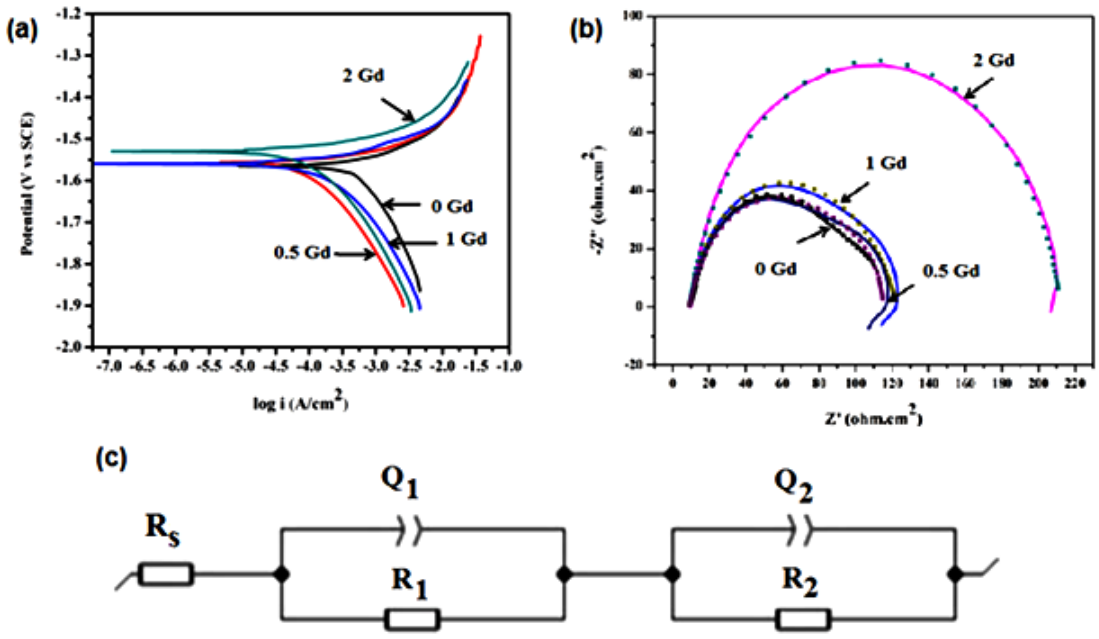

Fig. 6.1 *(a) Tafel plot, (b) Nyquist plot, and (c) Equivalent circuit model of the Mg-Al-Gd alloys.*

In general, for bare substrates, the high frequency capacitive loop represents the formation of oxides or hydroxides at the metal-solution interface as the result of corrosion occurring during the test. The values of 'n' for all the alloys are close to unity, indicating a capacitance behavior. However, the deviation observed in the 'n'

values is normally due to non-uniform current distribution. The presence of inductive loop indicates the occurrence of pitting corrosion in the samples.

Table 6.2 *The fitted EIS values of the Mg-Al-Gd alloys.*

	0 Gd	0.5 Gd	1 Gd	2 Gd
R_s ($\Omega.cm^2$)	9.467	9.356	9.714	9.549
Q_1 ($s^n/\Omega.cm^2$)	54.16×10^{-6}	35.06×10^{-6}	26.27×10^{-6}	22.17×10^{-6}
n_1	0.9656	0.7833	0.8696	0.9662
R_1 ($\Omega.cm^2$)	65.49	79.42	82.66	180.2
Q_2 ($s^n/\Omega.cm^2$)	45.64×10^{-6}	37.21×10^{-6}	34.26×10^{-6}	23.06×10^{-6}
n_2	0.8909	0.8956	0.9745	0.8868
R_2 ($\Omega.cm^2$)	33.41	39.83	42.83	50.72

6.2.1.2 Immersion test

To substantiate the electrochemical results, immersion tests were carried out by immersing all the alloys in 3.5 wt.% NaCl solution for 72 hours. Fig. 6.2 shows the macro images of corroded samples of developed alloys for varying time of 6, 24, 48 and 72 hours. With increasing immersion time, the Gd added alloys are seen to be less corroded. The surface becomes covered with loose white corrosion products which is assumed to be $Mg(OH)_2$. The corrosion initiation in the various developed alloys can be clearly seen after 6 hours of immersion. Corrosion initiates from the edges in all samples due to irregularity and the sharp edge. After 24 hours, the 0 Gd alloy shows pitting and uniform corrosion and almost 70% of the area is corroded. For 0.5 and 1 Gd alloys, localized pitting corrosion is seen at almost 40% and 20% of the exposed area respectively. For 2 Gd alloy, the initiation of corrosion can be seen which is much less when compared to the base alloy. After 48 hours, increased pitting corrosion is noticed for all the alloys. It is seen that the corrosion behavior of 0.5 and 1 Gd alloys are almost

similar in nature. After 72 hours, the metallic luster of 0 Gd alloy is completely lost while 0.5 and 1 Gd alloys show similar uniform pitting corrosion throughout the surface. From Fig. 6.2, under the same test conditions, the metallic luster is quite retained in 2 Gd alloy and suffered less corrosion compared to the other alloys, which may be due to a more uniform and compact corrosion product film formation. The main corrosion form of magnesium alloy is usually pitting corrosion, and from the thermodynamics theory, due to different corrosion potentials, the polarization effect of β phase influences the α phase thereby increasing the corrosion rate of α phase and hence corrosion pits are easily formed in the α phase [192,193]. With the addition of Gd, the corrosion potential moves to negative direction and due to the atomic size difference between Gd and Mg atoms, Gd becomes difficult to solid-solute in magnesium alloy and forms rare earth compounds. Another effect of Gd addition is grain refinement which reduces the micro-galvanic effect. Gd also acts as a purifying element, by removing the impurities in the alloy and hence the corrosion resistance of magnesium alloys are enhanced [192-194]. The gap in between the β phases is large in 0 Gd alloy compared to the other alloys and is not effectively blocked by the corrosive products formed between β and α phase resulting in pits and increased corrosion rate. Smaller sized grain and the narrow gap between precipitates in 2 Gd alloy improve the passive film thereby inhibiting anodic dissolution, and prevents the occurrence of pits.

Fig. 6.3(a) depicts the variation of corrosion rate (mm/year) of experimental alloys as a function of immersion time in 3.5 wt.% NaCl solution. It is seen that the corrosion rate of all alloys increase with respect to immersion time. In the case of Gd added alloys, the corrosion rate is minimal especially in the case of 2 Gd alloy compared to the base alloy which indicates the positive effect of Gd addition.

From the XRD results (Fig. 6.3(b)), it is observed that various hydroxide and oxide layers like $Mg(OH)_2$, $Al(OH)_3$, Al_2O_3 and Gd_2O_3 seems to have developed after the immersion test. It is suggested that adding RE to Mg alloys may improve the passivation of the alloy via incorporation of REs in the surface film of $Mg(OH)_2$ or stabilize corrosion product films to suppress further corrosion [196-198]. The improved corrosion resistance of the 2 Gd alloy can be explained as the incorporation of oxidized Gd by substituting magnesium cations thereby preventing the incorporation of chloride anions in the $Mg(OH)_2$ lattice resulting in the decreased susceptibility of the passive film breakdown.

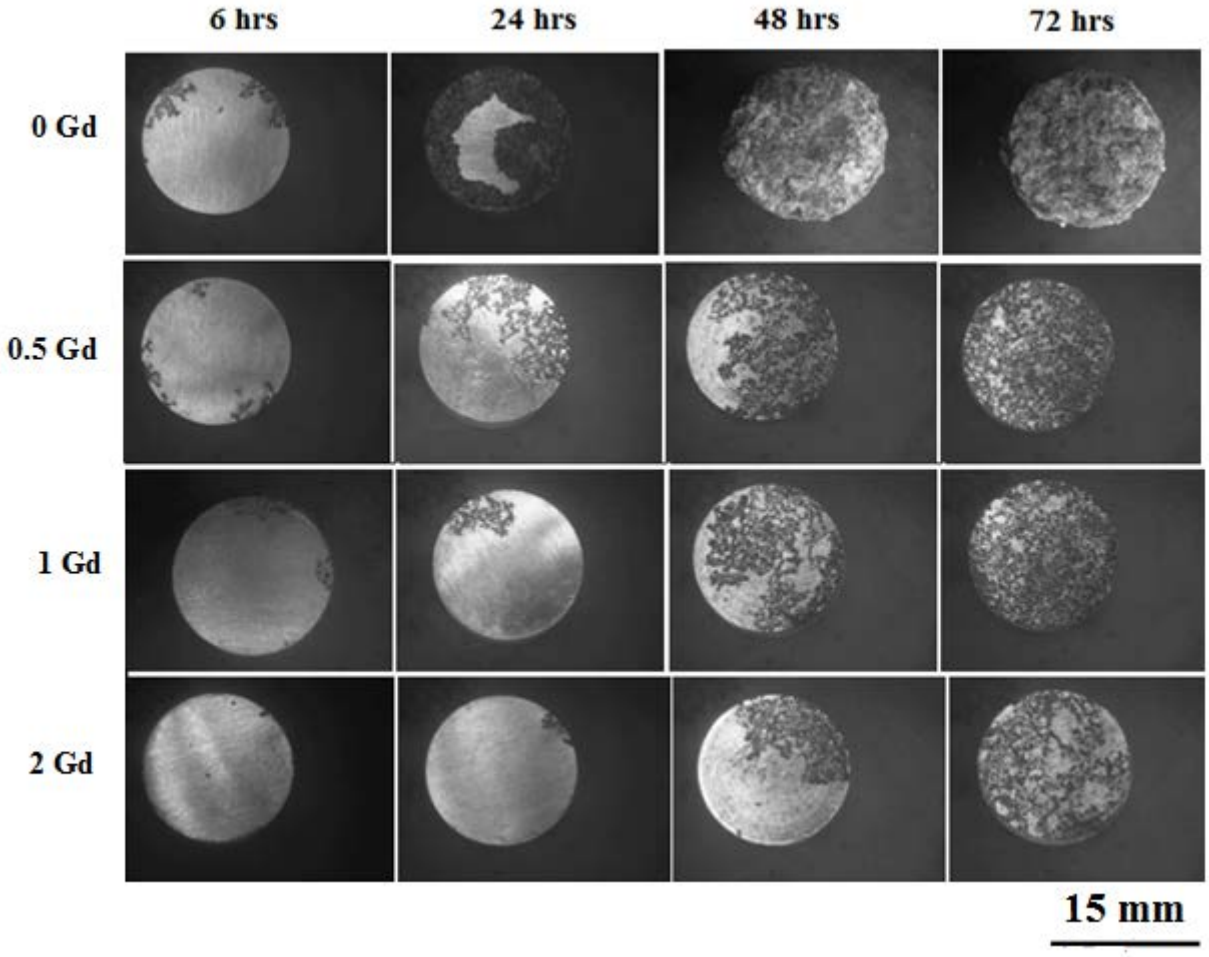

Fig. 6.2 *Macro images of the corroded Mg-Al-Gd alloys at different immersion time.*

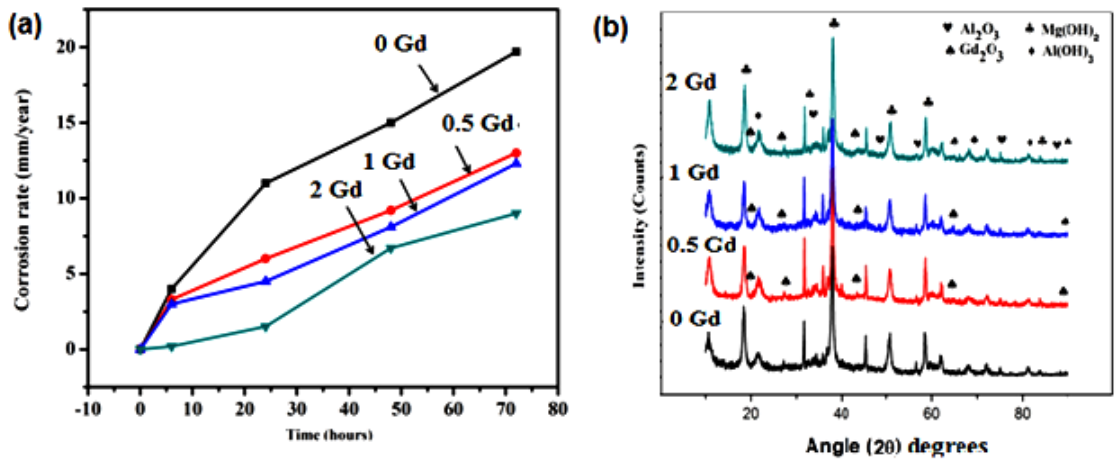

Fig. 6.3 *(a) Corrosion rate, and (b) XRD results of the corroded Mg-Al-Gd alloys.*

6.2.2 Mg-Al-Gd-Ca Alloys

6.2.2.1 Electrochemical test

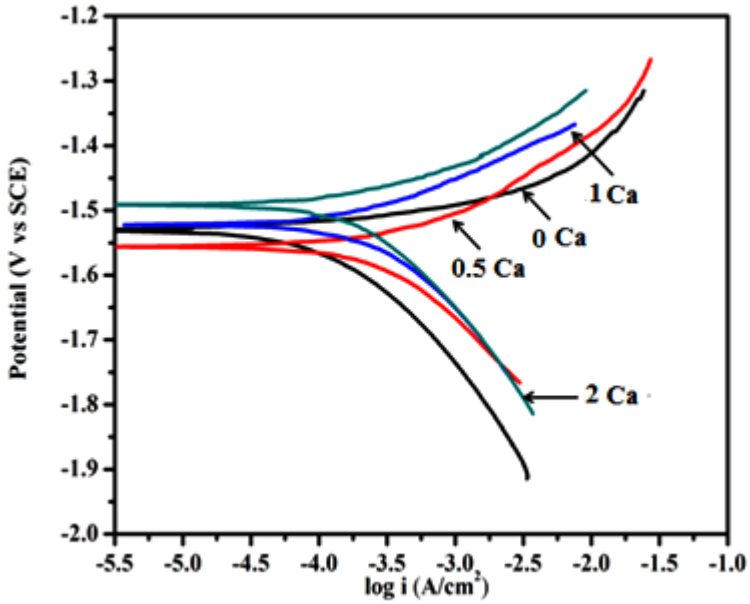

Fig. 6.4 *Tafel plot of the Mg-Al-Gd-Ca alloys.*

Table 6.3 *Electrochemical result of the Mg-Al-Gd-Ca alloys.*

	0 Ca	0.5 Ca	1 Ca	2 Ca
i_{corr}	0.085	0.259	0.261	0.331
(mA/cm^2)	(±0.004)	(±0.042)	(±0.053)	(±0.032)
E_{corr}	-1.530	-1.552	-1.524	-1.491
(V)	(±0.036)	(±0.026)	(±0.036)	(±0.023)

The electrochemical polarization curves of the developed alloys are presented in Fig. 6.4 and the polarization features such as i_{corr} and E_{corr} of the alloys, measured from polarization curves are given in Table 6.3. The E_{corr} values of the investigated alloys varied between -1.55 V and -1.49 V. The current density values increases with increase in the amount of Ca in the following order: 0 Ca < 0.5 Ca < 1 Ca < 2 Ca. It is seen that the i_{corr} values of all the Ca added alloys are one order magnitude higher than that of Mg-9Al-2Gd (0 Ca) alloy suggesting that Ca addition reduce the corrosion resistance. The increasing Ca content shifted the polarization curves to more positive potentials which is due to the formation of Al_2Ca phase. According to the electrochemical results, the Ca addition hinders the corrosion resistance of Mg-Al-Gd alloys.

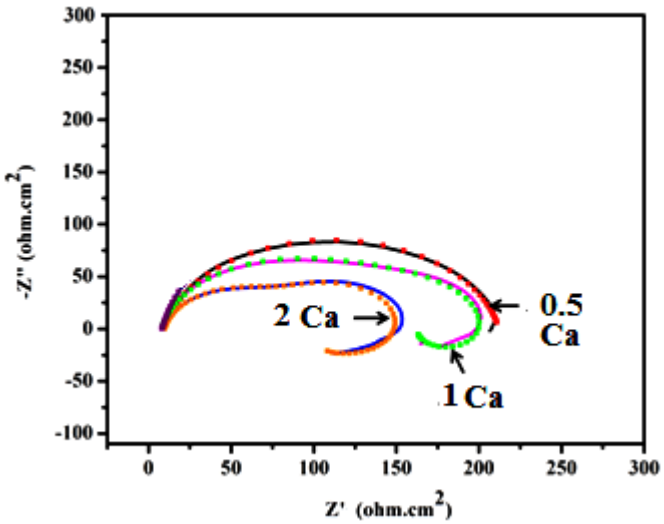

Fig.6.5 *Nyquist plot of the Mg-Al-Gd-Ca alloys.*

Nyquist plot of the studied samples and the simulated fittings (Fig. 6.5**)** are found to be well fitted with the experimental spectra. Among the studied alloys, 0 Ca alloy exhibited a larger diameter whereas, 2 Ca alloy exhibited lowest diameter indicating that corrosion resistance of alloys decreased with increase in Ca content.

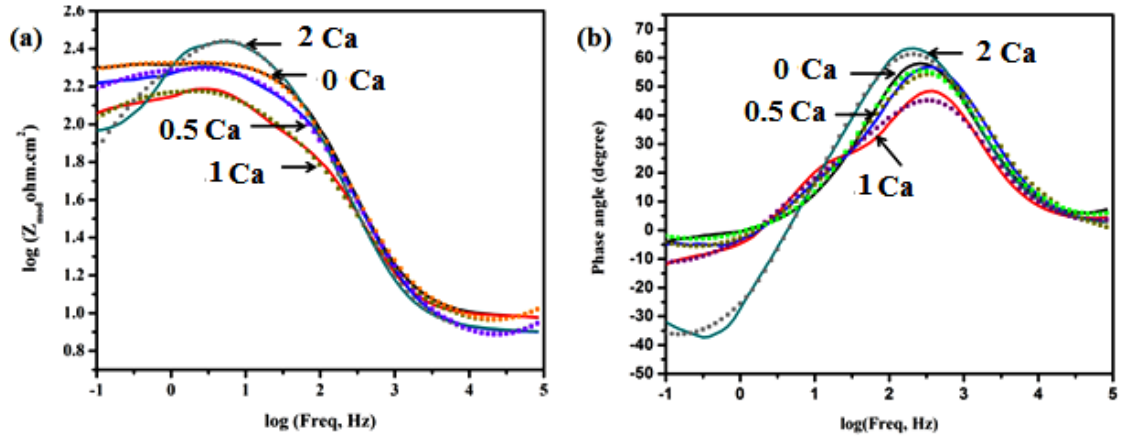

Fig.6.6 *Bode plots (a)* log Z_{mod} v/s log Freq *and (b)* Phase angle v/s log Freq *of the Mg-Al-Gd-Ca alloys.*

The Bode plots are represented by log Z_{mod} v/s log Freq (Fig. 6.6(a)) and Phase angle v/s log Freq (Fig. 6.6(b)) respectively. Generally, for bare substrates, the high frequency capacitive loop indicates the oxide or hydroxide formation at the metal-solution interface due to corrosion during the test. The intermediate frequency loop represents the mass transfer region in the solid phase caused by the diffusion of Mg^{2+} ions coming out through oxide or hydroxide layer or through the corrosion products on the bare sample. The low frequency inductive loops are normally due to the relaxation of the adsorbed species [199,200]. The high frequency region in Fig. 6.6(a) represents the solution resistance (R_s). It is seen that there is not much significant variation in the R_s value. A sudden dip in the curves at low frequency region for 2 Ca alloy could be interpreted as the effect of degraded corrosion resistance. The Z_{mod} of samples at lower frequency region (0.1 Hz) decreased in the following order: 0 Ca (200 cm^2) > 0.5 Ca (165 cm^2) > 1 Ca (120 cm^2) > 2 Ca (96 cm^2). The highest Z_{mod} value of 0 Ca alloy represents its enhanced corrosion resistance among the studied alloys.

The equivalent circuit model to fit the EIS data are presented in Fig. 6.7 and the fitted EIS values of the experimental alloys are summarized in Table 6.4. The R_1 values of the samples (in the high frequency domain) decreased in the following order: 0 Ca >

0.5 Ca > 1 Ca > 2 Ca. Among the studied alloys, 0 Ca alloy showed the highest resistance indicating its increased corrosion resistance. The fitted values of Q_1 shows continuous increase in the following order: 0 Ca < 0.5 Ca < 1 Ca < 2 Ca. It is observed that the Q values are increasing with the addition of Ca implying that more area is being subjected to corrosion. The similar values of Q observed in all the studied alloys indicated that the protection offered by the corrosion product was similar. The values of 'n' for all the alloys are close to unity, indicating a capacitance behavior. As discussed earlier, the deviation observed in the 'n' values is normally due to non-uniform current distribution. The presence of inductive loop indicate the occurrence of pitting corrosion in the samples. The L_1 values are seen to be increasing with increasing Ca content and the maximum value is obtained for 2 Ca alloy indicating its degraded corrosion resistance.

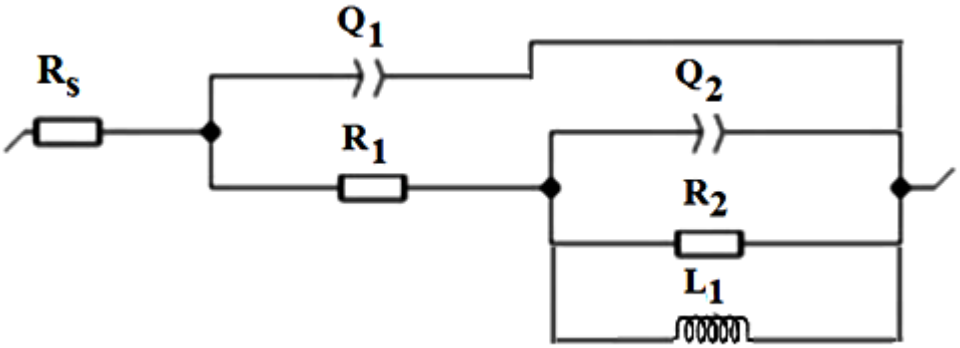

Fig. 6.7 *Equivalent circuit model of the Mg-Al-Gd-Ca alloys.*

Table 6.4 *The fitted EIS values of the Mg-Al-Gd-Ca alloys.*

	0 Ca	0.5 Ca	1 Ca	2 Ca
R_s ($\Omega.cm^2$)	9.549	9.613	9.989	9.541
Q_1 ($s^n/\Omega.cm^2$)	22.17×10^{-6}	36.05×10^{-6}	39.87×10^{-6}	43.81×10^{-6}
n_1	0.9662	0.8868	0.886	0.8814
R_1 ($\Omega.cm^2$)	180.2	170.5	154.5	93.08
Q_2 ($s^n/\Omega.cm^2$)	23.06×10^{-6}	55.765×10^{-6}	46.98×10^{-5}	65.26×10^{-5}

n_2	0.8868	0.9756	0.931	0.9432
R_2 ($\Omega.cm^2$)	50.72	40.806	41.41	48.54
L_1 (H)	1.734	7.865	31.653	38.612

6.2.2.2. Immersion test

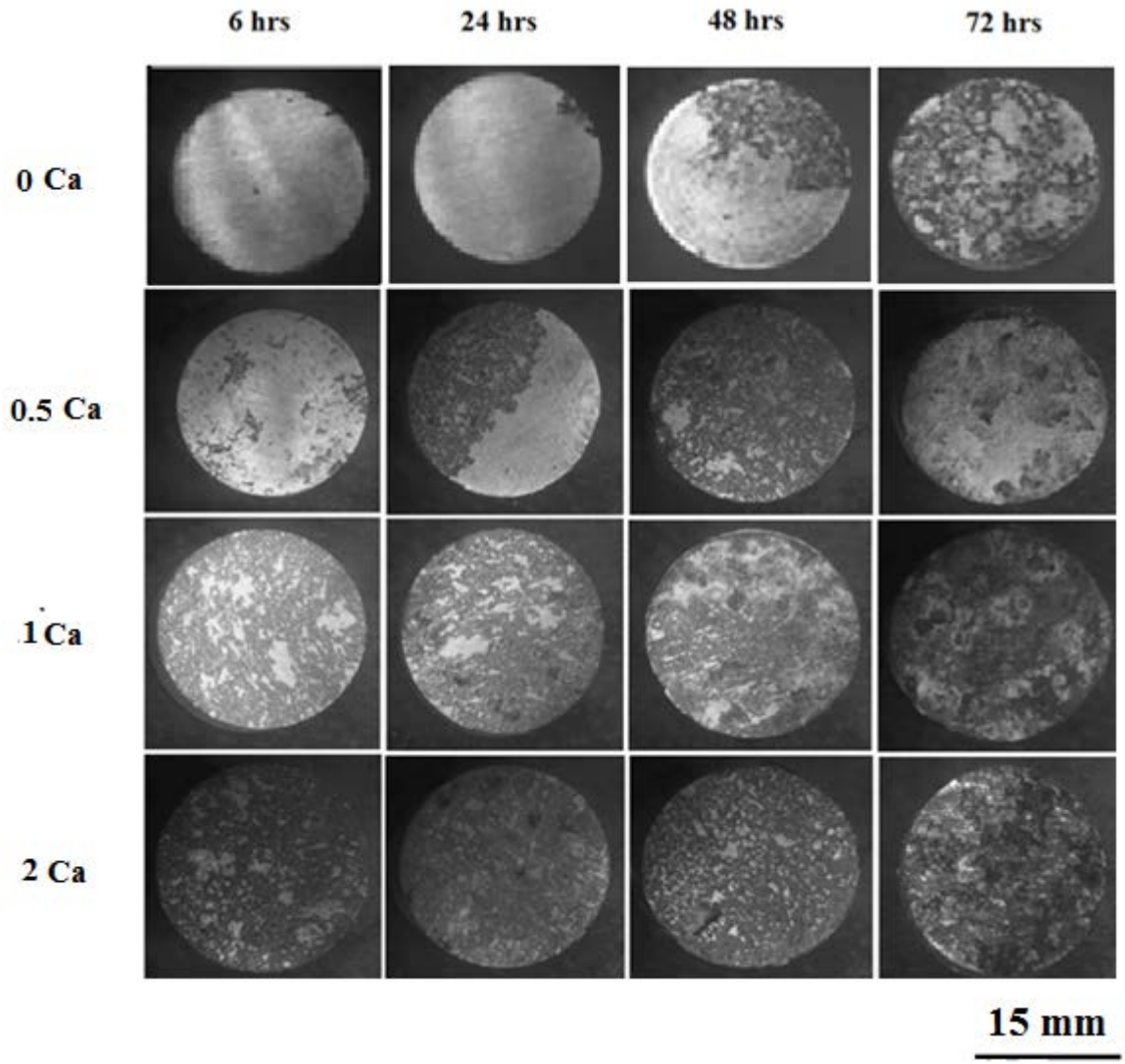

Fig. 6.8 *Macro images of the corroded Mg-Al-Gd-Ca alloys kept at different immersion time.*

To validate the electrochemical test results, immersion tests are done in 3.5 wt.% NaCl solution for a period of 72 h. The corrosion morphology of the alloys after removing corrosion products are shown in Fig. 6.8. The amount of pits are found to be more for Ca added alloys with increasing time revealing the increased corrosion rate

(Fig. 6.9(a)). The XRD pattern of the corroded alloys is presented in Fig. 6.9(b). There are main peaks observed are $Mg(OH)_2$ and $Al(OH)_3$, respectively. When the content of Ca addition is over 1 wt.%, the diffraction peak of $CaCO_3$ was observed due to the reaction of Ca with the atmospheric CO_2 [201,202]. However, the Ca-containing phases are expected to be corroded than the Mg matrix due to the higher electrical potential of these intermetallic compound particles [201-203].

It is known that the main corrosion product, $Mg(OH)_2$ is porous, so the surrounding solution continuously penetrate through the layer and react with the inner fresh magnesium substrate. When the continuous $Mg_{17}Al_{12}$ phases with nobler potential than Mg matrix are corroded, the solution easily goes into the interior of alloys [9]. The immersion test of the developed alloys show that the corrosion rate increases with increase in Ca content.

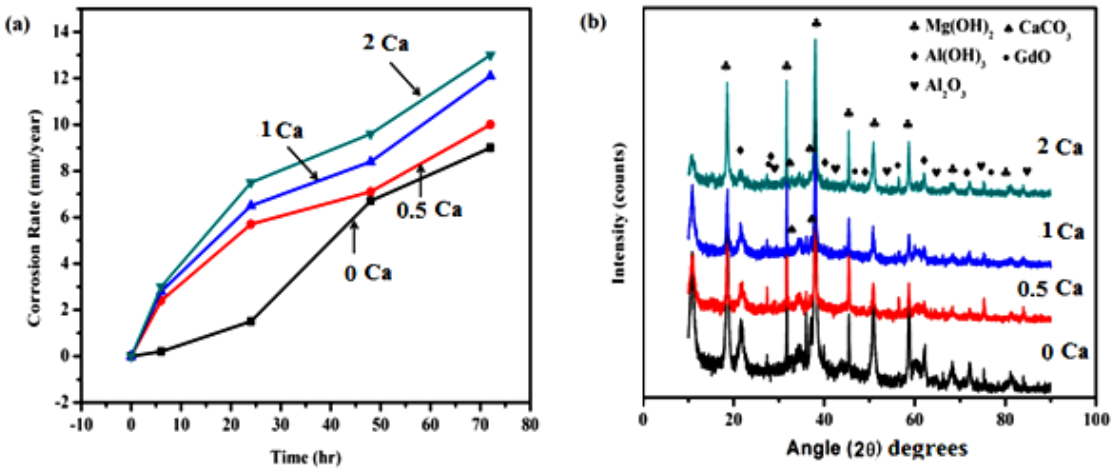

Fig. 6.9(a) *Corrosion rate, and* ***(b)*** *XRD results of the corroded Mg-Al-Gd-Ca alloys.*

The presence of $Mg_{17}Al_{12}$ particles in the matrix accelerate the corrosion rate due to galvanic coupling between the second-phase particles and the α-Mg matrix [204,205]. Even though the Al_2Gd acts as the main corrosion resisting phase, it may also acts as cathode, inducing galvanic effects, because the Al_2Gd surrounding Mg matrix gets preferentially dissolved suggesting the cathodic nature of the same relative

to the Mg matrix [68,69,206]. Ca addition degrade the protectiveness of the passive film [24], resulting in increased pitting. Due to the very limited solubility of Ca in Mg at ambient temperature, such degraded protectiveness of the passive film cannot be understood by the increment of Ca content within the α-Mg matrix. Instead, such degradation of the passive film can result from the reduction of solid solubility of Al in the α-Mg matrix by Ca alloying, as has been reported previously [205,207]. In addition, the formation of the passive film may occur in a more inhomogeneous manner with increasing Ca content, which enlarges the local potential difference. The Al_2Ca particles act as cathodic sites relative to the α-Mg matrix thereby providing preferable sites for pit initiation. After passive film breakdown, the corrosion rate of the alloys is determined by the general corrosion rate of the α-Mg matrix. This is understandable when considering that passive films on Mg alloys are hardly repassivated, as has been extensively reported [207]. The general corrosion rate of the alloys tends to increase as the Ca content increases; this can be primarily attributed to the degradation of the passive film by alloying with Ca. Besides, the presence of $Mg_{17}Al_{12}$ particles, which being nobler than the α-Mg matrix, act as microcathodes, causing internal galvanic corrosion thereby accelerating the corrosion process. Therefore, the deteriorated corrosion resistance observed in the Ca-containing Mg-Al-Gd alloys can be attributed to the combined effect of alloyed Ca on the degradation of passive film as well as the enhancement of microgalvanic corrosion.

6.2.3 Mg-Zn-Gd Alloys

6.2.3.1 Electrochemical test

The potentiodynamic polarization behavior of the developed alloys depicted in Fig. 6.10 and the polarization features such as i_{corr} and E_{corr} of the alloys, measured from polarization curves are presented in Table 6.5.

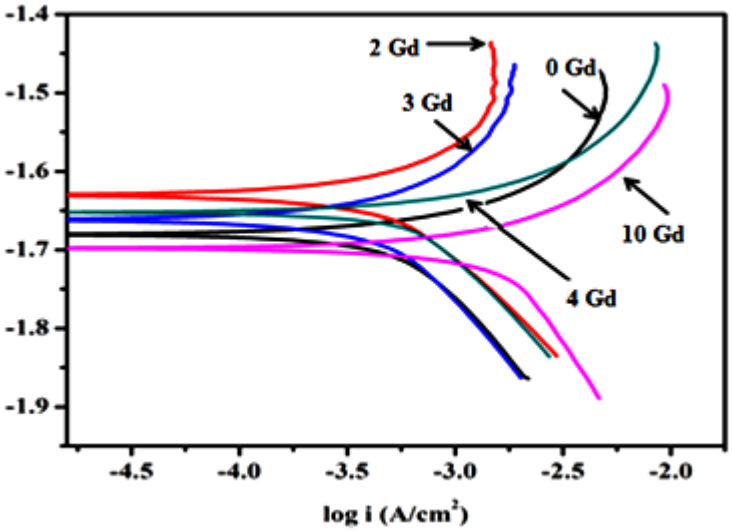

Fig. 6.10 *Tafel plots of the Mg-Zn-Gd alloys.*

Table. 6.5 *Electrochemical results of the Mg-Zn-Gd Alloys.*

	0 Gd	2 Gd	3 Gd	4 Gd	10 Gd
$\mathbf{i_{corr}}$ $\mathbf{(mA/cm^2)}$	2.073 (±0.024)	0.991 (±0.010)	0.892 (±0.021)	2.010 (±0.011)	3.026 (±0.046)
$\mathbf{E_{corr}}$ **(V)**	-1.683 (±0.013)	-1.632 (±0.021)	-1.652 (±0.010)	-1.662 (±0.033)	-1.698 (±0.024)

It is observed that the polarization curves between the anodic and cathodic branches is unsymmetrical. The slope of log i versus applied potential is found to be sharper in the anodic side. The complicated nature of the anodic polarization curves is due to the simultaneous combination of anodic dissolution and cathodic hydrogen evolution in the anodic region. Localized corrosion is yet another probable reason which could make the anodic process unstable. The E_{corr} values of the investigated alloys varied between -1.63 V and -1.698 V. Gd addition upto 3 wt.% shifted the cathodic portion of the curves towards lower current densities suggesting that the cathodic hydrogen evolution reaction decreased resulting in an improved corrosion resistance. The corrosion current densities (i_{corr}) of the alloys with Gd addition is lower

than that of the 0 Gd alloy, with appreciable reduction for 3 Gd alloy which is one order magnitude lower than base alloy implying that this alloy has highest corrosion resistance. In the present study, the alloys are tested in the as cast condition, and they consisted of coarse second phases at the grain boundaries. During corrosion most of the second phases in the Mg alloys are nobler than the magnesium matrix, forming galvanic couples with the matrix thereby acting as cathodic sites [176]. The volume of the second phases increases as the Gd content in the alloy increase, and more continuous networks of second phase are observed. Moreover, in addition to the volume fractions, the types of second phases and their morphologies also differ from alloy to alloy. 2 Gd, 3 Gd and 4 Gd alloys consisted of I-phase and $(Mg,Zn)_3Gd$ phase and 3 Gd alloy contains the maximum volume fraction of I-phase accounting for the improved corrosion resistance. As the Gd content is increased above 3 wt.%, more continuous $(Mg,Zn)_3Gd$ phase are seen in the microstructure thus accounting for decreased corrosion resistance . The electrochemical results indicate that Gd upto 3 wt.% is effective in enhancing the corrosion resistance of Mg-5Zn alloys by suppressing the hydrogen evolution.

The electrochemical impedance spectroscopy (EIS) behavior of the studied samples are represented as Nyquist plot (Fig. 6.11) and the simulated fitting circuit is shown in Fig. 6.12, which is found to be well fitted with the experimental spectra. Among the studied alloys, 3 Gd alloy exhibited a larger diameter whereas 10 Gd alloy showed lowest diameter indicating that corrosion resistance of alloys decreased with increase in Gd content above 3 wt.%. The fitted EIS values of the experimental alloys are summarized in Table 6.6.

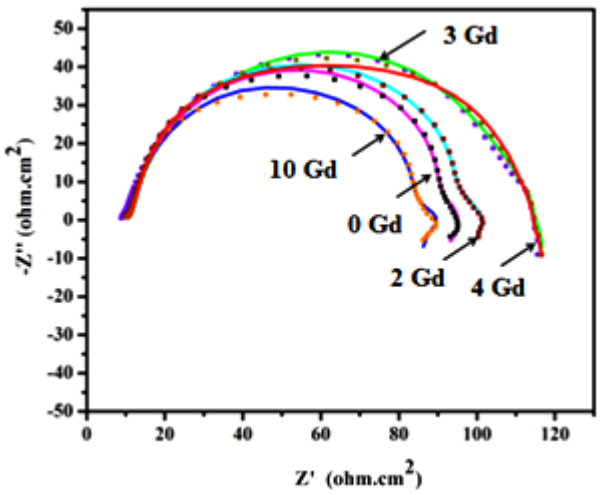

Fig. 6.11 *Nyquist curves of the Mg-Zn-Gd alloys.*

Table 6.6 *The fitted EIS values of the Mg-Zn-Gd alloys.*

	0 Gd	2 Gd	3 Gd	4 Gd	10 Gd
R_s ($\Omega.cm^2$)	9.455	9.621	9.022	9.689	9.333
Q_1 ($s^n/\Omega.cm^2$)	50.32 $x10^{-6}$	46.21$x10^{-6}$	42.59 $x10^{-6}$	52.41 $x10^{-6}$	60.59 $x10^{-6}$
n_1	0.8875	0.8796	0.8592	0.9813	0.8342
R_1 ($\Omega.cm^2$)	75.56	89.14	93.03	77.27	71.24
Q_2 ($s^n/\Omega.cm^2$)	9.07 $x10^{-6}$	7.177 $x10^{-6}$	5.644 $x10^{-7}$	11.656 $x10^{-6}$	9.043 $x10^{-4}$
n_2	0.8885	0.8569	0.9323	0.9123	0.8649
R_2 ($\Omega.cm^2$)	19.14	25.22	27.99	21.48	25.17
L_1 (H)	21.57	17.92	14.84	23.33	30.51

The R_1 values of the samples (in the high frequency domain) varied in the following order: 10 Gd < 4 Gd < 0 Gd < 2 Gd < 3 Gd. Among the studied alloys, 3 Gd alloy showed the highest resistance indicating its increased corrosion resistance. The fitted values of Q_1 are in the following order: 10 Gd > 4 Gd > 0 Gd > 2 Gd > 3 Gd. It is observed that the Q values are decreasing till 3 wt.% Gd addition implying that the area being corroded is getting decreased. The values of 'n' for all the alloys are close to unity, indicating a capacitance behavior. However, the deviation observed in the 'n'

values is normally due to non-uniform current distribution. The L_1 values are seen to be increasing with increasing Gd content above 3 wt.% and the maximum value is obtained for 10 Gd alloy (30.51H) indicating its degraded corrosion resistance.

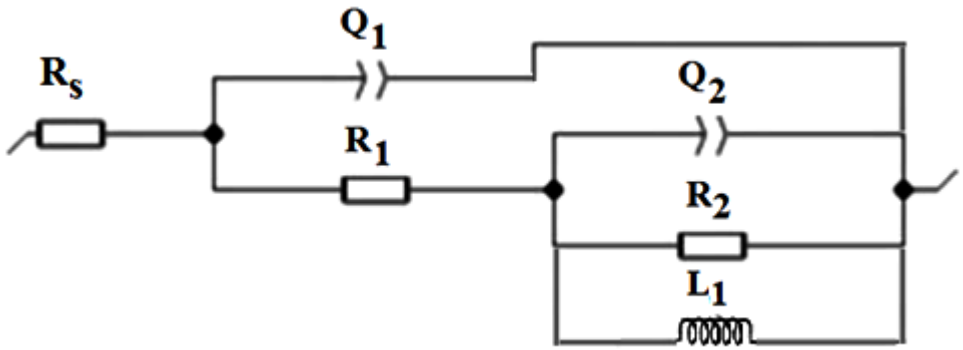

Fig. 6.12 *Equivalent circuit model of the Mg-Zn-Gd alloys.*

6.2.3.2 Immersion test

Previous studies on the corrosion behavior of Mg–Al alloys suggested that the β phases degrade the corrosion resistance when they were at the grain boundaries in bulk and discontinuous form [176,208]. RE additions as major alloying elements in Mg alloys such as Mg–La, Mg–Ce, Mg–Nd and Mg–Y alloys have shown that the increase in RE elements increases the corrosion rates of the alloys owing to the presence of the second phases and that the galvanic effect [209-212]. To verify the corrosion behavior of the studied alloys, post-corrosion test microstructures are analyzed. Fig. 6.13 depicts the typical macrostructures of immersion tested alloys for different times after corrosion products were removed. The preliminary results of the present study indicate that the corrosion resistance of the Mg-Zn-Gd alloys decreased as the second phases in the alloys increased beyond 3 wt.% Gd. The corrosion rate (Fig. 6.14) of 3 Gd alloy was around 3 mm/yr, whereas, the corrosion rate of 10 Gd alloy was around 21 mm/yr, which is 7 times higher after 72 hours. Thus, the decline of corrosion resistance can be confirmed with the increase in Gd content.

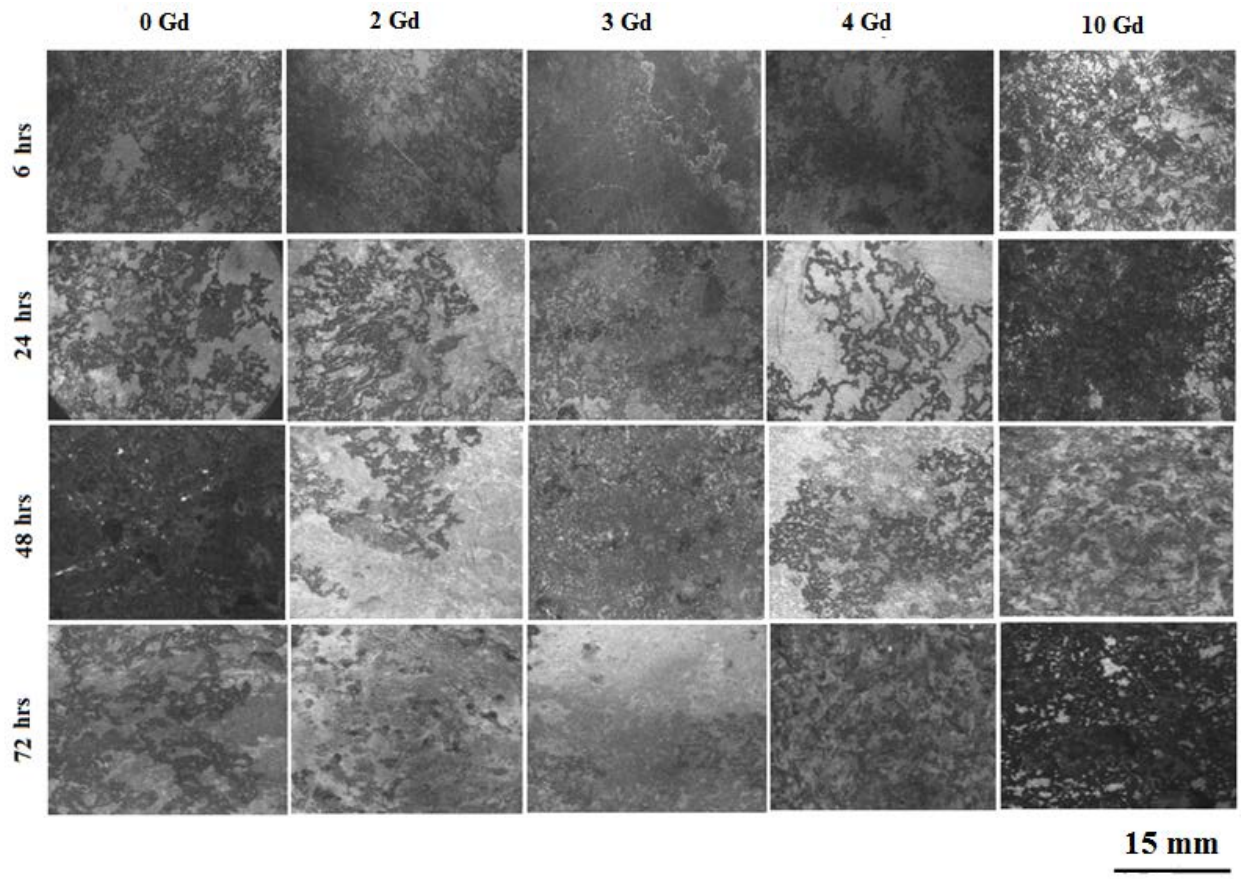

Fig. 6.13 *Surface macrographs of the Mg-Zn-Gd alloys for different time periods.*

Due to galvanic corrosion, the continuous dissolution of matrix around the intermetallics has led to undermining of the intermetallics. The dissolution of second phases themselves in the later stages of corrosion is another possibility if the stability of the second phases was altered by NaCl solution, and stronger alkalinization of the surface corrosion products after long immersion times. The difference in chemical composition of the same intermetallic phase in the alloys may also influence the severity of micro-galvanic process. Moreover, the types and morphologies of second phases differed from alloy to alloy. 2 Gd alloy consisted of mainly $(Mg,Zn)_3Gd$ phase with a morphology of rod and small spherical shape. Hence, less corrosion was observed. In 3 Gd alloy, in addition to $(Mg, Zn)_3Gd$ phase, an increase in the volume of Mg_3Zn_6Gd phase are observed. The I-phase enhances the corrosion resistance of an

Mg–Zn-RE alloys [135]. It is seen that the volume of the second phases increased as the total amount of alloying elements increased, and more continuous networks of $(Mg,Zn)_3Gd$ phase are observed in 10 Gd alloy attributing to higher corrosion rate. Moreover, the $Mg_{12}ZnGd$ (X-phase) present in the matrix might also have influenced the corrosion process. Previous studies on Mg–Zn–Y alloys show that the increase in the volume of X-phase increased the corrosion rate due to the galvanic coupling effect.

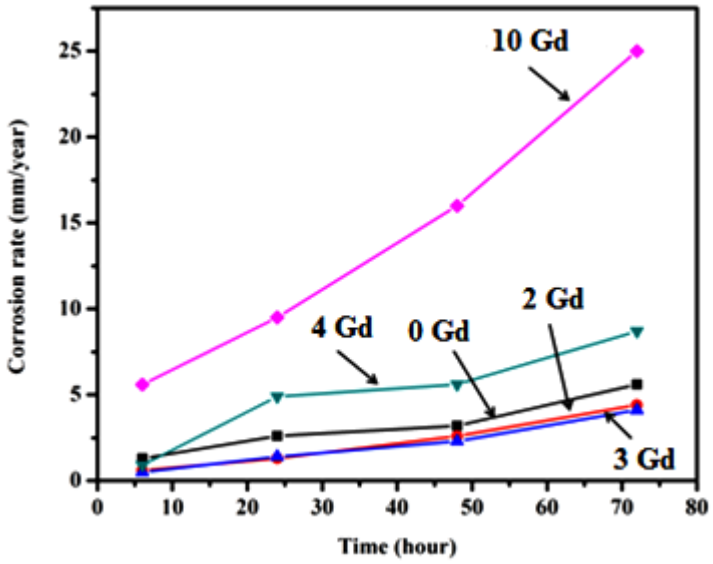

Fig. 6.14 *Corrosion rate of the Mg-Zn-Gd alloys for different time periods.*

The pH value of 3.5% NaCl solution was found to be 7.15 at 37±0.5°C before the test and it is seen to increase to 10.30, which can stimulate the formation of $Mg(OH)_2$ which inturn can partially protect the area thereby partially suppressing the localized corrosion. Various other oxide layers like $Zn(OH)_2$ and Gd_2O_3 are also seen in the XRD analysis (Fig. 6.15). It is found that the levels of $Zn(OH)_2$ and Gd_2O_3 have remained almost constant for all Gd added alloys but the intensity of $Mg(OH)_2$ and ZnO is more for 3 Gd alloy, which might have contributed to the better protection of the alloy. For 10 Gd alloy, it is seen that the intensity of ZnO layer formed is very less leading to decline in corrosion resistance.

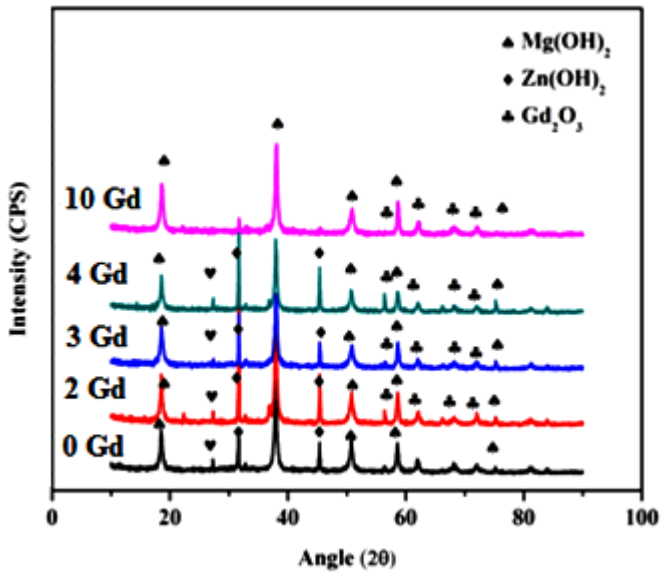

Fig. 6.15 *XRD analysis of the corrosion products of the Mg-Zn-Gd alloys.*

6.2.4 Mg-Zn-Gd-Ca Alloys

6.2.4.1 Electrochemical test

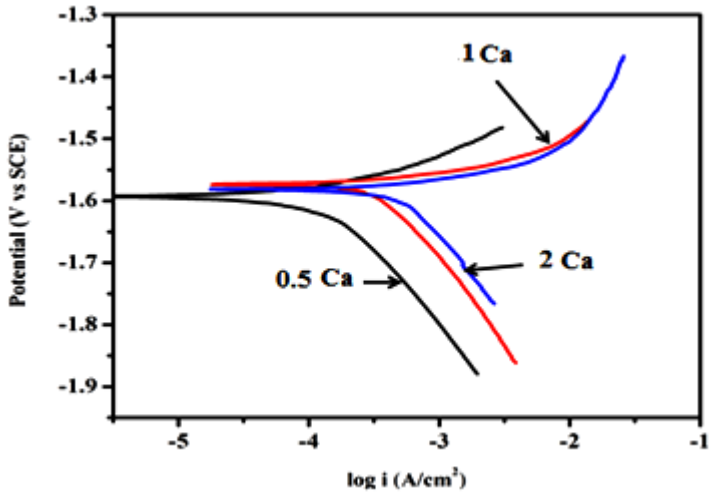

Fig. 6.16 *Tafel plots of the Mg-Zn-Gd-Ca alloys.*

Fig. 6.16 depicts the potentiodynamic polarization curves of Mg-Zn-Gd-xCa alloys, and the corrosion potential (E_{corr}) and corrosion current density (i_{corr}) are shown in Table. 6.7. The E_{corr} values of the developed alloys varied between -1.652 V and -1.574 V. The i_{corr} value is remarkably increased (by one order magnitude), indicating

that the corrosion resistance of Mg-Zn-Gd-xCa alloy deteriorates with increasing Ca addition. The electrochemical potential of $Ca_2Mg_6Zn_3$ phase is higher than α-Mg, therefore the $Ca_2Mg_6Zn_3$ phase acts as active cathodes thus driving the α-Mg substrate to dissolve rapidly through galvanic corrosion [213,214]. The size, distribution and morphology of secondary phases also influence the corrosion resistance of an alloy. The increase in volume fraction of $Ca_2Mg_6Zn_3$ phase due to increase in Ca content also retards the corrosion resistance.

Table. 6.7 *Electrochemical results of the Mg-Zn-Gd-Ca alloys.*

	0 Ca	**0.5 Ca**	**1 Ca**	**2 Ca**
i_{corr}	0.892	1.342	1.215	2.038
(mA/cm^2)	(±0.021)	(±0.033)	(±0.016)	(±0.020)
E_{corr}	-1.652	-1.593	-1.574	-1.581
(V)	(±0.010)	(±0.012)	(±0.015)	(±0.008)

The electrochemical impedance spectroscopy (EIS) behavior of the studied samples are represented as Nyquist plot and the simulated fittings are shown in Fig. 6.17 and found to be well fitted with the experimental spectra. Among the Ca added alloys, 0.5 Ca alloy exhibited a largest diameter whereas 2 Ca alloy showed the lowest diameter indicating that the charge transfer resistance is remarkably decreased with increase in Ca content above 0.5 wt.%. The fitted EIS values of the experimental alloys are summarized in Table 6.8 and the circuit is shown in Fig. 6.18. The R_1 values of the samples (in the high frequency domain) varied in the following order: 0 Ca > 0.5 Ca > 1 Ca > 2 Ca. The increased R_1 value of 0 Ca shows its increased corrosion resistance. The fitted values of Q_1 are in the following order: 0 Ca < 0.5 Ca < 1 Ca < 2 Ca. The increment in the Q_1 values are directly proportional to the area being corroded. As discussed earlier, similar values of Q observed in all the studied alloys indicate that the

protection offered by the corrosion product is similar. Capacitance behavior is indicated by the 'n' value close to unity for all the alloys and slight deviation observed is due to non-uniform current distribution. Pitting corrosion is indicated by the presence of inductive loop at lower frequencies in the samples. The L_1 values are seen to be increasing with increasing Ca content and the maximum value is obtained for 2 Ca alloy (22.84 H) implying that the Mg substrate suffers pitting corrosion.

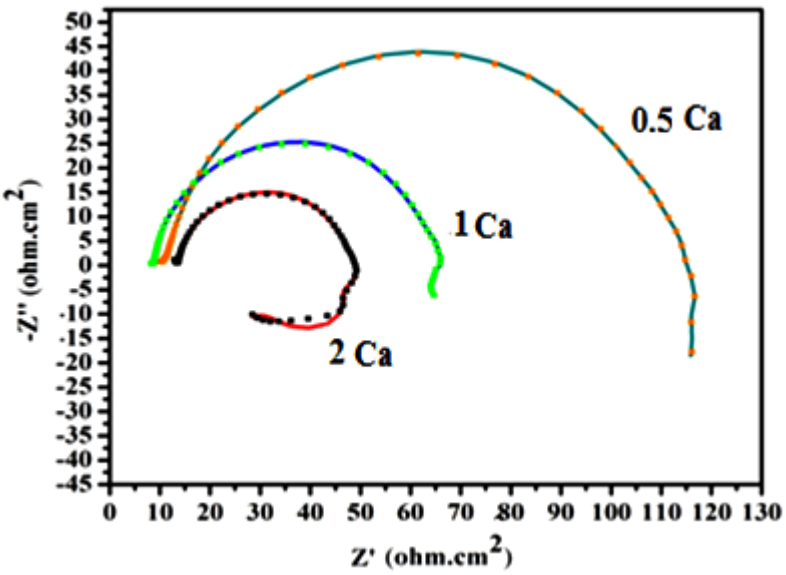

Fig. 6.17 *Nyquist curves of the Mg-Zn-Gd-Ca alloys.*

Table 6.8 *The fitted EIS values of the Mg-Zn-Gd-Ca alloys.*

	0 Ca	0.5 Ca	1 Ca	2 Ca
R_s ($\Omega.cm^2$)	9.022	9.324	10.274	10.166
Q_1 ($s^n/\Omega.cm^2$)	42.59 x10^{-6}	48.8 x10^{-6}	22.7x10^{-5}	34.0 x10^{-5}
n_1	0.8592	0.9045	0.9432	0.885
R_1 ($\Omega.cm^2$)	93.03	67.53	56.34	30.45
Q_2 ($s^n/\Omega.cm^2$)	5.644 x10^{-7}	6.88 x10^{-6}	8.91 x10^{-6}	10.46 x10^{-6}
n_2	0.9323	0.9458	0.9941	0.8212
R_2 ($\Omega.cm^2$)	39.99	27.65	23.05	17.83
L_1 (H)	14.84	16.64	19.92	22.84

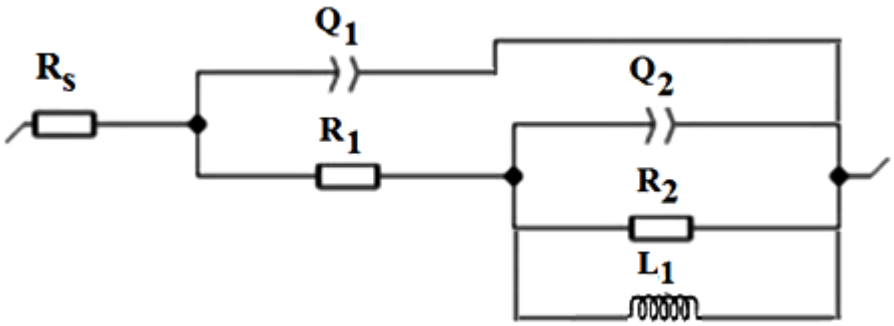

Fig. 6.18 *Equivalent circuit model of the Mg-Zn-Gd-Ca alloys.*

6.2.4.2 Immersion test

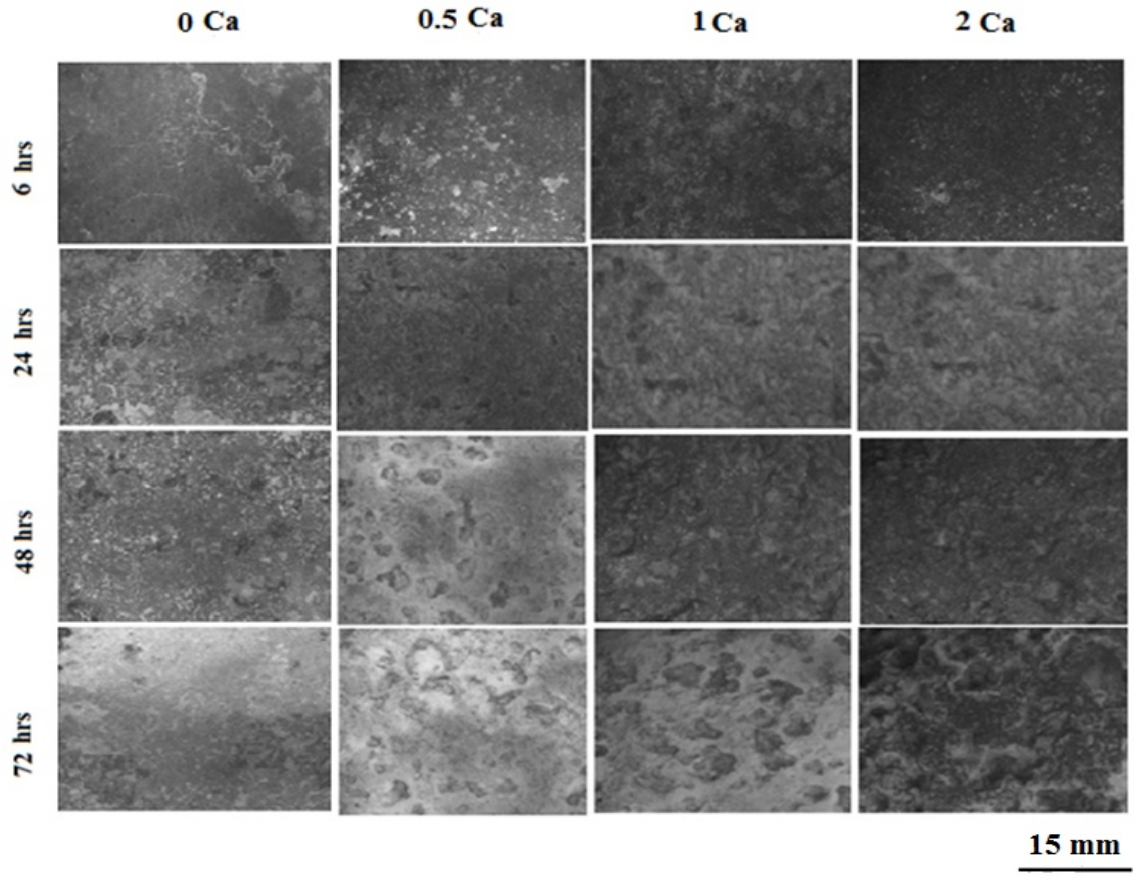

Fig. 6.19 *Surface macrographs of the Mg-Zn-Gd-Ca alloys for different time periods.*

Macro-image examination of immersed Mg-Zn-Gd-xCa samples at different times (after removal of corrosion products) in 3.5 wt.% NaCl are presented in Fig. 6.19. Increased localized corrosion is seen and pitting corrosions becomes prominent in Ca

added alloys after 6h, indicating that Ca accelerates the corrosion of Mg-Zn-Gd-Ca alloy after 0.5 wt.%. The corrosion rate (Fig. 6.20) is seen to increase from 3 mm/year (Mg-5Zn-3Gd alloy) to 8.8 mm/yr at 72 hours for the 2 wt.% Ca added alloy. The galvanic corrosion between secondary phase and α-Mg attributes to the decreased corrosion resistance of the alloy. The secondary phase acts as micro cathode, thereby accelerating the corrosion of the alloys when Ca content increases [215,218].

It is seen that the entire surface of Mg-Zn-RE-Ca alloy are covered by insoluble corrosion products. When 0.5 wt.% of Ca added to Mg-Zn-RE-Ca alloy, the corrosion rate is minimal and the surface is covered by insoluble $Mg(OH)_2$ and white particles. The $Mg(OH)_2$ is converted into a more soluble $MgCl_2$ by the chloride ions in the solution. As discussed earlier, the pitting corrosion is due to the second phases having more positive corrosion potential compared to the Mg matrix. The addition of 1 and 2 wt.% Ca to the alloy causes corrosion products and cracks compared with 0 Ca alloy. 2 Ca alloy suffered severe corrosion attack and hence the formation of many large corrosion pits on the surface. Fig. 6.21 depicts the XRD patterns of the corrosion products. The main peaks observed are $Mg(OH)_2$, $Zn(OH)_2$, Gd_2O_3 and $MgCO_3$.

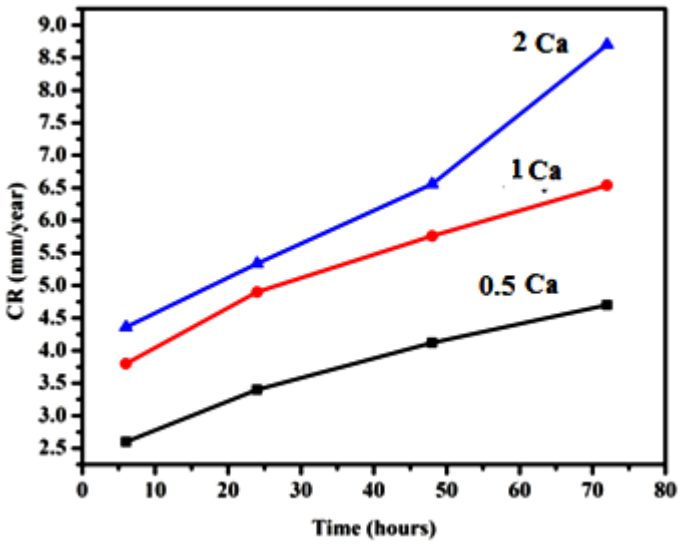

Fig. 6.20 *Corrosion rate of the Mg-Zn-Gd-Ca alloys for different time periods.*

The $Mg(OH)_2$ peaks intensities are seen to be increased with increasing Ca content and is due to the considerable amount of $Mg(OH)_2$ formed on the of specimen surface. $Mg(OH)_2$ has a HCP structure and easily undergoes basal cleavage, caused by the formation of crack on the corrosion product layer [216-218]. It can be also observed that the absorbance of the spectra from the $Mg(OH)_2$ was significantly lower in 0 Ca alloy which led to a lesser cracks compared to that in the other alloys.

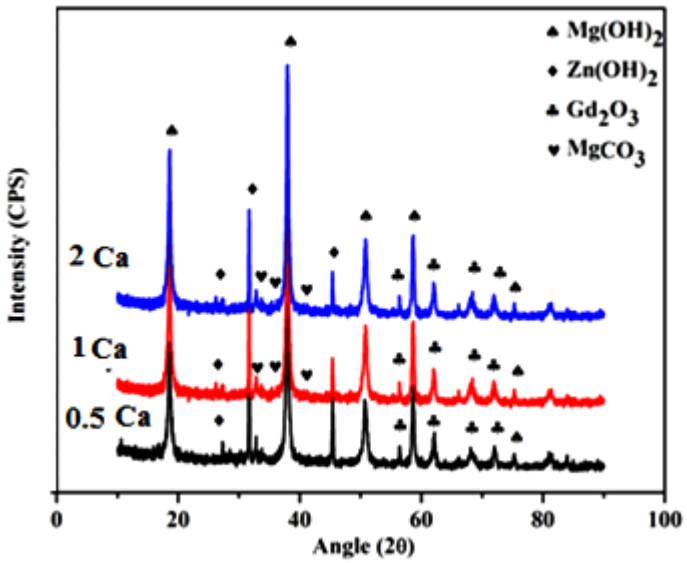

Fig. 6.21 *XRD analysis of the corrosion products of the Mg-Zn-Gd-Ca alloys.*

6.3 Wear Properties

6.3.1 Mg-Al-Gd Alloys

As seen from the hardness data, the Gd addition make the alloy harder, which is mainly due to the formation of Al_2Gd phase, whose volume fraction increased with increasing the Gd concentration. Due to Gd addition, the $Mg_{17}Al_{12}$ phase is substituted by more thermodynamically favorable Al_2Gd phase. The increase in hardness would directly increase the wear resistance of the alloys [57,81,82,219]. The weight loss of samples with varying Gd additions are measured using the pin-on-disc tester and the calculated wear rate is presented in Fig. 6.22.

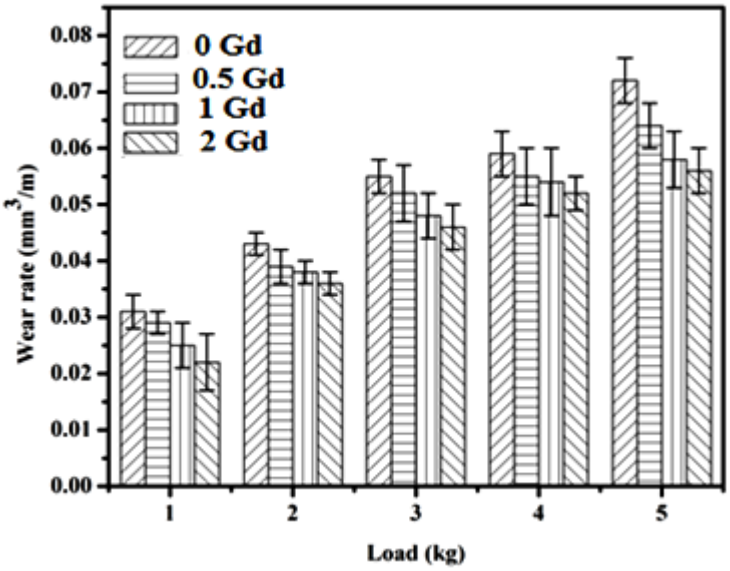

Fig. 6.22 *Wear rate of the Mg-Al-Gd alloys at corresponding loads.*

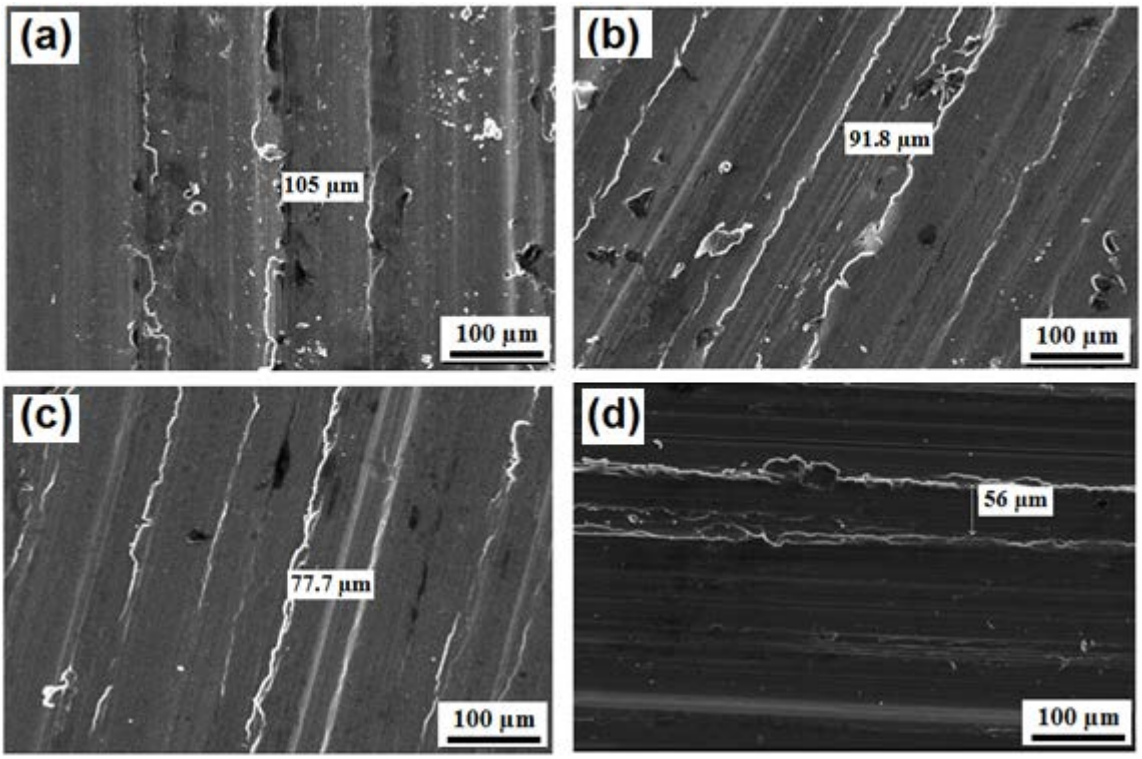

Fig. 6.23 *SEM micrographs of the worn (a) 0 Gd (b) 0.5 Gd (c) 1 Gd, and (d) 2 Gd alloys tested at 5kg.*

It is observed that there is considerable decrease in the weight loss by increasing the content of Gd, which is consistent with the increase in hardness due to the formation of harder Al_2Gd phase, whose volume increases with increase in Gd. The weight loss of

0 Gd alloy is about 18% more than that of 2 Gd alloy. The enhanced wear resistance can also be attributed to the higher thermal stability of Al_2Gd phase, compared to that of $Mg_{17}Al_{12}$. During the dry wear test, due to increase in the sample surface temperature, softening occurs for materials with low-melting temperatures. The thermally stable Al_2Gd phase effectively resists wear under such testing conditions. The wear morphology results of the test specimens at 5 kg load are shown in Fig. 6.23. The wear scar width (WSW) of as cast Mg-9Al alloy is 105 μm. Large pieces of alloy are seen to peel off from matrix, and the cracks propagate in a straightline. Taking into consideration the hardness and second phase, the 2 Gd alloy has the lowest WSW value of 56 μm indicating its higher wear resistance.

6.3.2 Mg-Zn-Gd Alloys

It is observed from the Fig. 6.24 (a) that with increasing Gd content, the wear rate is found to decrease for the same load level till 3 wt %. This is attributed to the strengthening of the alloys by the precipitation of hard Mg_3Zn_6Gd particles. However, with the application of higher normal loads for the same Gd content, the wear rate increases drastically. This is obvious that at higher loads, the soft Mg matrix smears off leading to higher wear in spite of the presence of hard particles. It is fascinating to note that for Mg-5Zn-3Gd alloy, for all the loads, the wear rates are much reduced. It can be also seen from Fig. 6.24 (b) that the wear resistance of 3 Gd alloy is quite appreciable when compared to the other developed alloys. This is due to the presence of Mg_3Zn_6Gd particles embedded in the α-Mg matrix which do not allow the Mg to smudge. Quasicrystals plastically deformable at temperatures about half the melting point, but at low temperatures most quasicrystals show high hardness and low friction coefficient. This combination of properties can be effectively used to improve the wear resistance of materials [220].

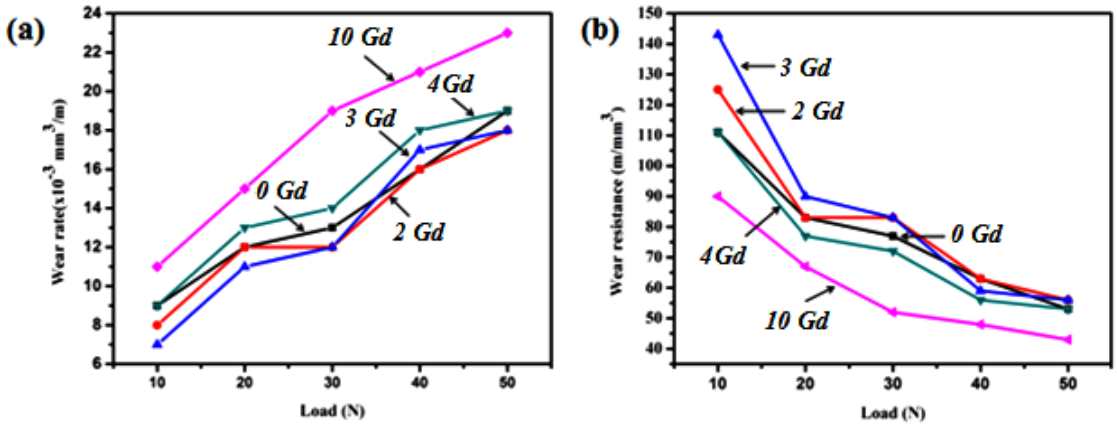

Fig. 6.24 *(a) Wear rate, and (b) wear resistance of the Mg-Zn-Gd alloys.*

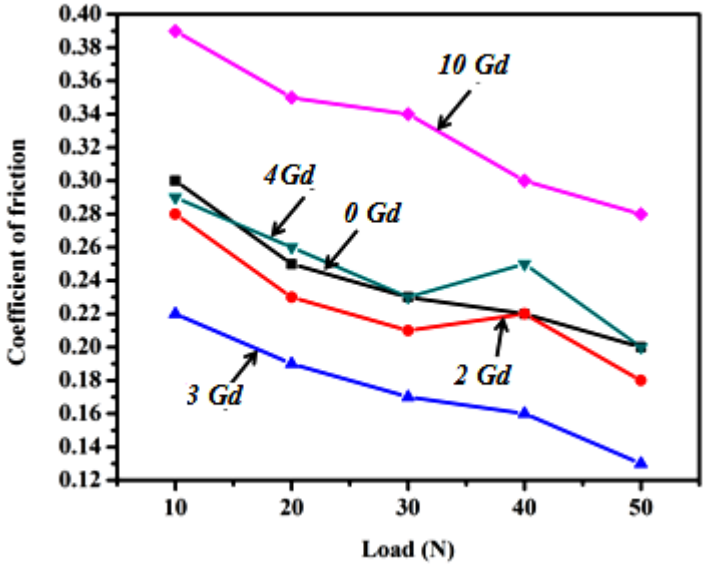

Fig. 6.25 *Coefficient of friction of the Mg-Zn-Gd alloys.*

Zhang et al. [221] investigated the friction and wear behavior of Mg alloys containing I-phase containing and discussed their wear mechanisms. The variations of the friction coefficients of the developed alloys at different applied loads are depicted in Fig. 6.25. The friction coefficients decreased with increase in applied loads for all alloys. When two hard materials come in contact, it leads to the formation of small fracture particles which are picked up again and gradually forms a film on the wear surfaces. Thus, the contact of dissimilar materials tranforms to contact of similar materials, which attributes to the increase in friction coefficient. At a low loads, the

contact temperature will be low and the hardness of alloys can be retained resulting in higher friction coefficients. The friction coefficients initially decreases with increasing Gd content and the lowest value is achieved at 3 wt.% after which the friction coefficients increased. Quasicrystal phases have low friction coefficient and high brittleness [220]. With the increase of Gd content, the quasicrystal phase volume fraction increases. When Gd content is 3 wt.%, the low friction coefficient of quasicrystal phase plays a key role in reducing the friction coefficient of the alloy. With further increase of Gd content, the brittleness is increased with the increase in volume fraction of $(Mg,Zn)_3Gd$ phase. During sliding, some small pieces could be easily removed from the surface by the shear and impact stress. Hence, the surface became coarse, resulting in increased friction resistance and friction coefficient.

The wear scar width (WSW) of the developed alloys at 50 N load are depicted in Fig. 6.26. All the worn surfaces are seen with distinct pattern of grooves and ridges running parallel to one another ensuring the typical characteristic of sliding wear. Deep scratches observed on the worn surfaces of all the tested samples may be attributed to the hard asperities of counter face or detached particles that are removed from the pin and placed on the contact surface. When the normal applied load reaches certain critical thresholds, flash temperatures at contacting asperities could exceed the melting point of the matrix alloy, thus increasing bulk temperature and causing gradual softening of the Mg alloy. Continued sliding or increase in load would raise temperatures further, leading to melting, which is due to the lower thermal stability of the Mg-Al alloys. The micrographs reveal detachment of sheet-like wear debris from the worn surfaces. The pin surface has been subjected to ploughing with obvious deep grooves or scratches. The light scratches found on the worn surface may be attributed to the hard asperities of counter face or detached particles removed from disk or pin. Taking into consideration

the hardness and second phases, the 3 Gd alloy has the lowest WSW value of 72.5 µm indicating its higher wear resistance.

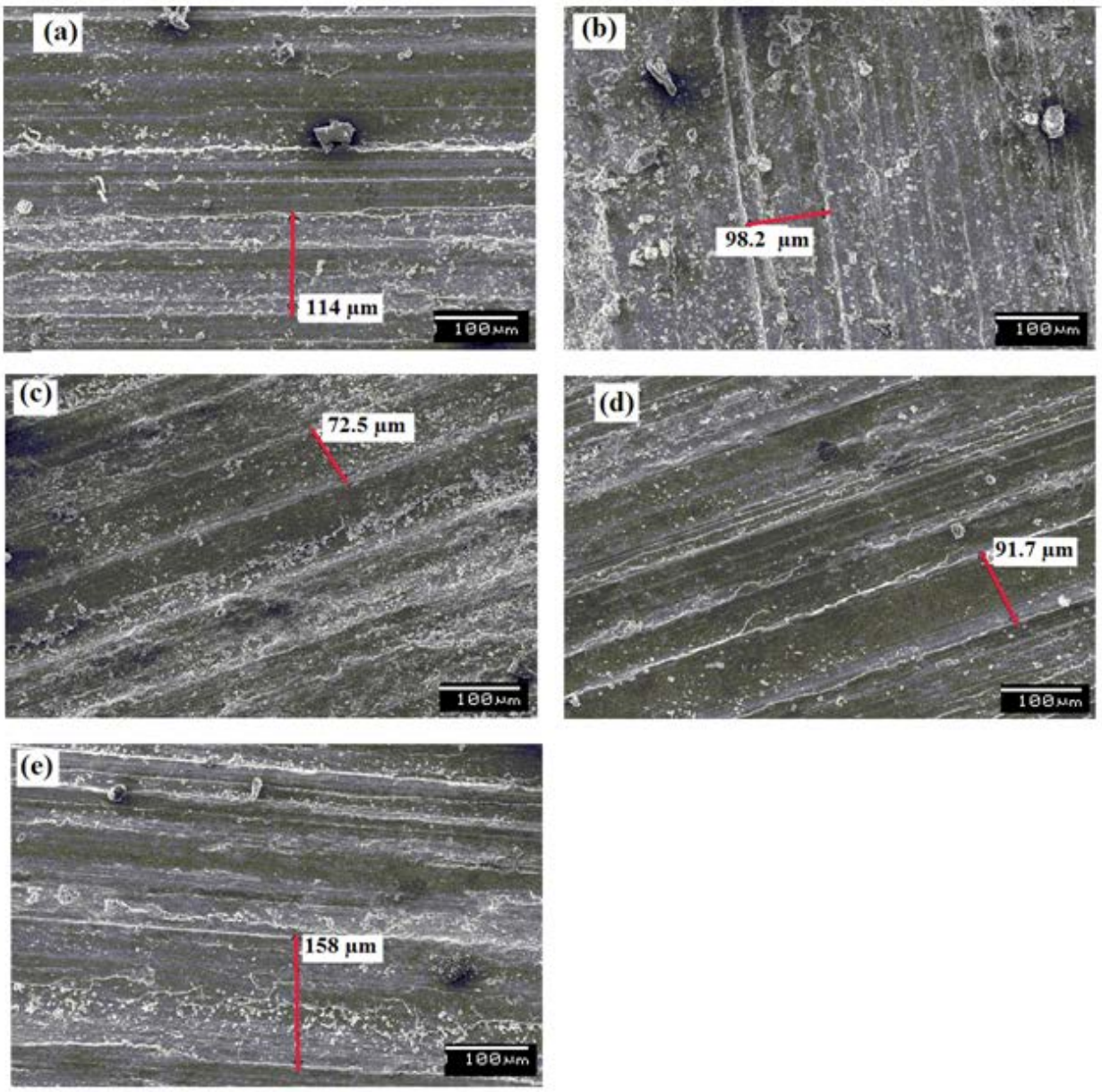

Fig. 6.26 *Wear scar width of (a) 0 Gd (b) 2 Gd (c) 3 Gd (d) 4Gd, and (e) 10 Gd alloys.*

6.4 Conclusions

By the addition of Gd, both the Mg-Al and Mg-Zn alloy systems have shown improvement in corrosion as well as wear properties. The conclusions drawn from the study are as follows:

- From the potentiodynamic polarization behavior of Mg-Al-Gd alloys, it is seen that the Gd additions have shifted the cathodic portion of the curves towards lower current densities suggesting increased corrosion resistance. The Mg-9Al-2Gd alloy has the lowest i_{corr} and the most negative E_{corr}, which means that this alloy has the strongest suppression effect in cathodic hydrogen evolution and the highest corrosion resistance. The diameter of the capacitive semicircle in Nyquist plot is the largest for Mg-9Al-2Gd alloy which confirms its corrosion resistance.
- The increasing Ca content in Mg-Al-Gd alloys shifted the polarization curves to more positive potentials which is due to the formation of Al_2Ca phase. The i_{corr} values of Ca added alloys are one order magnitude higher than the base alloy and the i_{corr} values are seen to slightly increase with increase in Ca wt.% implying the decline in corrosion resistance. The diameter of the semicircle in the nyquist plot is seen to be decreased with increase in Ca content which confirms the degraded corrosion resistance of alloys. At 72 hours of immersion test, the corrosion rate of Ca added alloys increased to 44 % of that of base alloy.
- Corrosion resistance of the Gd added Mg-Zn alloys increased till 3 wt.% and then declined. From the potentiodynamic polarization behavior, it is seen that the Mg-5Zn-3Gd alloy has the lowest i_{corr} and the most negative E_{corr}, which points that this alloy has the strongest suppression effect in cathodic hydrogen evolution and the highest corrosion resistance. The diameter of the capacitive semicircle in Nyquist plot is the largest for the same alloy which confirms its corrosion resistance.

- The increase in corrosion rate of the Gd added Mg-Zn alloys above 3 wt.% can be attributed to the presence of continuous (Mg, Zn)$_3$Gd phase and $Mg_{12}ZnGd$ phases at the boundaries. The corrosion rate of Mg-5Zn-10Gd alloy **is** around 7 times higher than Mg-5Zn-3Gd alloy after 72 hours.
- The corrosion resistance of Ca added Mg-Zn-Gd alloys are found to be deteriorating with increase in Ca content. In addition to the W-phase, $Ca_2Mg_6Zn_3$ phases also act as cathodic sites and accelerate the corrosion rate.
- It is observed that there is a decline in the wear rate by increasing the content of Gd to Mg-Al alloys, which is consistent with the increase in hardness due to the formation of harder Al_2Gd phase, whose volume fraction increases with increase in Gd. The Wear Scar Width (WSW) of the Mg-9Al-2Gd alloy is decreased by 46%, compared with the cast Mg-9Al alloy indicating its enhanced wear resistance.
- There is considerable decrease in the wear rate upto 3 wt.% Gd addition to Mg-5Zn alloy which is attributed to the strengthening of the alloys by the precipitation of hard Mg_3Zn_6Gd particles. With further increase of Gd content, the brittleness increased with the increase in volume fraction of (Mg,Zn)$_3$Gd phase. The Wear Scar Width (WSW) of the Mg-5Zn-3Gd alloy is decreased by 36%, compared with the cast Mg-5Zn alloy indicating its enhanced wear resistance.

Chapter 7 Summary & Conclusions

7. 1 Introduction

During the past half century, much progress has been made on the application of magnesium and its alloys in the automotive and aeronautical industries. The prime advantage of magnesium is its low density (1.74 g/cm^3) and high specific strength. Many researchers have made efforts to replace materials being used in automobile industries such as steel and aluminium with a material having low density and high specific strength. Magnesium, is having a density of only 20 % that of steel and 60% that of aluminium. The development of Mg alloys with enhanced mechanical, corrosion and wear properties have been considered and investigations undertaken. The elemental additions of Sb, Ca, RE, Sr, Si, etc which leads to the formation of thermally stable and morphologically favorable intermetallic phases have been extensively studied. These intermetallic phases effectively block the dislocation motion and restrict the grain boundary sliding during creep. Among these elements, rare earth additions have many merits such as purifying the alloy melt, modifying the castability, refining the microstructure, improving the mechanical properties and anti-oxidization properties. The present work attempts to understand the microstructure, mechanical and wear properties of Mg-Al and Mg-Zn alloys with varying Gd. Moreover, it is necessary to refine the α-Mg phase and modify the phases in alloys to improve their properties. Hence the effect of varying Ca wt.% on the optimal Mg-Al-Gd and Mg-Zn-Gd Mg-Si are also studied.

The present chapter highlights the significant conclusions drawn from the present work. Also, the contributions and scientific impact of this study have been examined in order to draw a roadmap with directions for future research.

7.2 Summary

The commercially used AZ and AS series Mg alloys, having reasonably high aluminium content, are most significant and economically competitive. However, they are unsuitable for power train applications in automobile industry owing to its poor mechanical properties at elevated temperature due to the presence of thermally unstable $Mg_{17}Al_{12}$ phase. RE addition is the best choice for attaining the aforementioned properties by the formation of RE-containing intermetallic phase results in improvement in high temperature tensile properties of Mg-Al alloys. Gadolinium (Gd) can reduce the formation of β- $Mg_{17}Al_{12}$ phase by consuming aluminium to form thermally stable intermetallic Al_2Gd phase, and also has an electrochemical potential almost near to that Mg. Introduction of hard intermetallic Al_2Gd phase can greatly enhance the wear resistance at room as well as high temperatures. Hence, studies on increasing the application of Mg-Al magnesium alloy for powertrain application with supportive wear and corrosion resistance with individual and combined effect of Gd with Ca is highly essential.

The icosahedral quasicrystal phase (I-phase) in Mg-Zn-RE alloys show a good combination of strength and ductility due to the strong interface between the I-phase and the Mg-matrix, which is due to the high symmetry and the quasiperiodicity of the I-phase. I-phase is very helpful for the mechanical properties of Mg alloys. Due to high hardness and low friction coefficient of I-phase, Mg alloys reinforced with I-phase particles usually have superior wear resistance. In order to fabricate the Mg alloy reinforced with I-phase, it is crucial to explore the formation range of I-phase in one alloy system. The relation between composition, microstructure and properties of Mg–Zn–Y based system in both as cast and heat treated conditions is well documented in the literature. However, the Mg–Gd–Zn system is relatively new, and has not been

investigated in detail. Mg–Zn–Gd is one of the very important systems as its microstructure consists of many different phases, such as I, W, X and laves phases, depending on the ratio of Zn to Gd contents, thus imparting different properties. Thus, the mechanical properties of these alloys can be tailored accordingly by altering the Zn and Gd contents.

Hence, to develop new Mg-Al-Gd and Mg-Zn-Gd alloys with high strength, wear and corrosion resistance, a thorough knowledge on the structure-property correlation of these alloys is essential. In the present investigation, alloys containing individual and combined effect of Gd with Ca are prepared, and their microstructure, mechanical corrosion and wear properties are evaluated in the as-cast condition. The conclusions drawn from each alloy system are summarized below.

7.2.1 Mg-Al Alloys

The structure-property evaluation of the Mg-Al alloys with addition of Gd and Ca are as follows:

- The microstructure of Mg-9Al consists of massive β-$Mg_{17}Al_{12}$ and α-Mg.
- When Gd is added in varying wt percentages to Mg-9Al alloy, in addition to the refinement of $Mg_{17}Al_{12}$ phase a thermally stable Al_2Gd phase is formed in the matrix.
- When Ca is added to Mg-9Al-2Gd alloys, the Ca atoms are incorporated into the β- $Mg_{17}Al_{12}$ phases and in addition to Al_2Gd phases, Al_2Ca phases are formed above 1 wt.% Ca addition.
- Better mechanical properties are obtained on Mg-9Al-2Gd-1Ca alloy due to suppression of discontinuous $Mg_{17}Al_{12}$ phase formation and the presence of Al_2Gd and Al_2Ca phases at the grain boundaries which effectively suppress the dislocation motion and grain boundary sliding.

- The corrosion resistance with Gd addition is mainly due to (1) improved film stability surrounding the β-$Mg_{17}Al_{12}$ phase due to the formation of Al_2Gd phase at the grain boundaries, (2) low volume fraction of β-$Mg_{17}Al_{12}$ phase, (3) presence of more protective oxide films and (4) reduction in grain size.
- Ca addition is observed to be detrimental to corrosion resistance.
- Formation of themally stable Al_2Gd phase in Mg-9Al alloys enhances the wear resistance of the alloys.

7.2.2 Mg-Zn Alloys

The variation of properties by the addition of Gd and Ca to Mg-Zn alloys are summarized below:

- The microstructure of Mg-5Zn alloys comprises of $MgZn_2$ and α-Mg.
- When the Zn/Gd ratio is in the range of 7-3, the main phases present in the alloys are $(Mg,Zn)_3Gd$ and Mg_3Zn_6Gd. In addition to the $(Mg,Zn)_3Gd$ phase, $Mg_{12}ZnGd$ phase is formed when the Zn/Gd ratio is decreased to 1.
- It is seen that the morphology of $(Mg,Zn)_3Gd$ phase becomes more continuous with decrease in Zn/Gd ratio.
- With increasing Ca content, the volume of $(Mg,Zn)_3Gd$ phase decreases and the $Ca_2Mg_6Zn_3$ phase increases.
- Mg-5Zn-3Gd alloy yields higher mechanical properties due to the presence of Mg_3Zn_6Gd, which effectively strengthens the material. However, the elongation is poor due to the brittle $(Mg,Zn)_3Gd$ phase at the boundaries.
- The increase in corrosion rate of the Mg-5Zn alloys with Gd above 3 wt.% can be attributed to the presence of continuous $(Mg, Zn)_3Gd$ phase and $Mg_{12}ZnGd$ phases at the boundaries. In Ca added alloys, in addition to the W phase, $Ca_2Mg_6Zn_3$ phase act as cathodic sites and accelerate the corrosion rate.

- The decrease in the wear rate upto 3 wt.% Gd addition to Mg-5Zn alloys is attributed to the hard Mg_3Zn_6Gd particles. With further increase of Gd content, brittleness increased with the increase in volume fraction of $(Mg,Zn)_3Gd$ phase.

Scope of Future Work

- A detailed TEM study to identify the mechanism responsible for improving the properties of Gd added Mg-Al and Mg-Zn alloys.
- A study on the effect of heat treatment on Mg-Al and Mg-Zn alloys.
- Creep studies for Mg-Al-Gd, Mg-Al-Gd-Ca, Mg-Zn-Gd, Mg-Zn-Gd-Ca alloys and study the creep mechanisms responsible for improving the high temperature properties.
- The corrosion behavior of magnesium alloys in coolants is still unclear and has not been systematically investigated. The compatibility of magnesium alloy in coolants that are developed for non magnesium alloys is yet another concern. The conventional coolant consists of 30–70 vol% ethylene glycol (EG) and and some inhibitors like molybdate, phosphate, borate, nitrate, nitrite, tolyltriazole, benzoate and silicate. The corrosion behavior of the developed magnesium alloys in ethylene glycol need to be investigated at ambient temperature.

References

[1] M.O. Pekguleryuz, M. Dierks, Proceedings of Annual World MA 2001 Magnesium Conference, **2001**, 32, 37.

[2] G. Pettersen, H. Westengen, R. Hoier, O. Lohne, *Mater Sci Eng A*, **1996**, 207, 115.

[3] M.O. Pekguleryuz, J. Renaud, in Magnesium Technology 2000 (eds H. I. Kaplan, J. N. Hryn and B. B. Clow), John Wiley & Sons, Inc., Hoboken, NJ, USA. **2000**, 279.

[4] A. Luo, M.O. Pekguleryuz, *J Mater Sci*, **1994**, 29, 5259.

[5] A.A. Luo, Recent magnesium alloy development for elevated temperature applications, *Int Mater Rev*, **2004**, 49, 13.

[6] Y.L. Song, Y.H. Liu, S.H. Wang, S.R. Yu, X.Y. Zhu, *Mater Corros*, **2007**, 58, 189.

[7] X. Wang, W. Du, K. Liu, Z. Wang, S. Li, *J Alloy Compd*, **2012**, 522, 78.

[8] F. Lu, A. Ma , J. Jiang, Y.Guo, D. Yang, D. Song, J. Chen, *Corros Sci,* **2015,** 94 171.

[9] Z. Li, X. Gu, S. Lou, Y. Zheng, *Biomaterials*, **2008**, 29, 1329.

[10] N. Li, Y. Zheng, *J. Mater Sci Technol*, **2013**, 29, 489.

[11] Y. Shi, M. Qi, Y. Chen, P. Shi, *Mater Let*, **2011**, 65, 2201.

[12] S.Cai, T. Lei, N. Li, F. Feng, *Mater. Sci. Eng. C*, **2012**, 2570.

[13] G.Q. Li, G.H. Wu, Y. Fan, W.J. Ding, *Foundry Technol*, **2006**, 27, 81.

[14] E. Abe, Y. Kawamura, K. Hayashi, A. Inoue, *Acta Mater*, **2002**, 50, 3845.

[15] Y.M. Zhu, A.J. Morton, J.F. Nie, *Acta Mater*, **2010**, 58, 2936.

[16] Z. Yang, J.P. Li, J.X. Zhang, G.W. Lorimer, J. Robson, *Acta Metall*, **2008**, 21,

313.

[17] B.L. Mordike, T. Ebert, *Mater Sci Eng A*, **2001**, 302, 37.

[18] M. Gupta, W.L.E. Wong, *Mater Charact*, **2015**, 105, 30.

[19] C.C. Jain, C.H. Koo, *Mater Trans*, **2007**, 2, 265.

[20] S.R. Agnew, J.F. Nie, *Scr Mater*, **2010**, 63, 671.

[21] I.J. Polmear, Magnesium alloys, in: I.J. Polmear (Ed.) Light Alloys, Butterworth-Heinemann, Oxford, **2005**, 237.

[22] P.K. Mallick, Overview, in: P.K. Mallick (Ed.) Materials, Design and Manufacturing for Lightweight Vehicles, Woodhead Publishing, **2010**, 1.

[23] C.S. Roberts, *Magnesium and its alloys*, ed. J.H. Hollomon 1960, New York, USA: John Wiley & Sons. p. 5.

[24] M.K. Kulekci, *Int J Adv Manuf Technol*, **2008**, 39, 851.

[25] D. Duly, M.C. Cheynet, Y. Brechet, *Acta Metall Mater*, **1994**, 42, 3843-3854.

[26] N. Hort, Y. Huong, K.U. Kainer, *AEM*, **2006,** 8, 235.

[27] Z. Yu, H. Zhao, X. Hu, D. Ju, *Trans Nonferrous Met Soc China*, **2010**, 20, 318.

[28] M. Gupta, N.M.L. Sharon, Magnesium, Magnesium Alloys, and Magnesium *Composites*, A John Wiley & Sons, Inc. Publication, United States of America (**2011**).

[29] A. Boby, A. Srinivasan, U.T.S. Pillai, B.C. Pai, Mater Des, 2015, 88, 871.

[30] H.T. Son, J.S. Lee, I.H. Oh, D.G. Kim, K. Yoshimi, K. Maruyama, *Mater Trans*, **2008**, 49, 1025.

[31] C.D. Yim, B.S. You, R.S. Jang, S.G. Lim, *J Mater Sci*, **2006**, 41, 2347.

[32] S.F. Hassan, M. Gupta, *Mater Res Bull*, **2002**, 37, 377.

[33] W.L.E.Wong, M. Gupta, *Compos Sci Technol*, **2007**, 67, 1541.

[34] A.A. Luo, Fundamentals of Magnesium Alloy Metallurgy, Woodhead Publishing, **2013**, 266.

[35] A.A. Luo, A.K. Sachdev, Advances in Wrought Magnesium Alloys, Woodhead Publishing, **2012**, 393.

[36] F. Czerwinski, *Corros Sci*, **2014**, 86, 1.

[37] L. Choudhary, R.K.S Raman, Surface Modification of Magnesium and its Alloys for Biomedical Applications, Woodhead Publishing, Oxford, **2015**, 179.

[38] Y. Chen, Z. Xu, C. Smith, J. Sankar, *Acta Biomaterialia*, **2014**, 10, 4561.

[39] Z.H. Chen, J.H. Chen, *Frontiers of Materials Science in China*, **2008**, 2, 1.

[40] H.E. Friedrich, B.L. Mordike, Magnesium Technology: Metallurgy, Design Data, *Applications*, Springer, Berlin, New York (**2006**).

[41] H.Okamoto, *J Phase Equilib*, **1992**, 13, 105.

[42] M.O. Pekguleryuz, A.A. Kaya, AEM, **2003**, 5, 866.

[43] S.F. Hassan, M. Gupta, *J Alloy Compd*, **2002**, 345, 246.

[44] A.K. Dahle, Y.C. Lee, M.D. Nave, P.L. Schafer, D.H. St John, *J Light Met*, **2001**, 1, 61.

[45] R.L. Fleisgher, *Acta Metall*, **1961**, 9, 996.

[46] R. Labusch, *Physica Status Solidi* (B), **1970**. 41, 659.

[47] F. Czerwinski, *Magnesium alloys - design, processing and properties.* InTech, **2011**.

[48] J.F. Nie, *Metall Mater Trans*, **2012**. 43, 3891.

[49] K.U. Kainer, P. Bala Srinivasan, C. Blawert, W. Dietzel, 3.09 - Corrosion of Magnesium and its Alloys, in: B.C.G.L.L.R.S. Stott (Ed.) Shreir's Corrosion, Elsevier, Oxford, **2010**, 2011.

[50] L. Xiaoyan, L. Mingzhao, F. Liuqun, W. Haiyan, F. Chong, M. Hua, *Rare Metal Materials and Engineering*, **2014**, 43, 278.

[51] P. Casajus, N. Winzer, *Mater Sci Eng A*, **2014**, 602, 58.

[52] R. Arrabal, E. Matykina, F. Viejo, P. Skeldon, G.E. Thompson, *Corros Sci*, **2008**, 50, 1744.

[53] E. Ghali, Activity and passivity of magnesium (Mg) and its alloys, in: G. Song (Ed.) Corrosion of Magnesium Alloys, Woodhead Publishing, **2011**, 66.

[54] A. Boby, K.K. Ravikumar, U.T.S. Pillai , B.C. Pai, Procedia Eng., 2013, 55, 98.

[55] J. Zhang, X. Niu, X. Qiu, K. Liu, C. Nan, D. Tang, J. Meng, *J Alloys Compd*, **2009**, 471, 322.

[56] S. Gollapudi, *Corros Sci*, 62 (**2012**) 90.

[57] A. Zafari, H.M. Ghasemi, R. Mahmudi, *Wear*, **2012**, 292-293, 33.

[58] H. Chen, A.T. Alpas, *Wear*, **2000**, 246, 106.

[59] N.N. Aung, W. Zhou, L.E.N. Lim, *Wear*, **2008**, 265, 780.

[60] M. Sharifzadeh, M.A. Ansari, M. Narvan, R.A. Behnagh, A. Araee, M.K.B Givi, Trans Nonferrous Met Soc China, **2015**, 25, 1847.

[61] M. Hu, Q. Wang, C. Chen, D. Yin, W. Ding, Z. Ji, *Mater Des*, **2012,** 42, 223.

[62] Y. Song, K. Dong, D. Shan, E.H. Han, *Appl Surf Sci*, **2014,** 314, 888.

[63] P.B. Srinivasan, C. Blawert, W. Dietzel, *Mater Charact*, **2009**, 60, 843.

[64] H. Somekawa, S. Maeda, T. Hirayama, T. Matsuoka, T. Inoue, T. Mukai, *Mate Sci Eng A*, **2013**, 561, 371.

[65] S.R. Wang, P. Quan, G. Li, Y. Yang, Y. Wang, *J Mater Eng Perform*, **2009**, 18, 137.

[66] R. Muraliraja H.Vettrivel, R. Elansezhian, *IJEIT*, **2013**, 2, 388.

[67] P. Lin, H. Zhou, W. Li, M. Wang, Q. Guo, H. Tang, W. Li, *J Alloy Compd*, **2009**, 481, 373.

[68] W. Liu, F.Cao , L. Chang, Z. Zhang, J. Zhang, *Corros Sci*, **2009**, 51, 1334.

[69] S. Lee, S. H. Lee, D.H. Kim, *Metall Mater Trans A*, **1998**, 29A, 1221.

[70] Q.Yang, F. Bu, F. Meng, X. Qiu, D. Zhang, Ti. Zheng, X. Liu, J. Meng, *Mater Sci Eng A*, **2015**, 628, 319.

[71] N. Kashefi, R. Mahmudi. *Mater Design*, **2012**, 39, 200.

[72] M. Nouri, X. Sun, D.Y. Li, *Tribol Int*, **2013**, 67, 154.

[73] T.J. Luo, Y.S. Yang, *Mater Des*, **2011**, 32, 5043.

[74] Y. Kawamura, K. Hayashi, A. Inoue, T. Masumoto, *Mater Trans*, **2001**, 42, 1172.

[75] F. Mert. A. Ozdemir, K.U. Kainer, N. Hort, *Trans Nonferrous Met Soc China*, **2013**, 2366.

[76] S. Tekumalla, S. Seetharaman, A. Almajid, M. Gupta, *Metals*, **2015**, 5, 1.

[77] A.K. Chaubey, S. Scudino, K.G. Prashanth, J. Eckert. *Mater Sci Eng A*, **2015**, 625, 46.

[78] F. Guo, P. Li. X. Gao, J. Xu, *Journal of Rare Earths*, **2010**, 28, 948.

[79] X.B. Liu, D.Y. Shan, Y.W. Song, E.H. Han, Trans Nonferrous Met Soc China, **2010**, 20, 1345.

[80] J. Bai Y. Sun, F. Xue, J. Qiang, *Mater Sci Eng A*, **2012**, 552, 472.

[81] A. Zafari H. M. Ghasemi. R.Mahmudi, *Mater Des*, **2014**, 54, 544-552.

[82] A. Moosa, *KECBUJ*, **2011**, 7, 75.

[83] J. Zhang, P.Yu, K. Liu. J. Meng, *Mater Design*, **2009**, 30, 2372.

[84] R. Mahmudi F. Kabirian, Z. Nematollahi, *Mater Des*, **2011**, 32, 2583.

[85] D.K. Xu, W.N. Tang, L. Liu, Y.B. Xu, E.H. Han, *J Alloy Compd*, **2008**, 461, 248.

[86] J.Wang, L. Wang, J. An, Y. Liu J, *Mater Eng Perform*, **2008**, 17, 725.

[87] R. Arrabal, B. Mingo, A. Pardo, A. Maroto, *Corros Sci*, **2015**, 97, 38.

[88] X. Wang, W. Du, K. Liu, Z. Wang, Shubo Li, *J Alloy Compd*, **2012**, 522, 78.

[89] M. Yang, Y. Liu, J. Liu, Y. Song, *J Rare Earth*, **2014**, 32, 558.

[90] H. Yokobayashi, K. Kishida, H. Inui, M. Yamasaki, Y. Kawamura, *Acta Mater*, **2011**, 59, 7287.

[91] L. Zhang, K. Deng, K. Nie, F. Xu, K. Su, W. Liang, *Mater Sci Eng A*, **2015**, 636, 279.

[92] Z. Jiang, B. Jiang, H. Yang, Q. Yang, J. Dai, F. Pan *J Alloy Compd*, **2015**, 647, 357.

[93] D. Xiao, Z. Chen, X. Wang, M. Zhang, D. Chen, *Mater Sci Eng A*, **2016**, 660, 166.

[94] H. Du, Z. Wei, X. Liu, E. Zhang, *Mater Chem Phys*, **2011**, 125, 568.

[95] X.N. Gu, Y.F. Zheng, Y. Cheng, S.P. Zhong, T.F. Xi, *Biomaterials*, **2009**, 30, 484.

[96] S.X. Zhang, X.N. Zhang, C.L. Zhao, J.N. Li, Y. Song, C.Y. Xie, *Acta Biomater*, **2010**, 6, 626.

[97] S.X. Zhang, J.N. Li, Y. Song, C.L. Zhao, X.N. Zhang, C.Y. Xie, *Mater Sci.Eng C*, **2009**, 29, 1907.

[98] C.J. Boehlert, K. Knittel, *Mater Sci Eng A*, **2006**, 417, 315.

[99] T.B. Massalski, Binary Alloy Phase Diagrams, American Society for Metals, Ohio, **1986**, 982.

[100] X.B. Liu, D.Y. Shan, Y.W. Song, E.H. Han, *Trans Nonferrous Met Soc China* 2010, **20**, 1345.

[101] O. Boudouard, *Proceedings of the National Academy of Sciences*, **1904**, 139, 424.

[102] G. Grube, *J Phys Chem*, **1906**, 10, 587.

[103] R.J. Chadwick, *Journal of the Institute of Metals*, **1928**, 449, 285.

[104] S. Samson, *Acta Chemica Scandinavica*, **1949**, 3, 835.

[105] J.J. Park, L.L.Wyman, WADC Technical Report: Astia Document AD142110, **1957**, 57.

[106] E.D.R.W. Hume Rothery, *Journal of the Institute of Metals*, **1929**, 41, 119.

[107] F. Laves, *Die Naturwissenschaften*, **1939**, 454.

[108] J. Clark, F. Rhins, *J Metals*, **1957**, 9, 425.

[109] I. Higashi, N. Shiotani, M. Uda, T. Mizoguchi, H. Katoh, *J Solid State Chem*, **1981**, 36, 225.

[110] J.B. Clark, L. Zabdyr, Z. Moser, ASM International, Metals Park, Ohio, USA, **1988**, 353.

[111] P. Liang, T. Tarfa, J. A. Robinson, S Wagner, P. Ochin, M.G Harmelin, H.J Seifert, H.L Lukas, F Aldinger, *Thermochimica Acta*, **1998**, 314, 87.

[112] A.A. Nayeb-Hashemi, J.B. Clark: ASM International, Materials Park, OH, **1988**, 157.

[113] X. Gao, J.F, Nie, *Scripta Mater*, **2007**, 57, 655.

[114] J.B. Clark: *Acta Metall*, **1965**, 13, 1281.

[115] G. Mima, Y. Tanaka, *Trans Jpn Inst Met*, **1971**, 12, 71.

[116] G. Mima, Y. Tanaka, *Trans Jpn Inst Met*, **1971**, 12, 76.

[117] L.Y. Wei, G.L. Dunlop, H. Westengen, *Metall Mater Trans A*, **1995**, 26, 1705.

[118] P.V. Padfield, ASM Handbook, ASM International Materials Park, OH, **2004**, 9, 801.

[119] L. Gao, R.S. Chen, E.H. Han, *J Alloy Compd*, **2009**, 481, 379.

[120] K. Kishida, K. Nagai, A. Matsumoto, A. Yasuhara, H. Inui, *Acta Mater*, **2015**. 99, 228.

[121] J.Y. Lee, D.H. Kim, H.K. Lim, D.H. Kim, *Mater Lett*, **2005**, 59, 3801.

[122] Y. Kawamura, M. Yamasaki, *Mater Trans*, **2007**, 48, 2986.

[123] J.H. Li, P. Schumacher, IOP Conference Series: Mater Sci Eng, 2013, 341.

[124] J. Li, Z. He, P. Fu, Y. Wu, L. Peng, W. Ding, *Mater Sci Eng A*, 2016, 651, 745.

[125] J. Grobner, A. Kozlov, X.Y. Fang, S. Zhu, J.F. Nie, M.A. Gibson, R.S. Fetzer, *Acta Mater*, 2015, 90, 400.

[126] A. Srinivasan, C. Blawer, Y. Huang, C.L. Mendis , K.U. Kainer, N. Hort; *J Magnesium Alloys*, 2014, 2, 245.

[127] A. Srinivasan, Y. Huang, C.L. Mendis, C. Blawert, K.U. Kainer, N. Hort, *Mater Sci Eng A*, 2014, 595, 224.

[128] M. Yang, T. Guo, H. Li, *Mater Sci Eng A*, 2013, 587, 132.

[129] L.B. Tong, Q.X. Zhang, Z.H. Jiang, J.B. Zhang, J. Meng, L.R. Cheng, H.J. Zhang, *J Mech Behav Biomed Mater*, 2016, 62, 57.

[130] Y.Z. Du, X.G. Qiao, M.Y. Zheng, K. Wu, S.W. Xu, *Mater Des*, 2015, 85, 549.

[131] Z. Qingxin, T. Libo, C. Liren, J. Zhonghao, M. Jian, Z. Hongjie, *J Rare Earths*, 2015, 33, 70.

[132] A. Singh, A.P. Tsai, M. Nakamura, M. Watanbe, A. Kato, Philos, *Mag Lett*, **2006**, 83, 543.

[133] D.K. Xu, E.H. Han, L. Liu, Y.B. Xu, *Metall Mater Trans A*, **2009**, 40, 1727.

[134] Z.H. Huang, S.M. Liang, R.S. Chen, E.H. Han, *J Alloys Compd*, **2009**, 468, 170.

[135] E. Zhang, W. He, H. Du, K. Yang, *Mater Sci Eng A*, 2008, 488, 102.

[136] Y. Liu, G. Yuan, S. Zhang, X. Zhang, C.Lu, W. Ding, *Mater Trans*, **2008**, 49, 941.

[137] Y.J. Wu, X.Q. Zeng, D.L. Lin, L.M. Peng, W.J. Ding, *J Alloys Compd*, **2009**, 477, 193.

[138] S. Zhang, G.Y. Yuan, C. Lu, W.J. Ding, *J Alloys Compd*, **2011**, 509, 3515.

[139] L.Y. Wei, G.L. Dunlop, *J Alloys Compd*, **1996**, 232, 264.

[140] T. Rzychon, A. Kiełbus, *JAMME*, **2006**, 17, 149.

[141] H.L. Chen, L. Lin, P.L. Mao, Z. Liu, *Journal of Magnesium and Alloys*, **2015**, 3, 197.

[142] S.M. Zhu, M.A. Gibson, J.F. Nie, M.A. Eastona, T.B. Abbott, *Scripta Mater*, **2008**, 58, 477.

[143] S.M. Jo, K.C. Park, B.H. Kim, H. Kimura, S.K. Park, Y.H. Park, *Mater Trans*, **2011**, 52, 1088.

[144] B. Kondori, R. Mahmudi, *Mater Sci Eng A*, **2010**, 527, 2014.

[145] L. Han, H. Hu, D.O. Northwood, *Mater Lett*, **2008**, 62, 381.

[146] C. Yuan, J. Li, F. Dan, S.Yu, Y. Ruiyu, *J Rare Earth*, **2015**, 33, 86.

[147] J. Liu, W. Wang, S. Zhang, D. Zhang, H. Zhang, *J Alloys Compd*, **2015,** 620, 74.

[148] Y. Qiang, G. Kai, B. Fanqiang, Z. Yaqin, Q. Xin, Z. Tian, L. Xiaojuan, M. Jian, *Mater Charact*, **2016**, doi: 10.1016/j.matchar.2016.01.024.

[149] Y.Z. Lu, Q.D. Wang, X.Q. Zeng, W. J. Ding, C.Q. Zhai, Y.P. Zhu, *Mater Sci Eng A*, **2000**, 278, 66.

[150] Z.T. Jiang, B. Jiang, J.Y. Zhang, X.S. Xia, F.S. Pan, *Mater Sci Forum*, **2015**, 816, 486.

[151] B. Jiang, W. Liu, D. Qiu, M.X. Zhang, F. Pan, *Mater Chem Phys*, **2012**, 133, 611.

[152] S. Liu, B. Li, X. Wang, W. Su, H. Han, *J Mater Process Technol*, **2009**, 209, 3999.

[153] D.H. Bae, Y. Kim, I.J. Kim, *Mater Lett*, **2006**, 60, 2190.

[154] D.K. Xu, L. Liu, Y.B. Xu, E.H. Han, *Acta Mater*, **2008**, 56, 985.

[155] A. Singh, M. Nakamura, M. Watanabe, A. Kato, A.P. Tsai, *Scr Mater*, **2003**, 49, 417.

[156] R. Banerjee, R.T. Savalia, D. Prakash, U.D. Kulkami, G.K. Dey, *Scr Mater*, **1995**, 32, 1607.

[157] S.S. Park, Y.S. Oh, D.H. Kang, N.J. Kim, *Mater Sci Eng A*, **2007**, 449, 352.

[158] J.Y. Lee, H.K. Lim, D.H. Kim, *Mater Lett,* **2005**, 59, 3801.

[159] A. Singh, H. Somekawa and T. Mukai, *Scripta Mater*, **2007**, 56, 935.

[160] J Yang, L Wang, H Zhang, *J Alloys Compd*, 2008, 459, 274.

[161] J.M. Kim, J.S. Park, Int J Cast Metals Res, 2011, 24, 127.

[162] J.Yang, W.L. Xiao, L.D. Wang, Y.M. Wu, L.M. Wang, H.J. Zhang, *Mater Charact*, **2008**, 59, 1667.

[163] D.H. Bae, S.H. Kim, W.T. Kim, *Acta Mater*, **2002**, 50, 2343.

[164] G. Levi, S. Avraham, A. Zilberov, M. Bamberger, *Acta Mater*, **2006**, 54, 523.

[165] M.B. Yang, L. Cheng, F.S. Pan, *J Mater Sci*, **2009**, 44, 4577.

[166] M.B. Yang, L. Cheng, F.S. Pan, *Int J Cast Met Res*, **2010**, 23, 111.

[167] N. Yang, T. Guo, C. Qin, F. Pan, *J Rare Earths*, **2012**, 30, 181.

[168] E.L. Zhang, L. Yang, *Mater Sci Eng A*, **2008**, 497,111.

[169] N. Balasubramani, U.T.S. Pillai, B.C. Pai, *J Alloys Compds*, **2008**, 460, L6.

[170] N. Balasubramani, U.T.S. Pillai, B.C. Pai, *J Alloys Compds*, **2008**, 457,118.

[171] T. Rzychon, A. Kiełbus, L. Litynska-Dobrzynska, *Mater Charact*, **2013**, 83, 21.

[172] Q. Peng, H. Dong, Y. Wu, L. Wang, *J Alloys Compd*, **2008**, 456, 395.

[173] J. Wang, L. Wang, J. An, Y. Liu, *JMEPEG*, **2008**, 17, 725.

[174] W. Zhou, Q. Li, H.J. Kang, Q. Zhang, *AMM*, **2012**, 117, 1125,

[175] Q. Guo, Z. Liu, P. Mao, J. Sun, *Mater Sci Forum*, **2013**, 747, 301.

[176] Y. Miao, L. Yaohui, L. Jiaan, S. Yulai, *J Rare Earths*, **2014**, 32, 558 .

[177] L. Yonggan, W. Yinghui, H. Lifeng, G. Chunli, H. Pengju, *J Rare Earth*, **2014**, 32, 1064

[178] L. Zhang, Z.Y. Cao, Y.B. Liu, G.H. Su, L.R. Cheng, *Mater Sci Eng A*, **2009**, 508, 129.

[179] Y. Lu, Q. Wang, X. Zeng, W. Ding, C. Zhai, Y. Zhu, *Mater Sci Eng A*, **2000**, 278, 66.

[180] H. Chena, K. Zhanga, C. Yaoa, J. Dong, Z. Li, C. Emmelmann, *Appl Surf Sci*, **2015**, 330, 393.

[181] G. Wu, Y. Fan, H. Gao, C. Zhai, Y.P. Zhu, *Mater Sci Eng A*, **2005**, 408, 255.

[182] D.K. Xu, W.N. Tang, L. Liu, Y.B. Xu, E.H. Han, *J Alloys Compd*, **2007**, 432, 129.

[183] J. Wang, P. Song, S. Gao, Y. Wei, F. Pan, *J Mater Sci*, **2012**, 47, 2005

[184] D.K. Xu, L. Liu, Y.B. Xu, E.H. Han, *Mater Sci Eng A*, 2007, 443, 248.

[185] Y. Liu, G. Yuan, W. Ding, C. Lu, *J Alloys Compd*, **2007**, 427, 160.

[186] G. Song, *Adv Eng Mater*, **2005**, 7, 563.

[187] Q.X. Zhang, L.B. Tong, L.R. Cheng, Z.H. Jiang, J. Meng, H.J. Zhang, *J Rare Earth*, **2015**, 33, 70.

[188] Y. Du, M. Zheng, X. Qiao, D. Wang, W. Peng, K. Wu, B. Jiang, *Mater Sci Eng A*, **2016**, 656, 67.

[189] Y.Z. Du, X.G. Qiao, M.Y. Zheng, D.B. Wang, K.Wu, I.S. Golovin, *Mater Des*, **2016**, 98, 285

[190] F. Naghdi, R.Mahmudi, *Mater Sci Eng A*, **2014**, 610, 315.

[191] N.J. Petch, *J Iron Steel Inst*, **1953**, 174, 25.

[192] G. L. Song, A. L. Bowles, D. H. St John, *Mater Sci Eng A*, **2004**, 366, 74.

[193] Y. Jiao, J. Zhang, L. He, M.Zhang, F. Jiang, W. Wang, Li. Han, L. Xu, R.Wu, *Adv Eng Mater*, **2016**, 18, 148 .

[194] P. Xiaodong, L. Junchen, L. Wenjuan, Y. Yan, W. Qunyi, *Rare Metal* Mat Eng, **2013**, 42, 1993.

[195] A. Srinivasan, S. Ningshen, U. Kamachi Mudali, U.T.S. Pillai, B.C. Pai, *Intermetallics*, **2007**, 15, 1511.

[196] D. Huang, J. Hu, G. L. Song, X. Guo, *Electrochim Acta*, **2011**, 56, 10166 .

[197] F. Rosalbino, E. Angelini, S. De Negri, A. Saccone, S. Delfino, *Intermetallics*, **2006**, 14, 1487.

[198] R. Arrabal, E. Matykina, A. Pardo, M.C. Merino, K. Paucar, M. Mohedano, P. Casajus, *Corros Sci*, **2012**, 55, 351.

[199] G.L. Song, A. Atrens, D. St John, J. Nairn, Y. Li, *Corros Sci*, **1997**, 39, 855.

[200] G.L. Song, A. Atrens, D. St John, X. Wu, J. Nairn, *Corros Sci*, **1997**, 39, 1981.

[201] D. Sachdeva, *Corros Sci*, **2012**, 60, 18.

[202] M. Mandal, A.P. Moon, G. Deo, C.L. Mendis, K. Mondal, *Corros Sci*, **2014**, 78, 172.

[203] H.R. Bakhsheshi Rad, M.R. Abdul Kadir, M.H. Idris, S. Farahany, *Corros Sci*, **2012**, 64, 184.

[204] Q. Liu, W. Cheng, H. Zhang, C. Xu, J. Zhang, *J Alloys Comp*, **2014**, 590, 162.

[205] J. Wang, Y. Li, S. Huang, X. Zhou, *App Surf Sci*, **2014**, 317,1143.

[206] R.C. Zeng, W.C. Qi, H. Z. Cui, F. Zhang, S.Q. Li, E.H. Han, *Corros Sci*, **2015**, 96, 23.

[207] E. Dabah, G. Ben Hamu, V. Lisitsyn, D. Eliezer, K.S. Shin, *J Mater Sci*, **2010**, 45, 3007.

[208] R.K. Singh Raman, *Metall Mater Trans A,* **2004**, 35, 2525.

[209] F. Zucchi, V. Grassi, A. Frignani, C. Monticelli, G. Trabanelli, *J Appl Electrochem*, **2006**, 36, 195.

[210] N. Birbilis, M.A. Easton, A.D. Sudholz, S.M. Zhu, M.A. Gibson, *Corros Sci,* **2009**, 51, 683.

[211] A.D. Sudholz, K Gusieva, X.B. Chen, B.C. Muddle, M.A. Gibson, N. Birbilis, Corros Sci, **2011**, 53, 2277.

[212] L. Bresson, D. Gratias, *J Non-Cryst Solids*, **1993**, 153, 468.

[213] D. Zander, N.A. Zumdick, *Corros Sci*, **2015**, 93, 222.

[214] Z. Shi, M. Liu, A. Atrens, *Corros Sci*, **2010**, 52, 579.

[215] L. Yang, Y. Huang, F. Feyerabend, R. Willumeit, , C. Mendis, K.U. Kainer, N. Hort, *Acta Biomater*, **2013**, 9, 8499.

[216] W.C. Kim, J.G. Kim, J.Y. Lee, H.K. Seok, *Mater Lett*, **2008**, 62, 4146.

[217] D.Z. Naemi, A. Zumdick, *Corros Sci*, **2015**, 93, 222.

[218] H.R. Bakhsheshi-Rad, M. Abdellahi, E. Hamzah, A.F. Ismail, M. Bahmanpour, *J Alloy Compd*, **2016**, 687, 630.

[219] C. Taltavull, B. Torres, A.J. Lopez, J. Rams, *Wear,* **2013**, 301, 615.

[220] R. Wittmann, K. Urban, M. Schandl, E. Hornbogen, *JMR*, **1991**, 6, 1165.

[221] Y.B. Zhang, S.R. Yu, Y.R. Luo, H.X. Hu, *Mater Sci Eng A,* **2008**, 472, 59.

Publications

- **K.R. Athul**, A. Srinivasan, U.T.S. Pillai and B.C. Pai; ***"A Comparative Study on Corrosion Behavior of Mg-Zn-Gd alloys by Varying the Gd Content";*** Materials Science Forum; Vols. 830-831 (2015) pp 631-634.

- **K.R. Athul**, A. Srinivasan, U.T.S. Pillai and B.C. Pai; ***"A Review of different Creep Mechanisms in Mg Alloys Based on Stress Exponent and Activation Energy";*** Advanced Engineering Materials; Vol 18 (2016) pp 770–794.

- P. Ajmal, **K.R. Athul**, A. Srinivasan, U.T.S. Pillai and B.C. Pai; ***"Effect of Rare Earth Elements on the Mechanical Properties of Mg-Al Alloys";*** Indian Foundry Journal; Vol 62 (2016) pp 33-47.

- **K.R. Athul**, A. Srinivasan, and U.T.S. Pillai; ***"Investigations on the Microstructure, Mechanical, Corrosion and Wear Properties of Mg-9Al-xGd (0, 0.5, 1 and 2 wt%) Alloys";*** Journal of Materials Research Vol 32 (2017) pp 3732-3743.

Conference Proceedings / Publications

- **K.R. Athul**, A. Srinivasan, U.T.S. Pillai and B.C. Pai; ***"A Comparative Study on Corrosion Behavior of Mg-Zn-Gd alloys by Varying the Gd Content";*** poster presented at ICAMPS held at Thiruvananthapuram, Kerala between 13th and 15th May 2015.

- **K.R. Athul**, A. Srinivasan, U.T.S. Pillai and B.C. Pai; ***"Effect of Varying the Gd Content (0,3,5, 10 and 12 wt%) on the Mechanical and Corrosion Behavior of***

Mg-5Zn Alloys"; oral presention at NMD- ATM held at Coimbatore, Tamil Nadu between 13th and 16th November 2015.

- **K.R. Athul**, A. Srinivasan and U.T.S. Pillai; ***"Effect of Varying the Gd Content (0, 0.5, 1 and 2 wt%) on the Microstructure, Mechanical and Corrosion Behavior of Mg-9Al Alloys";*** oral presention at NCRAME held at Tirunelveli, Tamil Nadu on 6th April 2016.

- M. Rahul**, K.R. Athul**, R. Ajith, A. Srinivasan and U.T.S. Pillai; ***"Investigation on the Creep Behavior of Mg-Al-Re Alloys"*** Oral presentation at National Conference on Technological Trends held at Thiruvananthapuram, Kerala between 6th and 7th June 2016.